Air Force Institute of Technology

AFIT Scholar

3-1997

Quantification of Weather Effects on Imaging Laser Radar

Clifton D. Stargardt

QUANTIFICATION OF WEATHER EFFECTS
ON IMAGING LASER RADAR

THESIS

Clifton D. Stargardt
Captain, United States Air Force

AFIT/GM/ENP/97M-09

DEPARTMENT OF THE AIR FORCE
AIR UNIVERSITY

AIR FORCE INSTITUTE OF TECHNOLOGY

Wright-Patterson Air Force Base, Ohio

QUANTIFICATION OF WEATHER EFFECTS
ON IMAGING LASER RADAR

THESIS

Clifton D. Stargardt
Captain, United States Air Force

AFIT/GM/ENP/97M-09

19970402 074

Approved for public release; distribution unlimited

AFIT/GM/ENP/97M-09

QUANTIFICATION OF WEATHER EFFECTS

ON IMAGING LASER RADAR

THESIS

Presented to the Faculty of the School of Engineering

Air Education and Training Command

In Partial Fulfillment of the

Requirements for the Degree of

Master of Science (Meteorology)

Clifton D. Stargardt, B.A., B.S.

Captain, United States Air Force

March 1997

QUANTIFICATION OF WEATHER EFFECTS ON
IMAGING LASER RADAR

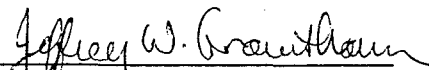Clifton D. Stargardt, B.A., B.S.
Captain, USAF

Approved:

Maj Clifton E. Dungey
Chairman, Advisory Committee

10 MAR 97
Date

Maj Jason P. Tuell
Member, Advisory Committee

10 Mar 97
Date

Maj Jeffrey W. Grantham
Member, Advisory Committee

10 Mar '97
Date

Acknowledgments

When the time arrived to choose thesis topics, I knew I wanted to get involved in a subject that was interesting, exciting, certain to benefit the Air Force, and on the leading edge of technology. I certainly found what I was looking for. This topic has been a wonderful challenge and the entire thesis process has been a rewarding experience. I am thankful to the Meteorology Department for allowing me to tackle this subject.

I am most grateful to my advisor, Major Clifton Dungey, for his support and guidance in this effort. He gave me the reigns of this project from the beginning, adding insight and perspective when I asked or when he thought I might be straying from the correct path. His style has allowed me to make mistakes, correct them when I could, and seek help when I couldn't. Major Dungey has played an invaluable role in the completion of this thesis. I thank my thesis committee, Major Jason Tuell, and Major Jeff Grantham, who is also my sponsor. They courageously volunteered to review draft versions of this thesis and have provided significant suggestions and comments. I owe a debt of gratitude to Lieutenant Eddie Meidunas. His previous work on this project, programming of *Labview* files, retrieving any and all information I required, and countless other consequential tasks have been immeasurable help. Eddie's efforts in this project have been key to its success.

I thank the members and faculty of GM-97M, the first AFIT in-residence meteorology class. They have made this program challenging, rewarding, and fun. When things became hectic, I always knew I had eight great guys with me, and four of the finest

professors I've known to help me out. Their comradeship has made this a wonderful experience.

Finally, I wish to thank my Mom and Dad for their support and encouragement. I am incredibly lucky and proud to have such wonderful parents, and a lifetime of "thank you" and "I love you" will never be enough to repay all they have given me.

Captain Clifton Dean Stargardt

Table of Contents

List of Figures

List of Tables

Abstract

The Air Force is investigating the use of imaging laser radar systems as autonomous guidance systems on future precision guided munitions. The Air Force's Wright Laboratory is currently testing a 1.06 μm wavelength laser radar (ladar) at Eglin Air Force Base. Since laser radiation can be susceptible to propagation problems through weather, quantitative understanding of these effects is important to the development of this weapon system. Ladar image degradation, in the form of target dropouts and false returns, was evaluated in various weather conditions. Statistical analysis of the images presented expected degrees of degradation according to visibility and rain fall rate. Apparent system noise masked much of the ladar response to weather. It accounted for a dropout percentage of a maximum of 12% of the target, and a false return percentage up to 1% of the area viewed. Visibility generally less than 2 kilometers, and rain rates greater than 4 millimeters per hour were required to generate dropouts and false returns from the ladar above the system noise level. Heavy rain with rates up to 6.8 inches per hour, and thick fog with visibility down to 200 meters caused the highest percentages of dropouts and false returns. Image degradation showed a generally exponential relation to visibility and those graphs were fitted with best-guess exponential curves. However, dropouts and false returns indicated a strong linear correlation with rain rate. For the heaviest rain, correlation coefficients of 0.91 and 0.90, respectfully, were computed. Best-fit linear functions were fitted to the rain rate data.

QUANTIFICATION OF WEATHER EFFECTS

ON IMAGING LASER RADAR

I. Introduction

1.1 Background

A new revolution in surveillance technology known as imaging laser radar (ladar)

could prove just as important as the development of radar more than 50 years ago. This

emerging technology, which bounces light off targets instead of radio waves, is proving

itself capable of doing things radar cannot, such as detecting stealth aircraft, submarines

and mines under water, and clouds of poison gas or biological agents. Ladar is also

demonstrating to be arguably superior to advanced millimeter wave radar in some imaging

applications such as precision guided munitions. Ladar proponents insist it is cheaper, less

complex, and more reliable than radar, and because of its quick-scanning narrow beam

width, ladar proposes less risk of revealing its presence to the enemy (Keller 1993).

From a military operator's perspective, there are perhaps three primary advantages

over competing imaging sensors such as millimeter wave radar and forward-looking

infrared (FLIR): high resolution, signature stability, and the ability to produce a three-

dimensional image. The key to ladar's high image resolution is its short wavelength.

Image resolution produced by an active sensor is directly proportional to the wavelength.

Target signature stability may be just as important as resolution in the development of

smart autonomous munitions guidance. A stable ladar signature in an automatic target

recognition system means a more reliable match with pre-stored imaging data in all types

of environments, and thus, better chance of recognizing and ultimately destroying the

target. And finally, the ladar's ability to produce a three dimensional image increases its precision in fitting to known images by target recognition software (Keller 1993). It also allows for easier mission planning since 3-D imagery can be viewed from any aspect angle. Reconnaissance imagery can be used as templates for target recognition.

However, ladar cannot compete with millimeter wave radar on two fronts. First, radar has a longer range than ladar. Secondly, radar can operate in a more adverse environment. Millimeter wave is more all-weather and outpaces ladar with less attenuation in smoke and fog, whereas ladar can operate in adverse, but not all, weather (Keller 1993).

In spite of this potentially large drawback, the Air Force is studying ladar as the future of guidance on its precision guided munitions (PGMs). Ladar gives the Air Force an inexpensive, compact, "strap-on" guidance package which produces highly accurate autonomous target detection and allows the Air Force to minimize risk to human life with outstanding standoff capability.

A concept has been developed to circumvent ladar's inability to propagate through clouds. Using inertial navigation systems (INS) and global positioning systems (GPS), the munitions can be "flown" through weather and cloud decks down to 1500 feet above ground level where visual acquisition of the target becomes necessary. This should eliminate 90% of the weather propagation problem. The INS and GPS systems are accurate to about 10 meters, which is not precise enough for certain Air Force requirements. In addition, GPS is not useful for moveable targets. The ladar, which is accurate to less than 3 meters, will then guide the munitions to the target. The question

now becomes, "How does the other 10% of the weather propagation problem, in the form of low level precipitation and fog, affect the performance of the ladar?"

An ongoing experiment by Wright Laboratory at Eglin Air Force Base is gathering data on target detection by ladar in rain, fog, and haze conditions. This experiment uses a scanning neodymium yttrium aluminum garnet (Nd:YAG) laser at 1.06 micrometers to view a distant target. The Nd:YAG solid state laser is being developed over a more "atmospheric friendly" carbon dioxide (CO_2) gas laser because it is smaller, less expensive, and doesn't require that the detectors be cryogenically cooled like a CO_2 laser does. Along with the laser radar images, the scientists at Eglin collect meteorological data such as temperature, wind speed, wind direction, visibility, and rainfall rate. The ladar images are then paired with the concurrent weather data.

As an example, preliminary analysis has shown that when the measured visibility is 0.3 km in rain, the ladar can image the target. However, with a visibility of 1.0 km in fog, the target cannot be seen. Thus, there is no apparent general correlation between target imaging and measured visibility; fog affects the imaging differently than rain. This example clearly indicates the dilemma with imaging laser radar and its ability to image targets through weather.

1.2 Specific Problem

Degradation of the ladar's ability to image the target can occur in one of two ways. First, received images can show areas of very low or zero power return. The laser energy received at the ladar must be above a certain threshold level for detection. If it is not, the range for that laser pulse is set to the maximum range. For instance, some pixels

3

within the image of a certain target (an area of high power return) would be the same color or gray shade as the pixels indicating the sky (an area of almost no power return). The low power pixels in the area of the target are called dropouts. These occur when the transmitted laser beam is attenuated or scattered in directions other than that of the ladar, or when there is no target to reflect the laser energy. The second type of image degradation is known as a false return. These appear as pixels of relatively higher power than the rest of the target on the image. False returns occur when the laser beam is scattered back to the ladar by atmospheric constituents before it reaches the target. The goal of this thesis is to quantify adverse weather effects due to rain, fog, and haze on imaging ladar by finding relationships among weather parameters and the number of image dropouts and false returns during target imaging.

1.3 Research Objectives

Previous research and modeling have shown to predict well the transmission of a single beam laser through the atmosphere, given an adequate knowledge of the atmospheric constituents and their distributions. Very little, however, has been done to show how the atmosphere affects the images produced by a scanning ladar. This thesis evaluates the correlation of measured atmospheric parameters, rainfall rate and visibility, with the ladar's ability to image targets. This capability is determined objectively through the number of dropouts and false returns that occur on the ladar image. Analysis is done to determine the expected dropout percentage of the target and expected percentage of false returns for a given area. Additionally, confidence intervals are computed of these

4

percentages for 35 visibility intervals from 0.2 to 32 km. Finally, this thesis evaluates the correlation between the mean distance of the false returns and the weather parameters.

1.4 Scope and Limitations

The research was accomplished by comparing the number of dropouts and false returns in a given area recorded under measured weather parameters. The ladar images were not modified and the thickness of the fog and intensity of the rain could not be chosen. We were left to the mercy of Mother Nature.

The ladar hardware itself was not altered. The same sensor was used throughout the data at the same wavelength, power, pulse repetition frequency, etc. However, the targets did vary somewhat. Although each target remained fixed once it was in place, two targets were added during the year. Additionally, the area of view of the ladar varied in order to image the different targets.

The primary limitation of this thesis is the lack of reliable weather instrumentation. No fog droplet size distributions were available. In addition, the rain size distributions proved unreliable. The visibility and rain rate instruments suffered occasional failure, usually at critical data gathering times. Unfortunately, since the scientists at the Site C-3 laser lab do not own the meteorological equipment, some opportune data gathering events were missed due to circumstances beyond their control.

1.5 Overview

Imaging laser radar is being developed by the Air Force as its next munitions guidance system. This thesis explores how weather may degrade the performance of that

system. Chapter II provides background into previous research involving extinction of laser radiation by the atmosphere. Chapter III outlines the approach implemented to quantify the weather effects on ladar imaging while Chapter IV offers the results of the analysis. Finally, Chapter V presents a summary of the research, conclusions, and recommendations for further study.

II. Background

2.1 Introduction

The study of the number of dropouts and false returns of a ladar image essentially equates to understanding the extinction and scattering of the laser radiation by the atmospheric constituents. The dropouts occur because of the extinction of the radiation before it can be received, and false returns occur because the laser radiation gets scattered back to the receiver before reaching the target. Understanding these facts should make finding the proper relations easy. Unfortunately, lack of much previous atmospheric research at 1.06 micrometers and the fact than this wavelength puts us in the Mie scattering regime for fog greatly hinders any ease in finding the proper relationships between the weather and ladar image degradation.

2.2 Mie Scattering Theory

Mie scattering theory is the analytical solution of radiation scattering by spherical particles. Rayleigh approximations of the Mie equations describe scattering of electromagnetic energy by atmospheric particles much smaller than the wavelength. Methods of geometric optics can be used for scattering by particles much larger than the wavelength. However, when the scattering particles are comparable in size to the wavelength, the full Mie regime principles must be used, which are highly complex. The largest atmospheric scatterers, raindrops and hailstones, are treated as Mie scatterers at millimeter wavelengths. Most other scatterers, such as fog and haze, are treated by the Rayleigh approximation at far infrared wavelengths and Mie scattering at near infrared

wavelengths. The wavelength of the ladar being tested, 1.06 μm, is comparable to usual fog droplet sizes of 0.3 to 14 μm. Thus, Mie theory is used to calculate its scattering (Kyle 1991).

Mie theory results from solving Maxwell's equations for the interaction of an electromagnetic wave of wavelength λ with a spherical particle of radius r. The particle, such as a fog droplet or raindrop, has an index of refraction m, which is real or complex ($m = 1.33$ is used for water in the near infrared). One very important index stemming from these parameters is called the size parameter x, where

$$ x = \frac{2\pi r}{\lambda} $$

The size parameter determines when we are in the Rayleigh, Mie, or geometric optics regime. Using the Rayleigh approximation when x is less than 0.3 introduces almost no error in the extinction cross section. However, when x is 1.0, over 10% error exists between the Mie and Rayleigh solutions, jumping to 100% error when x is greater than 3.0 (Kyle 1991). Therefore, the complex Mie equations must be solved for larger size parameters. For a size parameter of 50 or greater, scattering is largely independent of wavelength and the principles of geometrical optics can be used.

Many texts give a full derivation of the Mie equations. Chapter 4 of Bohren and Huffman (1983) gives a detailed derivation while Kyle, on pages 124-139, shows a sufficient, but general overview. To get a brief understanding of Mie theory, Fleagle and Businger tell us:

> The more complete Mie theory shows that the ratio of scattered energy to the incident energy intercepted by the geometrical cross section of the particles is given by

$$2\left(\frac{\lambda}{2\pi r}\right)^2 \sum_{j=1}^{\infty}(2j+1)\{|a_j|^2+|b_j|^2\}$$

where r is the particle radius, λ is the wavelength, and a_j and b_j are functions of spherical Bessel functions and Hankel function of the second kind with complex arguments. The first three terms of the series representing the energy received at distance d and angle $\theta = \pi/2$ (forward or backward scatter) can be expressed as proportional to

$$\frac{r^6}{d^2\lambda^4}\left(\frac{n^2-1}{n^2+2}\right)^2\left\{1+\frac{6}{5}\left(\frac{n^2-2}{n^2+2}\right)\left(\frac{2\pi r}{\lambda}\right)^2+\frac{9}{25}\left(\frac{n^2-2}{n^2+2}\right)\left(\frac{2\pi r}{\lambda}\right)^4+...\right\}$$

,

where n is the complex index of refraction. The first term of this series represents Rayleigh theory. The second term becomes significant for r/λ greater than about 0.1, so that Mie theory is necessary for particles of this size or larger. (Fleagle and Businger 1980).

To show that we are in the Mie regime at a wavelength of 1.06 μm, it is enough to work with parameters that tell about the scattering over all directions. The extinction efficiency is the energy removed from the incident beam divided by the geometric cross section of the scattering particle. If we take the incident beam to have unit intensity (power per unit area), the extinction efficiency Q_{ext} and the extinction cross section σ_{ext} are

$$Q_{ext} = \frac{2}{x^2}\sum_{n=1}^{\infty}(2n+1)\,\mathrm{Re}(a_n+b_n)\ , \text{ and}$$

$$\sigma_{ext} = \pi\, r^2\, Q_{ext},$$

where r is the radius of the scatterer, x is the size parameter, and $a_n,\ b_n$ are the expansion parameters satisfying Maxwell's equations. The efficiency is the factor by which the actual geometric cross section must be magnified or diminished to produce the observed extinction (Kyle 1991).

The other two important parameters are the scattering efficiency and absorption efficiency. The scattering efficiency, given by

$$Q_{scat} = \frac{2}{x^2} \sum_{n=1}^{\infty} (2n+1)\left(\left| a_n \right|^2 + \left| b_n \right|^2 \right)$$

is the area of incident radiation that appears to have been scattered over the geometric cross section of the scatterer. Since the absorption cross section is the difference between the extinction and scattering cross sections,

$$\sigma_{abs} = \sigma_{ext} - \sigma_{scat},$$

and the absorption efficiency is likewise related by

$$Q_{abs} = Q_{ext} - Q_{scat}$$

since $Q = \dfrac{\sigma}{\pi r^2}$ (Kyle 1991).

These efficiencies are almost always zero when the size parameter is very small. This means that the particles scatter much less radiation than their physical cross section intercepts. Then, as the particle radius increases, so too does the efficiency. For particles that are nonabsorbing, the extinction and scattering efficiencies will rise until they oscillate around two (Kyle 1991). Figure 2.1 shows the extinction efficiency as a function of particle radius, which was calculated using Bohren and Huffman's Mie scattering calculation program *bhmie.exe*. The wavelength used is 1.06 μm with a refractive index for water of 1.33.
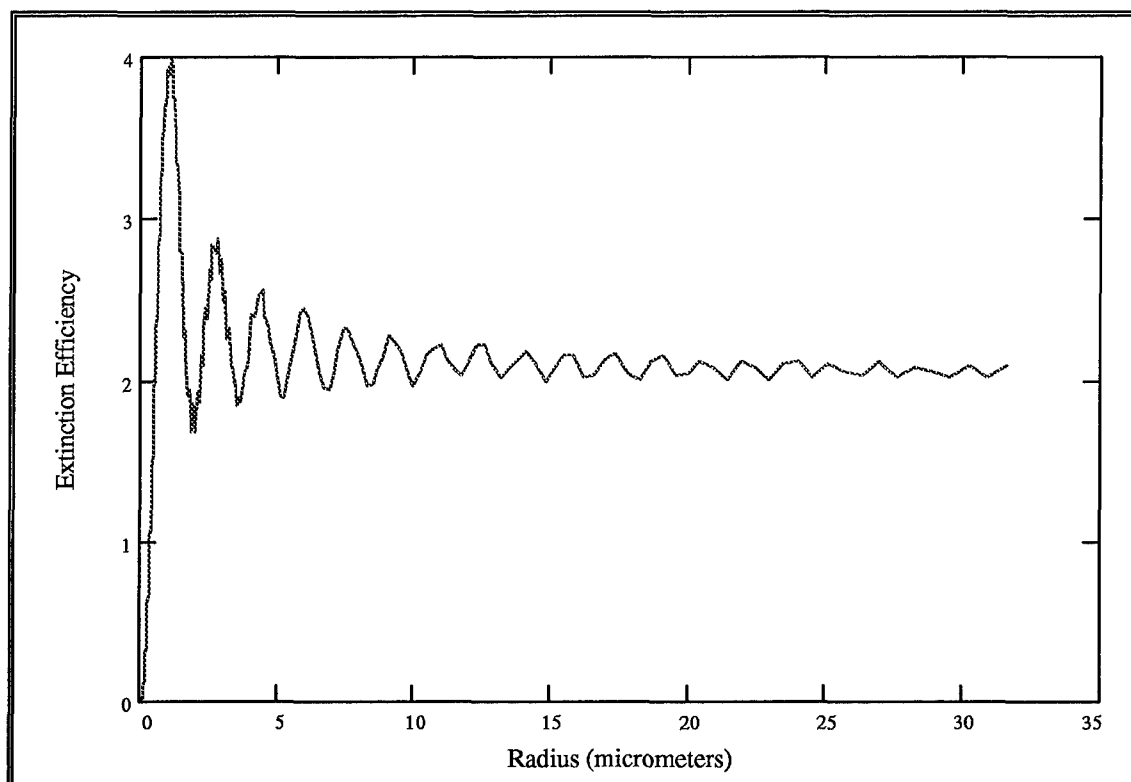
Figure 2.1 Extinction Efficiency vs. Particle Radius

It seems illogical that a particle can scatter twice as much radiation as its area, but there is an explanation. The incident light on the particle scatters because the particle is nonabsorbing. It then interacts with non-scattered radiation, which means more radiation is affected by the presence of the particle than the radiation intercepted by the cross section. This, plus the radiation scattered by the edges of the particle, makes an extinction and scattering efficiency of two not too unreasonable (Kyle 1991).

The oscillation of the extinction and scattering efficiencies about 2 is a type of resonance. For this reason, they can show fluctuations for usual fog droplet sizes of 0.3 to 14 μm at a wavelength of 1.06 μm, which give size parameters from 1.7 to 26. This in turn can lead to fluctuations in the extinction and scattering of laser light, which in this experiment manifests itself as fluctuations in dropouts and false returns on images.

11

2.3 Fog Attenuation

Fog is almost always characterized by its optical visibility. Unfortunately, this description is inadequate since fogs of different liquid water contents (LWCs) and fog droplet size distributions can have the same visibility. Advection fog, which forms over water and advects onto land, can have five times the LWC as radiation fog, which forms from the nighttime cooling of land under moist, warm air, while having the same visibility conditions. Since the LWC largely determines fog's attenuation at infrared frequencies, with LWC proportional to attenuation, fogs with identical visibility but different size distributions and LWC can produce different attenuations (Jelalian 1992).

2.3.1 Chylek, 1978

Chylek was first to show that an unambiguous relation between extinction and LWC, independent of the shape of the droplet size distribution, exists at some infrared wavelengths. The liquid water content W and extinction coefficient k are given by

$$W = \frac{4}{3}\pi\rho \int r^3 \, n(r)dr$$

$$k(\lambda) = \int \sigma_{ext}(\lambda,r) \, n(r)dr$$

where ρ is the water density, λ is the wavelength of the radiation, n is the number density, and $\sigma_{ext}(\lambda,r)$ the extinction cross section as discussed earlier. First, Chylek shows derivations of three relations between k and W using various substitutions and assumptions, none of which yield a suitable relation independent of size distribution (Chylek 1978).

12

Next, he proposes that the extinction efficiency Q_{ext} can be approximated by a straight line up to a given maximum fog droplet radius (and its maximum size parameter x) as indicated on Figure 2.2. The equation for this line is given by
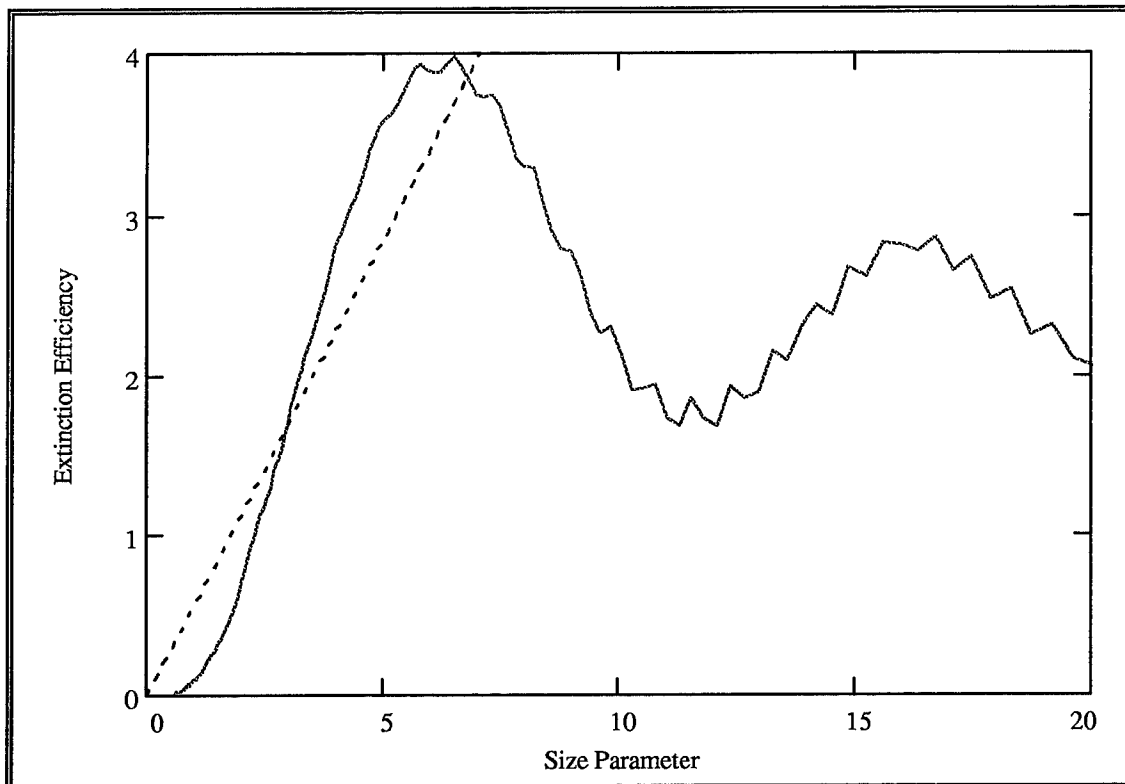
Figure 2.2 Extinction Efficiency vs. Size Parameter

$$Q_{ext} = cx$$

where c is the slope of the line approximating Q_{ext}. This approximation overestimates the exact Q_{ext} value at some values of x and underestimates it at others. Consequently, these two errors tend to cancel each other in the integral. With this approximation he obtains

$$W = \frac{2\rho \lambda k}{3\pi c}$$

which relates LWC to extinction coefficient independently of the droplet size distribution. Chylek then shows the wavelengths at which a linear k-W relationship exists for a given

13

maximum droplet radius in a distribution, and the appropriate parameter c. For a wavelength of 0.5 μm the maximum radius for which the $Q_{ext} = cx$ approximation is valid is 0.5 μm. The corresponding parameter c is 0.61. At a wavelength of 1.2 μm, the maximum radius for validity is 1.2 μm, also with a c parameter of 0.61. Thus, for normal fog droplet distributions where the bulk of radii are greater than 1.2 μm, this approximation is not valid for these two wavelengths (Chylek 1978).

To verify this k-W relation, Chylek plots data from over 300 different size distributions of clouds and fog at wavelengths of 0.55 μm and 11μm. The longer wavelength fits the approximation very well, but no unique relationship between extinction coefficient and liquid water content exists for the shorter wavelength. Therefore, the linear relation for liquid water content and extinction coefficient can be size distribution independent, but it is not independent of wavelength (Chylek 1978).

2.3.2 R.G. Pinnick, et al., 1978

In this paper, Pinnick et al. examine the vertical structure of fog and haze and relates their effects to extinction over various wavelengths. Although the vertical profile of the fog distributions is not of consequence in this experiment, some other conclusions do lend relevance.

Measurements of fog distributions taken over eight days near Grafenwöhr, Germany using impaction and light scattering techniques showed a bimodal distribution of droplet radii. The larger particle mode had a mean radius of 5μm with a standard deviation of 1.6. The smaller mode indicated means of 0.3 to 0.6 μm with standard deviations from 1.8 to 2.5 (Pinnick et al. 1978).

The authors also investigated Chylek's approximation of a linear relation between extinction coefficient and liquid water content. At 10 μm, Pinnick et al. conclude that a size-distribution-independent linear relationship exists between extinction coefficient and liquid water content. Oddly, the data indicate such a relationship at 0.55 μm, 1.2 μm, and 4 μm as well. However, the authors investigated empirical relations determined by others for fog measurements made under different meteorological conditions at different geographic locations. They found extinction coefficients differing by nearly an order of magnitude and conclude those differences are due to varying droplet size distributions. Thus the similarity of the authors' results at 0.55 to 4μm is due to the homogeneity of their fog droplet distributions (Pinnick et al. 1978).

2.3.3 Pinnick and Chylek et al., 1979

In a study using 341 fog droplet size distributions, the authors verified the previous work of Chylek in 1978 with regards to the linear relation between extinction and liquid water content at wavelengths around 11μm, independent of droplet size distribution. Additionally, they determined a linear relation between absorption and water content at wavelengths of 3.8 and 9.5 μm (Pinnick and Chylek et al. 1979).

However, the authors did show that at 0.55 μm, the relation between extinction coefficient and liquid water content is in fact dependent on droplet size distribution, contrary to the conclusions about longer wavelengths. They also investigated wavelengths of 1.2 and 4 μm. They noted that the $Q_{ext} = cx$ relation better approximates the exact numerical solutions as wavelength increases, although still not sufficiently so at 1.2 μm.

At this wavelength the extinction is largely overestimated (Pinnick and Chylek et al. 1979).

2.3.4 Tonna, 1991

In his paper, Tonna studies relationships among backscattering coefficient, extinction coefficient, and liquid water content in fogs for lidar systems at forty wavelengths from 0.25 to 12 μm. Using 239 droplet size spectra, the Tonna finds both power-law and linear relations for backscattering (β) versus extinction (σ_{ext}), a power-law relation for water content (W) versus σ_{ext}, and one as well for $\sigma(.55 \ \mu$m) versus σ_{ext}. Although the intent of the study is to locate those wavelengths most suitable for inferring extinction, liquid water content, and visibility vertical profiles in fog, the specific calculations for $\lambda = 1.06 \ \mu$m are of consequence here (Tonna 1991).

For each droplet radius distribution n(r) and wavelength, the following quantities were computed:

the volume extinction coefficient $\sigma(\lambda)$ given by

$$\sigma(\lambda) = \int_{r_m}^{R_m} \pi \ r^2 \ Q_{ext}[r, m(\lambda)] \ n(r) \ dr ,$$

where r_m and R_m are the lower and upper radii of the n(r) considered, Q_{ext} is the efficiency factor for extinction, and $m(\lambda)$ is the complex refractive index of water;

$\beta(\lambda)$, the volume backscattering coefficient given by

$$\beta(\lambda) = \frac{\lambda}{4\pi^2} \int_{r_m}^{R_m} \frac{i_1[\pi_1\, r_1\, m(\lambda)] + i_2[\pi_2\, r_2\, m(\lambda)]}{2} n(r)dr,$$

where i_1 and i_2 are the Mie intensity function for light scattered at $\theta = \pi$, and

W, the liquid water content (Tonna 1991).

Data elaboration consisted of:

(1) determining the mean β and σ_{ext} at each wavelength and the relevant dispersion

coefficient, which is the standard deviation divided by the mean value, in percent.

(2) fitting the (β, σ_{ext}), (W, σ_{ext}), and [$\sigma(.55\ \mu m)$, σ(for each wavelength)] data points

with power-law functions of the form $y = cx^k$ and determining the relevant correlation and

dispersion coefficients; and,

(3) fitting the above data points with straight lines and determining the differences

between the linear and non-linear functions.

For $\lambda = 1.06\ \mu m$, Tonna determines that the (β, σ_{ext}) relationship is given by

$$\beta = c_1 \sigma^{k1},$$

where β is in $m^{-1} sr^{-1}$ and σ is in m^{-1}, with $c_1 = 0.03584$ and $k1 = 0.903$. This equation is

determined to be reliable since the corresponding correlation and dispersion coefficients

are 0.962 and 18.25 % respectively.

The (W, σ) curve is shown to be

$$W = c_2 \sigma^{k2}$$

At the 1.06 μm wavelength, the best-fit parameters are $c_2 = 3.223$ and $k2 = 0.838$. A correlation coefficient of 0.863 is determined with a dispersion coefficient of 34.56 % , indicating relatively poor accuracy for this curve.

Finally, the data are fit to the curve for the [σ(.55 μm), σ] relationship given by

$$\sigma(.55 \ \mu m) = c_3 \ \sigma^{k3}$$

The parameters c_3 and $k3$ for 1.06 μm are not specifically given in this paper. However, an equally accurate linear relation is determined where

$$\sigma(.55 \ \mu m) = a_3 \ \sigma$$

Substituting Koschmeider's relation for visibility,

$$V = 3.912 / \sigma(.55 \ \mu m)$$

and $a_3 = 0.979$ for the wavelength in question gives

$$V = 3.996 / \sigma$$

at 1.06 μm (Tonna 1991).

Comparisons between the linear fits and non-linear fits for each relation indicate a general improvement in correlation and dispersion with the power-law curves. The β-σ relation has mean improvements of 3.8% and -2.6% in correlation and dispersion respectively. For the W-σ relation the mean improvements were 6.5% and -2.1%, while the σ(.55 μm)-σ relation had small improvements of 1.3% and -1.4% in correlation and dispersion (Tonna 1991).

2.4 Rain Attenuation

2.4.1 Jelalian, 1992

The data on ladar performance in rain given by Jelalian in his textbook are somewhat limited. He shows in one table that a medium rain of 12.5 mm hr^{-1} has an attenuation coefficient of 5.5 dB km^{-1} for wavelengths from 0.7 μm to 0.3 cm. However, he then shows a graph of rain rate versus attenuation coefficient from other works at wavelengths of 0.63 and 10.6 μm. The best-fit curve gives the equation

$$\alpha = .29 + \frac{R}{2.53} - \left(\frac{R}{20.3}\right)^2$$

where α is the attenuation coefficient in dB km^{-1} and R is the rain rate in mm hr^{-1}. From this equation a rain rate of 12.5 mm hr^{-1} yields an α of 4.85 dB km^{-1} and not 5.5 dB km^{-1} as mentioned earlier (Jelalian 1992).

Later in the text, Jelalian calculates the range performance of a 1.06 μm ladar as a function of atmospheric conditions in detecting a target with a cross section of 1 square meter. In a 4 mm hr^{-1} rain, the target is detectable at 7 km. In a rain rate of 20 mm hr^{-1}, that detection range is about 2.5 km. Although Jelalian does not give a definition of "detectable", this data gives an indication of the detection capabilities of ladar through increasing rain rates (Jelalian 1992).

The previous research shown in the literature elicits some expectations of what we might find in our work. The research shows that extinction of infrared radiation is linearly related to the liquid water content of fog. Therefore, we might expect to find linear relations between image degradation and rain rate, which is proportional to liquid water content. Also, the extinction coefficient, which we can relate to dropouts, is non-linearly

related to visibility. Therefore, we might expect a non-linear relation between dropouts and visibility.

This concludes the summary of previous work in the area of laser performance through fog and rain. The next chapter addresses our approach to assessing the relations between weather and dropout and false return rates, as well as analyzing their significance in image degradation.

III. Approach

3.1 Introduction

To quantify how weather degrades laser radar images, we must complete three general processes. First, an assessment is made of the image degradation. Using programs created with a graphical programming software package, each image generated by the ladar is analyzed for the number of dropout pixels from two targets, as well as the number of false return pixels for a given area. Next, the images with their dropouts and false returns are paired with their corresponding weather data. The raw weather data are deciphered and coupled with the image data taken to the nearest minute. Finally, statistical analyses are performed to determine how the meteorological variables influence the degradation of the ladar images. Equations which quantify this influence are proposed and evaluated.

3.2 Image Data Analysis

Operation of the ladar takes place at Site C-3 on the grounds of Eglin Air Force Base, Florida. The range itself is an open field roughly 0.5 km wide and 1.5 km long with various targets placed about in the field of view of the ladar. These include a watch tower, a tank, two small sheds, two large resolution panels, and several tall poles. Chain link fences also run through the area behind the targets. The range ends roughly 1.5 km away with a line of tall pine trees. The ladar itself sets on ground level inside a laser radar facility at the boundary of the range. The nearest target is about 200 m away. Figure 3.1

is a picture of the range. The two large panels are between the tallest poles with the tank and small sheds to the left.
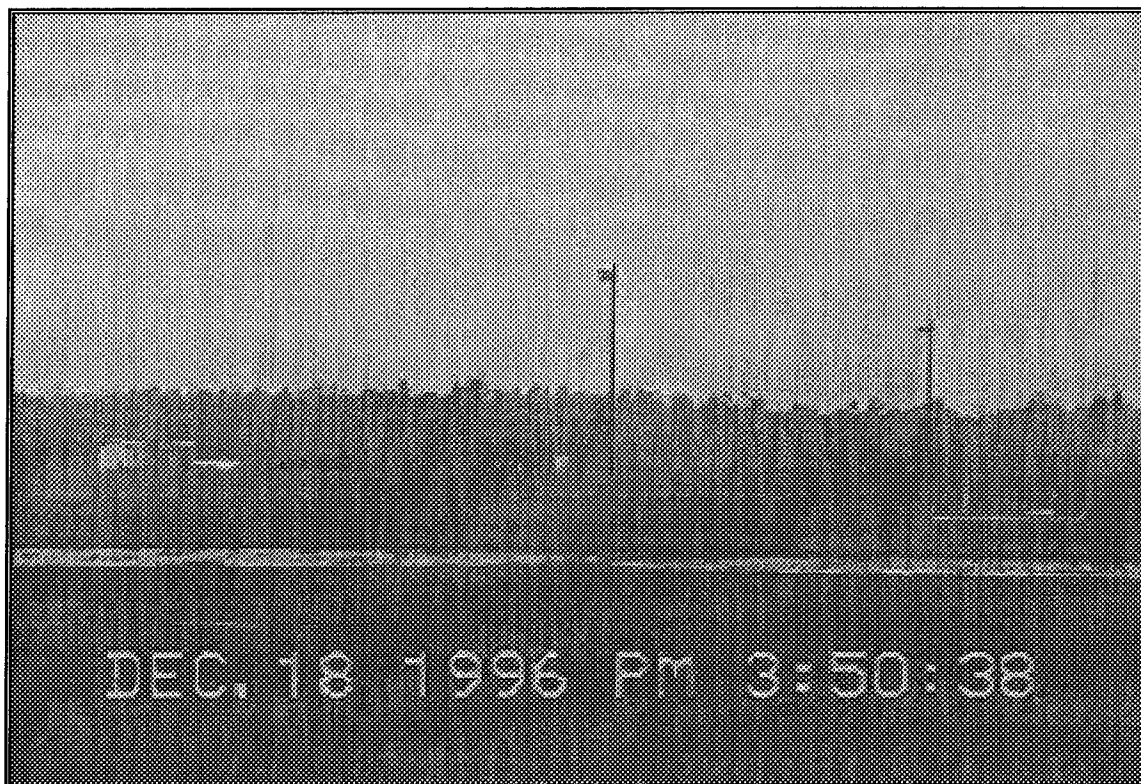
Figure 3.1 Television Picture of the Laser Range

The images used in this thesis were created by the Swartz Electro-Optics imaging laser radar. It uses a solid-state Nd:YAG laser operating in a pulsed wave mode at 1.064 µm. The diameter of the laser beam, which is defined as twice the distance from the center of the beam to where the power falls off by a factor of 1/e, is 1 cm. The power output is 25 microjoules. It has a pulse width of 15 nanoseconds, and the pulse repetition frequency is 50 kilohertz. It requires approximately 90 seconds to complete its full scan and create an image. (Kimmet 1996)

The ladar images were taken over 8 different days in 1996, in various types of weather. Table 3.1 presents a brief description of the weather regime for those days.

Table 3.1 Overview of the Weather Regimes

Date	Weather
15 March 96	Thick fog
25 March 96	Heavy rain and fog
29 March 96	Light fog
4 April 96	Light fog
30 October 96	Moderate fog
2 November 96	Light rain and fog
6 December 96	Moderate fog
18 December 96	Light rain and fog

The number of images taken per day varies due to the weather. Images were generated as long as the weather persisted. Since fog usually dissipates after a couple of hours and rain can last a much longer time, the fog days had fewer images. On 30 October 14 images were taken, which was the least, while 25 March had the most taken with 89.

The raw image data is viewed and stored as a binary data file on a floppy disk by a software program called *Oscardsp.exe*. This menu-driven system will display the images in color, with the various colors indicating their range from the ladar. It also stamps each image with the date and time to the second at which it was completed. With the images saved on disk, they can then be read by a software program to count the dropouts and false returns on each image.

The software package we used for counting is a graphical programming language called *Labview*. Two programs were developed to perform the counting tasks. The first, *Dropout.vi*, reads and displays the ladar image data from the disk. Cursors are then placed wherever the user desires on the image, creating a box around the desired target. An example of *Dropout.vi* viewing the tank target is given in *Appendix A*. *Labview* then

counts the number of pixels (dropouts) above a certain distance threshold that the user sets. Dropouts are pixels assigned to the maximum range of the ladar, which is 1.2 km. In this case the targets being imaged were in the 500 to 600 m range. The dropout threshold was set to 700 m in order to guarantee that no target pixels were included in the counting. Any pixel within the cursors that indicated a distance greater than 700 m was counted. The second program, *Falsrtn.vi,* counts the number of pixels within the cursor field that are below the user-defined range threshold. In this analysis, the false return threshold was set to 600 m, indicating that any pixels shown to be less than 600 m were counted as false returns. The false return analysis looked at an area of the sky only which ideally returns no power. For each image, both programs record the following information: total number of dropouts or false returns, the mean value of their distances, the standard deviation, and the variance of those distances.

With *Dropout.vi* we looked at two different targets on each day (except for 15 March). For the March and April data, we looked at a small building and a tank. On 15 March, we looked at the building only, since the tank was not yet placed on the range. The building target is about 2.4 m wide by 2.9 m high, and 548 m from the ladar. The tank is 7.6 m long, 4.3 m wide, 3.7 m high, and located 492 m from the ladar. On 30 October and 2 November, the ladar imaged the tank and two large resolution panels. The small buildings were outside of the field of view. The right panel, which is 8.8 m long, 4.8 m high, and 525 m from the target, was used in this analysis. The ladar imaged all three targets on 6 December and just the tank and panel on 18 December.

Cursor placement on the *Labview* screen determined an upper bound to the total number of dropouts. The building was 33 pixels wide by 12 pixels long for a total of 396.

The panel was 67 x 22 pixels for a total of 1474. Since the building and panel are rectangular the cursors were placed to match the edges exactly. The tank was 57 x 12 pixels for a total of 684. However, since the tank is not rectangular, the cursors could not match the edges exactly. Areas of background sky can be seen above and below the gun barrel. Because of this there is a baseline of roughly 100 dropouts on each tank image. This becomes a minor detail in the dropout analyses that deal with relative trends. However, for the analyses that incorporate the dropout percentage of the target, the baseline number of dropouts will be subtracted.

The target used in *Falsrtn.vi* is a large area of open sky. Since we are counting returns in an area where there should not be any, this is a logical choice. The sky area counted on most images was 380 x 100 pixels, for a total of 38,000. The areas on 2 November, 6 December, and 18 December were 26508, 37700, and 39750 pixels respectively.

Quality control of the images was necessary due to the effects of ladar sensor failure. When the ladar operated improperly large "blacked-out" areas appeared on the image. If these areas were in the vicinity of the target, the image was not used for fear of biasing the dropout or false return count. From the eight useable days of data 15 images out of a total of 325 were discarded. In addition, an entire seventh day of data, 5 April, was not useable due to sensor failure.

The text files created by *Labview* were imported into *Excel* spreadsheets. Image numbers, times, and appropriate labels were added to create a summary of target dropouts, tank dropouts, and false returns for each day. At this point, the data sets were ready to be married with the appropriate weather data and analyzed.

3.3 Weather Data

The ladar range at Eglin AFB contains an instrument package that measures a wide array of meteorological variables. Those pertinent to the ladar performance are visibility, rainfall rate, aerosol size, and rain drop size.

3.3.1 Instrumentation

The instrumentation package consists of duplicate instrument sets, one set close to the ladar, and one near the targets. The near sensor group is located 60 m from the ladar and the far sensor group is 600 m away. Both measure rain rate, visibility, rain drop size, and aerosol size. Additionally, the near sensor measures temperature, dew point, pressure, wind speed, and wind direction. Unfortunately, having two sensors contributes to the complexity and variability of the data analysis. However, since fog can be very nonuniform over small distances, an average of both sensors proves quite useful.

Visibility values are determined by a forward scatter visibility sensor that measures atmospheric optical extinction coefficient. An array of infrared diodes illuminate the sample volume of the atmosphere with a narrow-band optical radiation centered at a wavelength of 950 nanometers. The optical energy scattered by interaction with particles in the sample volume is measured at a principle scatter angle of 35 degrees. Calculations performed using this parameter yield an absolute extinction coefficient which is then related to visibility by Koschmeider's formula. The range of the instrument is 160 m to 32 km. (Metvan Instrument Pamphlet 1995).

Rain rate is measured by Scientific Technology Inc.'s ORG-705 Optical

Precipitation Gauge. This instrument measured rainfall by "detecting the optical

irregularities induced within the sample volume by precipitation particles falling through a

beam of partially coherent infrared light. These irregularities are known as scintillation.

By detecting the intensity of the scintillations which are characteristic to precipitation, the

actual rainfall rate can be determined" (Metvan Instrument Pamphlet 1995). Output of the

ORG-705 is given in voltage that is proportional to the log of the rain rate such that

$$\text{Rain rate [mm hr}^{-1}] = 10^{x}$$

where x = (output voltage - 0.65). The measurement range is from 0.1 to 1000 mm hr^{-1}.

It is accurate to 1% from 10 to 100 mm hr^{-1}and accurate to 4% elsewhere. (Metvan

Instrument Pamphlet 1995).

The Ground Based Precipitation Probe is a complete spectrometer probe which

measures raindrop particle diameter. The raindrops are sized using an array of

photodiodes which sense the shadows on array elements left by particles passing through

its field of view. The raindrops are illuminated by a He-Ne laser and imaged as

shadowgraphs onto the photodiode array. The particle size is determined from the

magnification of the optical system, the spacing of the array elements, and the number of

elements shadowed by a raindrop's passage. The size range is from 0.2 to 12.4 mm,

divided into 64 equally spaced bins. (Metvan Instrument Pamphlet 1995).

Finally, fog droplet sizes are measured by the Classical Scattering Aerosol

Spectrometer Probe. It has a useful total range of 0.3 to 20 μm, with four selectable

subranges divided into 15 bins each. The four subranges are 0.3 to 0.75 μm, 0.5 to

2.75 μm, 1.0 to 12.5 μm, and 2.0 to 20.0 μm. Unfortunately, none of these ranges can

completely describe a typical fog droplet spectrum. However, for some unknown reason, the instrument failed to give readings of any droplets at all. Fog droplet spectra are necessary in the calculation of extinction and lack of this data greatly hinders this research.

Overall, reliability of the entire instrument package, and accuracy of some of the readings was suspect. On March 25, the most data-rich day, a cloud-to-ground lightning strike on the range caused the weather instrumentation to fail. The rain rate sensors worked intermittently, stopping altogether for a period of seven minutes before the near sensor resumed. The far sensor did not resume operation for 23 minutes after that. The far visibility sensor ceased operation at 9:28 AM and the near visibility sensor stopped at 10:38 AM; the weather event continued past noon. Thus, valuable visibility data was not available for half of the event. In addition, other data collection opportunities had to be passed up due to complete weather instrumentation failure, again due to lightning.

3.3.2 Data Format

The raw weather data were saved as ASCII files with the time, sensor code, and sensor reading. The collected data must be decoded and converted (in the case of rain rate), and put into a useful format. The instruments gave readings once every minute and the stamped times were rounded to the nearest whole minute to coincide with the image times. The refined weather data are then put into an *Excel* spreadsheet and married with the image data to give a complete picture of the data collection. An example is given in Table 3.2.

Table 3.2 Example of *Excel* Weather and Dropout Summary for 30 October

Time	Rain Rate	Avg Vis	Temp (°F)	Dew Pt (°F)	Press (mb)	File	# of Drop outs	Mean Value	Std Dev	Var	Target Status
6:17	0.0	0.9	69	69	1011	1	876	1251.2	8.3	68.4	top 1/3 visible
6:20	0.0	0.4	69	69	1011	2	721	1252.7	6.9	47.9	top 1/3 visible
6:21	0.0	0.4				3	679	1253.7	4.6	21.1	top 1/3 visible
6:23	0.0	0.3				4	538	1253.8	4.3	18.3	top ½ visible
6:25	0.0	0.3				5	424	1253.3	12.6	159.6	top 2/3 visible
6:27	0.0	0.2				6	233	1254.4	2.9	8.6	top 4/5 visible
6:29	0.0	0.3				7	215	1253.6	17.4	303.2	all visible
6:31	0.0	0.4	69	69	1011	8	133	1255.0	1.8	3.4	clear
6:33	0.0	0.6				9	163	1251.3	30.5	933.8	clear
6:34	0.0	0.7				10	28	1253.3	6.4	41.9	clear
6:36	0.0	0.5				11	84	1211.1	98.2	9756.1	clear
6:38	0.0	0.7				12	5	1255.8	0.6	0.5	clear
6:40	0.0	3.0			1011	13	70	1194.6	112.0	12718.7	clear
6:42	0.0	5.6				14	6	1255.5	0.0	0.0	clear

3.4 Statistical Analysis

Once the image and weather data for each day have been counted, decoded, converted, and properly formatted, they can be imported into the proper software and analyzed. The intensive analysis of the data encompassed several techniques and *Mathcad 6.0 Plus* was used as the primary tool.

3.4.1 Graphical Analysis and Equation Fitting

In order to receive sufficient understanding of the data, several different graphs were produced for each day. Dropouts and false returns were shown as time lapses with rain rate and visibility to show correlations between maxima and minima. The set of time series graphs is located in *Appendix C*.

Dropouts and false returns were also shown as functions of visibility and rain rate (where applicable) to show how the weather parameters affect image degradation. Best-

fit linear and non-linear equations were then applied to the graphs with distinct shapes.

The linear equations were produced using the *slope* and *intercept* functions of *Mathcad*.

The non-linear equations were estimated with a best guess exponential function. Since we

do not have reliable data on the nature of the weather parameters (specifically, droplet size

distributions), we cannot in good faith say that those functions are how the weather affects

image degradation. The non-linear curves are only fitted in order to show similarity in the

shape of the dropout and false return plots.

3.4.2 Correlation Coefficients

The simplest possible relationships between ladar image degradation and weather

parameters is a linear one. This would indicate a direct proportionality of one variable to

another, in other words, a perfect linear correlation. The statistical parameter known as

the correlation coefficient determines the degree of linearity of the relationship between

two variables. For each set of dropout and false return data versus weather parameters,

correlation coefficients were computed to determine the degree of *linear* correlation of the

data. The equation for the correlation coefficient of a sample of n pairs of data

$(x_1,y_1)\ldots(x_n,y_n)$ is given by

$$r = \frac{n\sum x_i y_i - (\sum x_i)(\sum y_i)}{(\sqrt{n\sum x_i^2 - (\sum x_i)^2}) * (\sqrt{n\sum y_i^2 - \sum y_i^2})}$$

A reasonable rule of thumb is to say that the linear correlation is weak if $0 \leq |r| \leq 0.5$,

strong if $0.8 \leq |r| \leq 1$, and moderate otherwise (Devore 1995). Coefficients of around 0.70

and higher indicate good linear correlation and therefore a linear function should provide a

good fit to the data. Data sets satisfying this condition were fitted with approximate lines.

It is important to remember that a correlation coefficient near 0 is not evidence of the lack of a strong relationship, but only the absence of a linear one.

3.4.3 Visibility and Degradation Percentage

For the data sets which showed a non-linear relationship, some miscellaneous analyses were performed. Since non-linear equation fitting can be difficult, it proved worthwhile to determine what percentage of the target would dropout as a function of visibility. This analysis enabled us to combine building, tank and panel targets over all days and determine the mean percentages and standard deviations for a chosen visibility interval. Ninety-five percent confidence intervals were computed as well. It is important to note the true interpretation of confidence interval. It means that if this experiment is performed over and over, the true value of the mean dropout percentage will be within that interval 95% of the time (Devore 1995). This percentage analysis was also performed on false returns for the same visibility intervals.

3.4.4 Mean Distance of False Returns

One of the parameters that *Falsrtn.vi* tabulated was the mean distance of the false returns for each image. It is useful information to the sponsors of this thesis to know what the expected distances of the false returns are. Therefore, an analysis of the mean distances and standard deviations was performed for each day of data.

This concludes our presentation of the approach used in this thesis effort. The next chapter will present the results generated by this approach.

IV. Results

4.1 Introduction

This chapter presents results of the ladar image degradation analysis described in Chapter 3. It includes weather data analysis and determination of its trustworthiness, determination of the linear correlation between weather variables and image degradation, and analysis of dropout and false return percentages for 35 visibility intervals between 0.2 and 32 km. These results provide insight into the significance of weather impacts on laser imaging radar and its viability as an all-weather guidance system.

Before delving into the quantitative information contained herein, it is important to have a general idea of the weather that occurred on each day during data collection. Table 4.1 provides an overview of the weather that transpired.

Table 4.1 Overview of the Weather Regimes

Date	Weather
15 March 96	**Thick fog.** Visibility decreased to 0.2 km for extended periods
25 March 96	**Heavy rain (thunderstorm) and fog.** Rain rates briefly reached 173 mm hr^{-1} (6.8 in hr^{-1}) and visibility fell to 0.2 km
29 March 96	**Light fog.** Average visibility greater than 12 km (7 mi)
4 April 96	**Light fog.** Average visibility greater than 20 km (14 mi)
30 October 96	**Moderate fog.** Visibility briefly down to 0.2 km
2 November 96	**Light rain and fog.** Rain rates less than 5 mm hr^{-1} (0.2 in hr^{-1}), visibility greater than 2.5 km (1.5 mi)
6 December 96	**Moderate fog.** Visibility briefly down to 1.1 km (.7 mi)
18 December 96	**Light rain and fog.** Rain rates less than 5 mm hr^{-1} and visibility greater than 4 km

4.2 Weather Data Analysis

4.2.1 Sensor Correlation

On the first four weather days, two groups of sensors were recording weather conditions, one approximately 60 m from the ladar, and one 500 m away. On the last four days, only the far sensor package was operating. When both operated correctly, averages of the sensors were used. We would assume that over such a small distance (for meteorological scales) the two sensors would give nearly identical readings. Figure 4.1 shows rain rate readings for both sensors on 25 March. Their peaks are well matched and their correlation coefficient is a very strong 0.85. On rain days, the near and far rain rate sensors differed little overall in their readings.
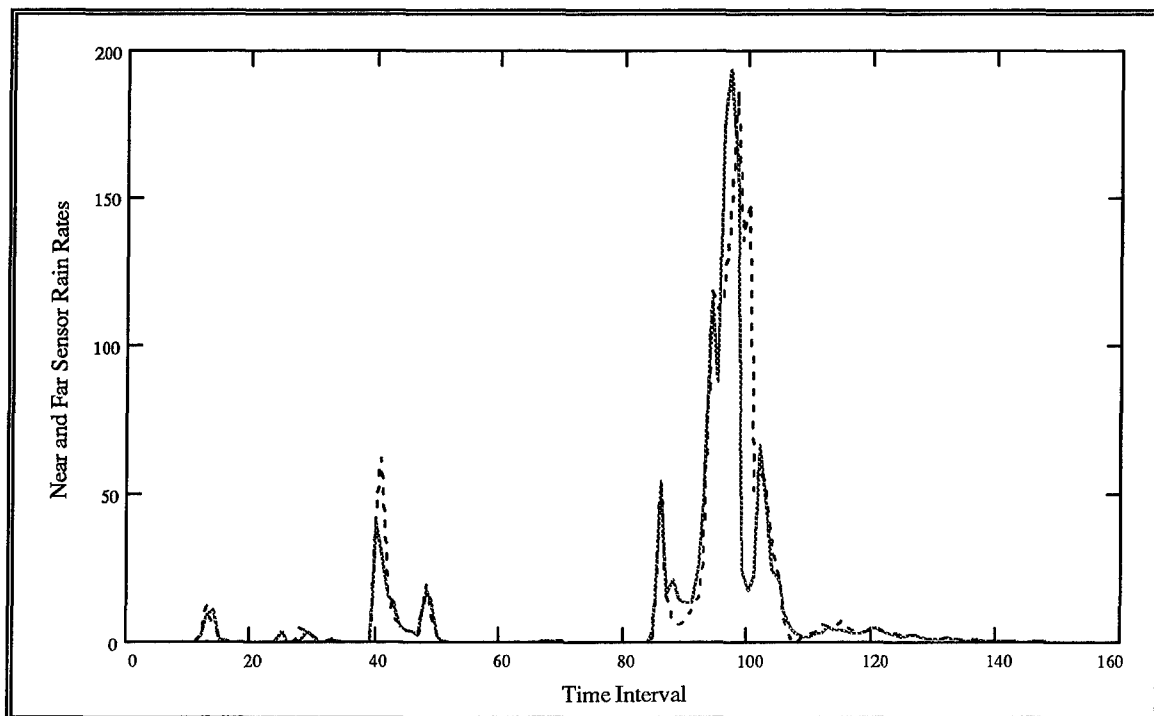

Figure 4.1 Comparison of Near (solid line) and Far (dashed line) Rain Rate Sensors (mm hr $^{-1}$) for 25 March (heavy rain)

However, for the visibility sensors this was far from the case. Figure 4.2 shows visibility readings for 25 March and Figure 4.3 shows the same for 4 April. Here the sensor data vary dramatically. The 25 March graph shows a pronounced lag time of 3 minutes between peaks in the graph. On 4 April, the far visibility sensor read a constant 32 km while the near sensor varied. The correlation coefficient for the 25 March visibilities is a weak 0.408 and for 4 April it is exactly 0.
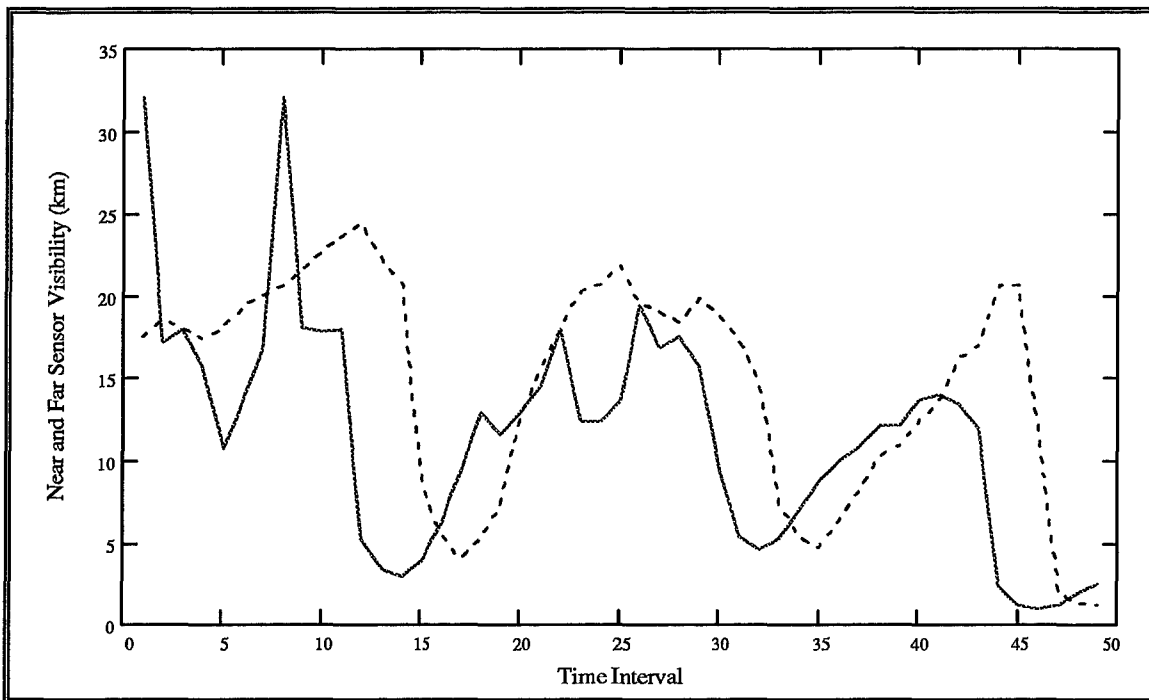

Figure 4.2 Comparison of Near (solid line) and Far (dashed line) Visibility Sensors on 25 March (heavy rain)
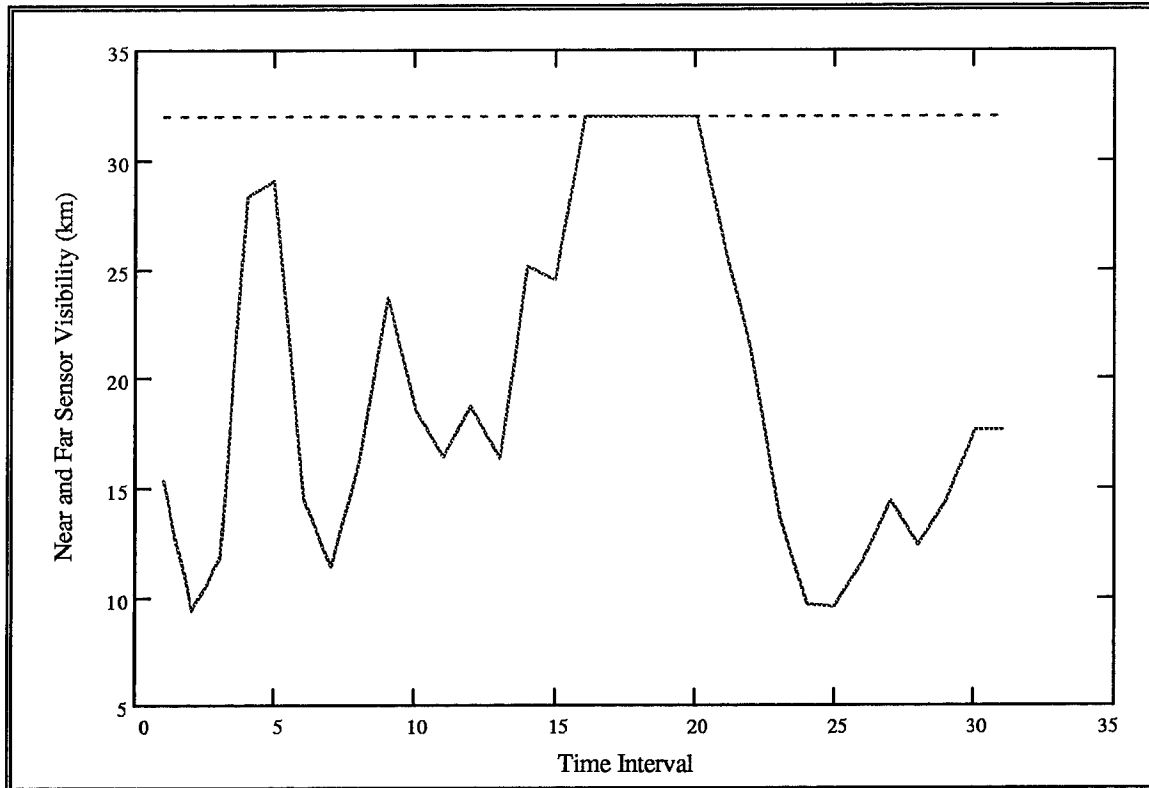
Figure 4.3 Comparison of Near (solid line) and Far (dashed line) Sensors on
4 April (light fog)

These results seem to indicate that the sensors are giving faulty readings. It is

possible that the far visibility sensor was not operating properly. However, an argument

can be made that the readings are accurate. Rain bands are fairly large scale phenomena

occurring on the mesoscale which has a horizontal length on the order of 100 km. Over a

distance of 500 m we should expect a uniform rain rate. However, fog usually occurs on

the smaller storm scale, or even sub-storm scale, meaning it has a horizontal distance on

the order of 1 to 10 km. Here 500 m can be a significant portion of the dimension of the

fog. Thus, it is not unusual to have the kind of variability we see in the sensor readings.

The data from 25 March seems to indicate that the fog is advecting at about 2 m s^{-1} from

the near sensor to the far sensor since the near sensor minima precede the far sensor

minima by about 3 minutes. The 4 April graph indicates that the horizontal extent of the

fog is not great enough to span from the near sensor to the far sensor. Unfortunately, this variability that fog provides only contributes to the complexity of assessing its impact on ladar image degradation.

4.2.2 Suspicion of Data

As shown by the previous works of others in Chapter 2, the droplet size distribution of the weather phenomena in question is an absolute necessity for the proper calculation of laser radiation extinction. The aerosol spectrometer failed to give indications of any sizes of fog droplets whatsoever. Therefore, this research has been greatly hindered by that lack of data. However, we did still have the raindrop size probe which was producing an abundant amount of data.

We set out to show that the raindrop size data was accurate. The first clue that this may not be the case was that some of the data showed the instrument counting nearly 75,000 raindrops over 64 different bin sizes in one minute. If the data were accurate, we could use it to calculate a theoretical rain rate and it would compare favorably to the measured rain rates. To determine the theoretical rain rate, calculate:

$$\sum_{i=1}^{64} (N_i) \frac{4}{3} \pi r_i^3$$

for each minute, where the r_i's are the 64 radius bin sizes, and N_i is the number of drops in that radius bin. This gives the total volume of rain in cubic millimeters per minute Then divide that number by the area over which the drops are counted, 60 cm^2. Multiply that number by 60 to get the rain rate in millimeters per hour. Graphs of the calculated versus measured rain rates for 25 March are given in Figure 4.4 and Figure 4.5 presents those

values for 2 November. The raw data are contained in *Appendix B*. The disparity in the

results is clear.   The theoretical data poorly matches the measured rain rates. Therefore,

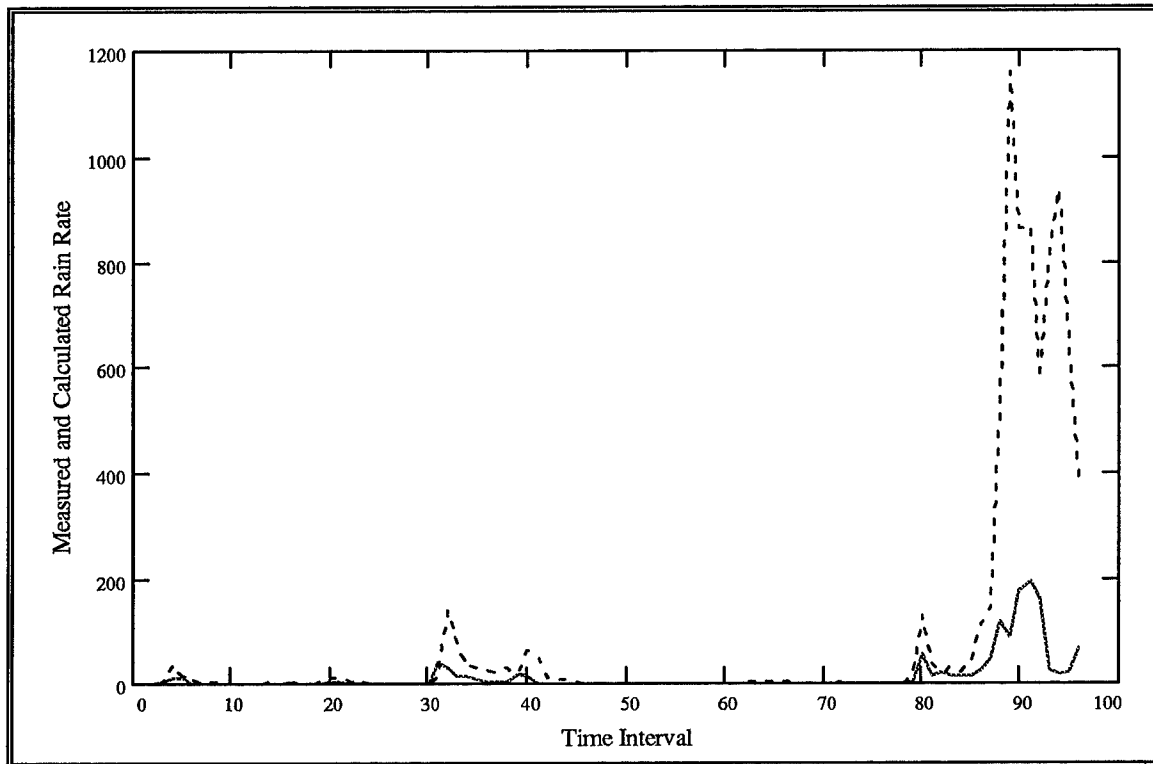the rain drop size distribution data was deemed inaccurate and was not used.

Figure 4.4 Measured (solid) and Calculated (dashed) Rain Rates (mm hr^{-1}) for
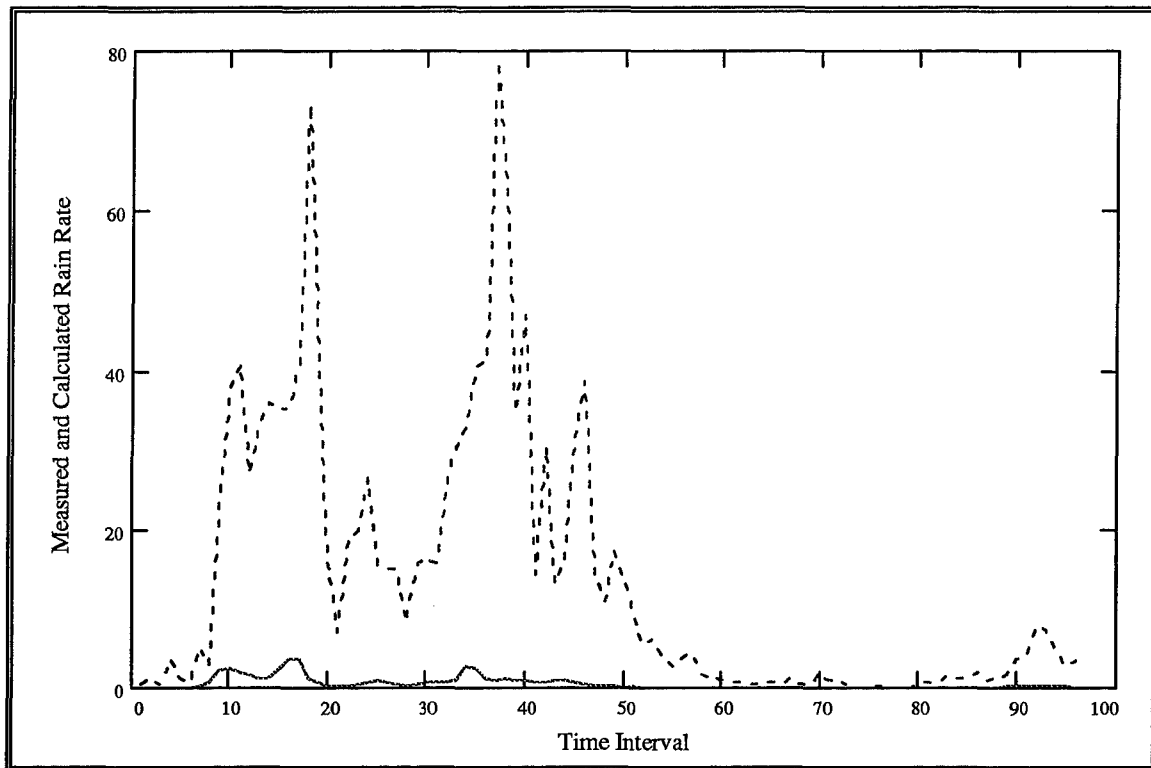25 March (heavy rain)

Figure 4.5 Measured (solid) and Calculated (dashed) Rain Rates (mm hr^{-1}) for 2 November (light rain)

4.2.3 Extinction Calculation

As a second check of the accuracy of the rain drop size data, we decided to calculate the extinction of laser radiation by the rain. The equation for extinction is given by

$$\beta_{ext} = (n^*)\sigma_{ext}$$

where β_{ext} is in units of m^{-1}, n* is the number density per unit volume (m^{-3}), and σ_{ext} is the extinction cross section per drop (in units of m^2). The number density per volume is given by

$$n^* = \sum_{i=1}^{64} \frac{n_i}{(V_i)\,A}$$

where n_i is the number of drops measured per minute for each radius bin, V_i is the fall speed of each drop size, and A is the area on the spectrometer that the drops fall through per minute (60 cm^2). The fall speeds were taken from a table in Rogers and Yau. The extinction cross section is determined by

$$\sigma_{ext} = \sum_{i=1}^{64} (Q_{ext})\pi r_i^2$$

where r_i is the mean radius of each of the 64 bins and Q_{ext} is the extinction efficiency. Since we are well into the geometric optics regime with size parameters approaching 3.5×10^4, we approximated Q_{ext} as 2.

Table 4.4 shows the extinction calculations for part of the data gathered on 25 March. Theoretically, the extinction should be a constant multiple of the visibility in accordance with Koschmeider's formula

$$V = \frac{const}{\beta_{ext}}$$

where V is the visibility and β_{ext} is the extinction for a given wavelength. For this data the theoretical constant varies dramatically, indicating that the droplet size distributions may be inaccurate, or that such a relationship does not exist.

Table 4.2 Total Extinction and Visibility Constants for 25 March

Time	Visibility (km)	Total Extinction per km	Visibility Constant	Time	Visibility (km)	Total Extinction per km	Visibility Constant
9:41	16.7	0.09	1.48	10:07	10.4	0.01	0.11
9:42	14.5	0.07	1.06	10:09	9.7	0.02	0.15
9:43	11.2	0.05	0.60	10:10	9.7	0.01	0.08
9:44	10.5	0.04	0.40	10:11	11.2	0.01	0.07
9:45	9	0.01	0.12	10:12	11.3	0.71	8.06
9:46	8.8	0.03	0.25	10:13	3.1	6.00	18.60
9:47	9.4	0.06	0.55	10:14	1.2	3.15	3.78
9:48	10	0.04	0.36	10:15	1	1.89	1.89
9:49	11.2	0.01	0.06	10:16	1.1	2.64	2.91
9:50	11.5	0.003	0.04	10:17	1.9	1.86	3.53
9:51	12.5	0.01	0.13	10:18	1.8	3.68	6.63
9:52	11.9	0.01	0.15	10:19	1.8	9.81	17.67
9:53	9.7	0.14	1.36	10:20	1.4	12.59	17.62
9:54	7.3	0.37	2.67	10:21	1.1	38.56	42.41
9:55	6.8	0.42	2.84	10:22	0.6	65.18	39.11
9:56	6.9	0.33	2.30	10:23	0.4	59.34	23.74
9:57	12.4	0.41	5.11	10:24	0.3	58.67	17.60
9:58	12.5	0.33	4.07	10:25	0.2	36.49	7.30
9:59	15.5	0.20	3.14	10:26	0.2	55.77	11.15
10:00	11.6	0.13	1.46	10:27	0.2	53.77	10.75
10:01	12.7	0.06	0.79	10:28	0.2	59.42	11.88
10:02	26.8	0.06	1.69	10:29	0.3	50.24	15.07
10:03	22.9	0.068	1.54	10:30	0.4	28.89	11.55
10:04	24.8	0.09	2.20	10:31	0.6	8.94	5.36
10:05	12	0.08	0.94	10:32	0.8	3.53	2.83
10:06	10.4	0.07	0.72	10:33	0.9	3.13	2.81

4.3 Correlation Coefficients

Correlation coefficients were computed for every possible combination of weather variable and degradation parameter on each of the 8 days of data collection. Table 4.5 presents the correlation coefficients of dropout percentage and rain rate for each of the targets viewed. Table 4.6 gives the coefficients for each target of dropout percentage and visibility. Table 4.7 shows the correlation coefficients for false return percentage and visibility in the left column with false return percentage and rain rate in the right. Targets

which were not on the range or outside of the field of view on that day are listed as

"N/A". In Table 4.7, days with no rain are also listed as "N/A".

Table 4.3 Correlation Coefficients of Target Dropout Percentage With Rain Rate For Each Target

Date	Building	Tank	Panels
25 March	.91	.67	N/A
2 November	N/A	.31	.32
18 December	N/A	.54	.15

Table 4.4 Correlation Coefficients of Target Dropout Percentage With Visibility For Each Target

Date	Building	Tank	Panels
15 March	-.66	N/A	N/A
25 March	-.58	-.57	N/A
29 March	-.42	-.14	N/A
4 April	.02	-.19	N/A
30 October	N/A	-.41	-.36
2 November	N/A	-.51	-.41
6 December	.18	.28	.45
18 December	N/A	-.29	.02

Table 4.5 Correlation Coefficients of False Return Percentage with Visibility and Rain Rate

Date	False Return Percentage and Visibility	False Return Percentage and Rain Rate
15 March	-.38	N/A
25 March	-.49	.90
29 March	-.12	N/A
4 April	.43	N/A
30 October	.20	N/A
2 November	-.37	.33
6 December	.08	N/A
18 December	-.22	.32

Several of these results are worth noting. The day with the most intensive weather and the largest sample of images, 25 March, shows excellent linear correlation between both dropout percentage and false return percentage and rain rate. Having been computed from 70 or more data pairs, these coefficients are statistically significant. By contrast, the rain rate correlations for the other two rain days, 2 November and 18 December, are not nearly as high. The most likely reason is that the rain rates for these two days are very light, less than 5 mm hr^{-1}. The possibility arises that ladar system noise is masking the true response.

The correlations of image degradation with visibility do not appear as strong as those with rain rate. The maximum visibility correlation of 0.66 occurs on 15 March, the day with the thickest fog, and the rest are somewhat lower. Again, this indicates that the linearity of the relationship is weak, not the relationship itself. A graphical analysis should give a better understanding of how reductions in visibility affect image degradation. We have shown that cloud droplet sizes are significant scatterers of near infrared radiation, thus a viable relationship exists. Intuitively, the dropouts and false returns should increase as visibility decreases, and increase as rain rate increases. The coefficients for 6 December in Table 4.6 indicate that the percentage of target dropouts increases as visibility increases. Clearly, these coefficients are suspect and should not be trusted as indicators of the true correlation between dropouts and visibility.

4.4 Graphical Analysis of Image Degradation as a Function of Weather Parameter

In presenting graphical analysis of image degradation as a function of weather, it becomes extremely useful to understand what percentage of the target area is degraded as the weather varies. Target recognition software becomes unreliable when a certain percentage of the target cannot be detected. The following four sections depict of the percentage of dropouts and false returns plotted against visibility and rain rate. Here the nature of the relationships becomes clear. For a different view of the data, time series graphs were produced for each day as well. Actual numbers of dropouts and false returns were plotted with the weather parameters over time. These graphs, located in *Appendix C*, do not show the nature of the relationships as well.

The analyses are presented in descending order of weather severity by the following categories: dropouts vs. visibility, dropouts vs. rain rate, false returns vs. visibility, false returns vs. rain rate. All percentages are expressed out of 100. Several of the plots appear to conform to the shape of distinct functions. Those that do are fitted with a linear or exponential equation in order to get a quantitative understanding of the relationship. The linear equations are a best-fit solution, while the exponential functions were estimated. Again, without accurate droplet size distributions, a more scientific approach to equation fitting is not feasible.

4.4.1 Analysis of Dropout Percentage vs. Visibility

Figure 4.6 shows how the percentage of dropouts increased as visibility decreased on March 15th. The graph resembles an exponential shape, with the percentage of dropouts increasing dramatically as the visibility falls below 2 km. It is fitted with the

curve $y=120exp(-.5x)$. Figure 4.7 shows a well-defined exponential shape. The

percentage of dropouts increases sharply and fairly consistently as the visibility falls below

2 km, save for one apparent outlier at 11.3 km. However, the raw data indicate that this

outlying point is a reflection of the lag time between increases in rain rate and decreases in

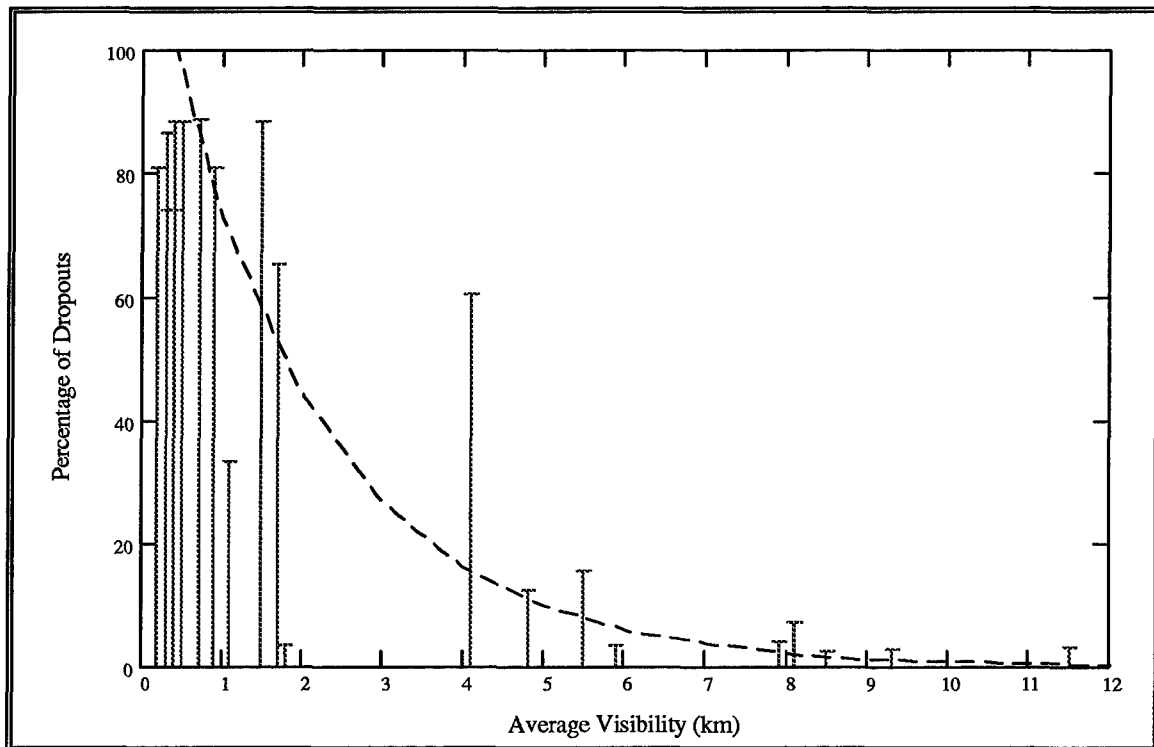visibility. This graph is fitted with the equation $y=80exp(-1.3x)$ which seems to fit the

curve shape well.

Figure 4.6 Dropout Percentage of the Building Target vs. Visibility on
15 March (thick fog)
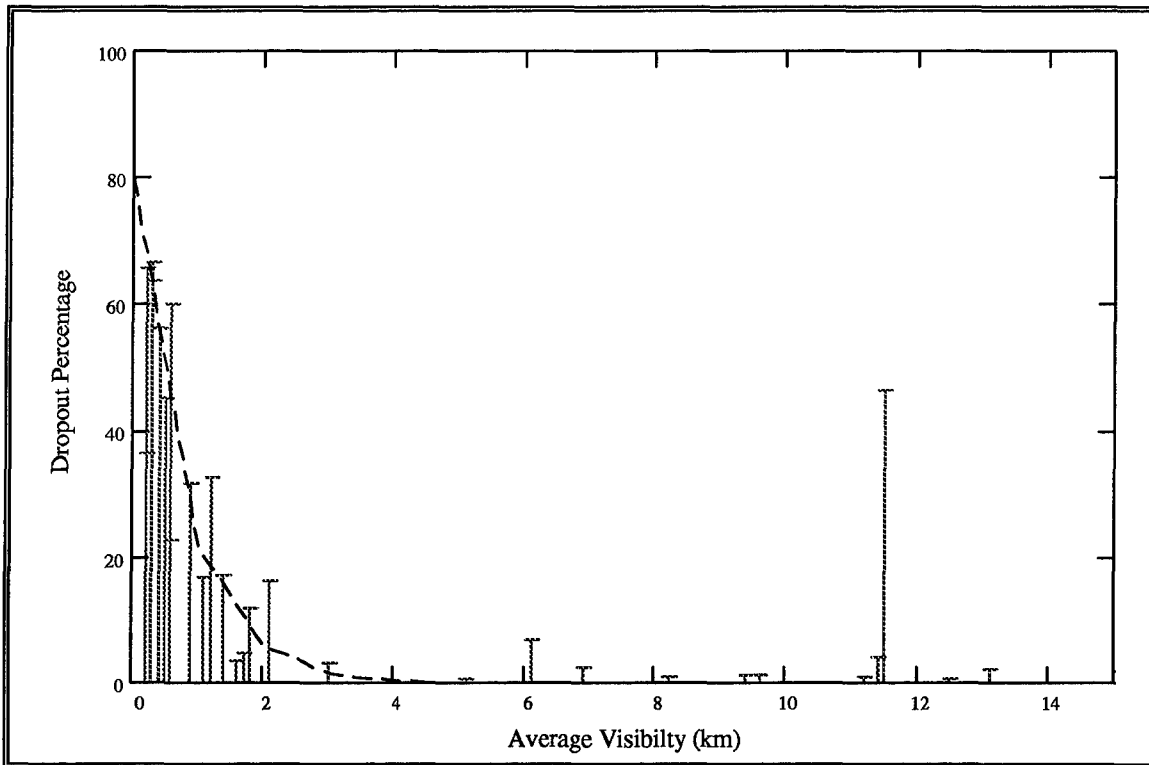
Figure 4.7 Dropout Percentage of the Building vs. Visibility for 25 March (heavy rain)
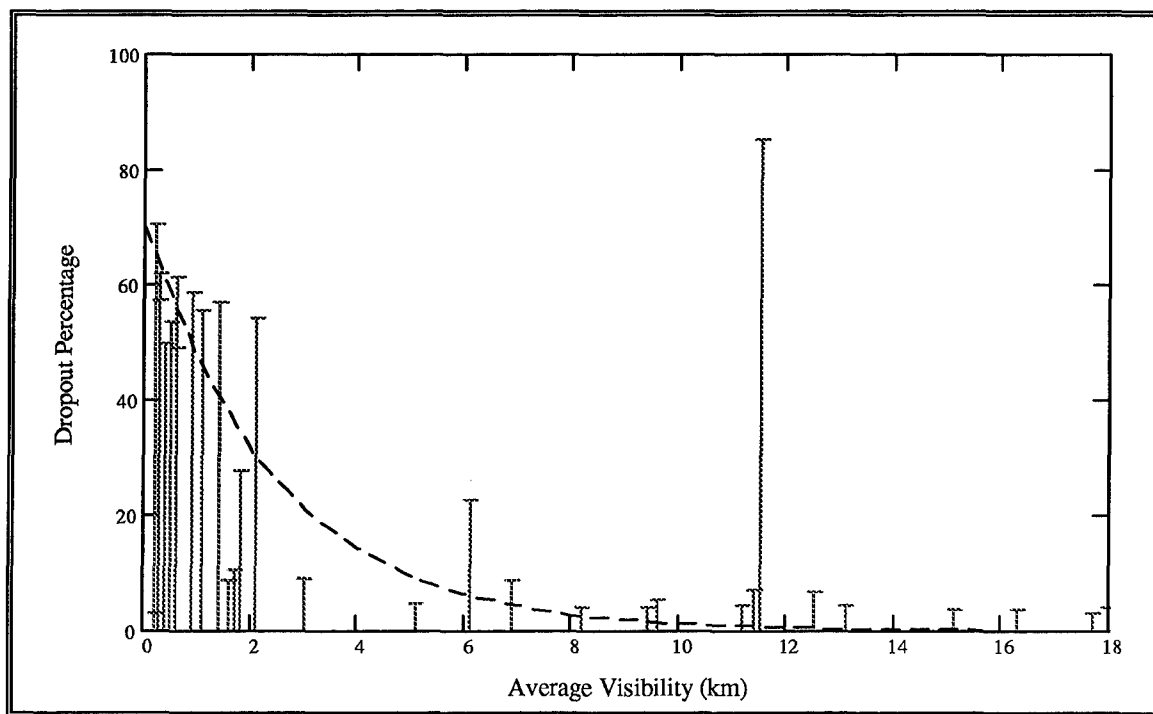
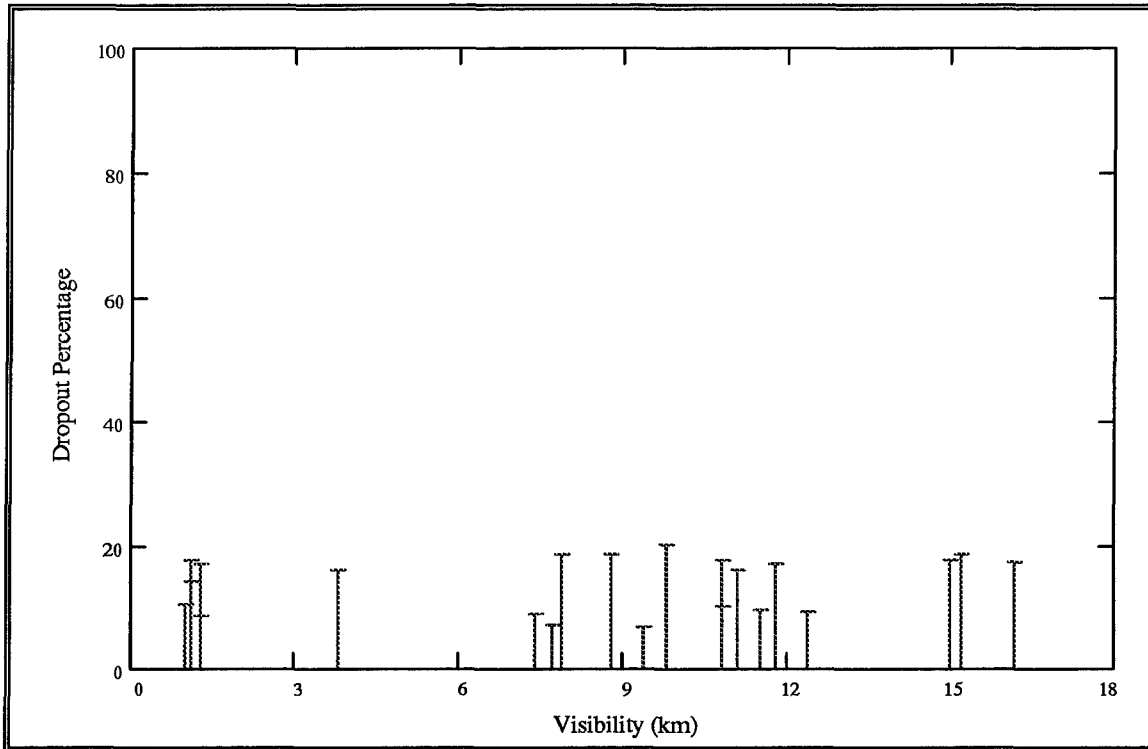Figure 4.8 Dropout Percentage of the Tank vs. Visibility for 25 March (heavy rain)

Comparison of Figure 4.8 to Figure 4.7 shows a noticeable disparity in the shape

of the graphs. Figure 4.7 has a better exponential shape than Figure 4.8, which is fitted

with $y=70exp(-.4x)$. with slightly higher dropout percentages for the tank as visibility falls

below 2 km. Figure 4.9 shows a sharp increase in dropouts as the visibility decreases past

1 km. However, the percentages then decrease again as the visibility reaches a minimum

of 0.2 km, which is not what we would expect. Since only one visibility sensor was

functioning, a likely explanation for the decrease is that the visibility reading is not

representative of the fog between the ladar and the target. Figure 4.10 has smaller dropout

percentages than Figure 4.9, but still shows the decrease in dropouts percentage as

visibility falls below 1 km.
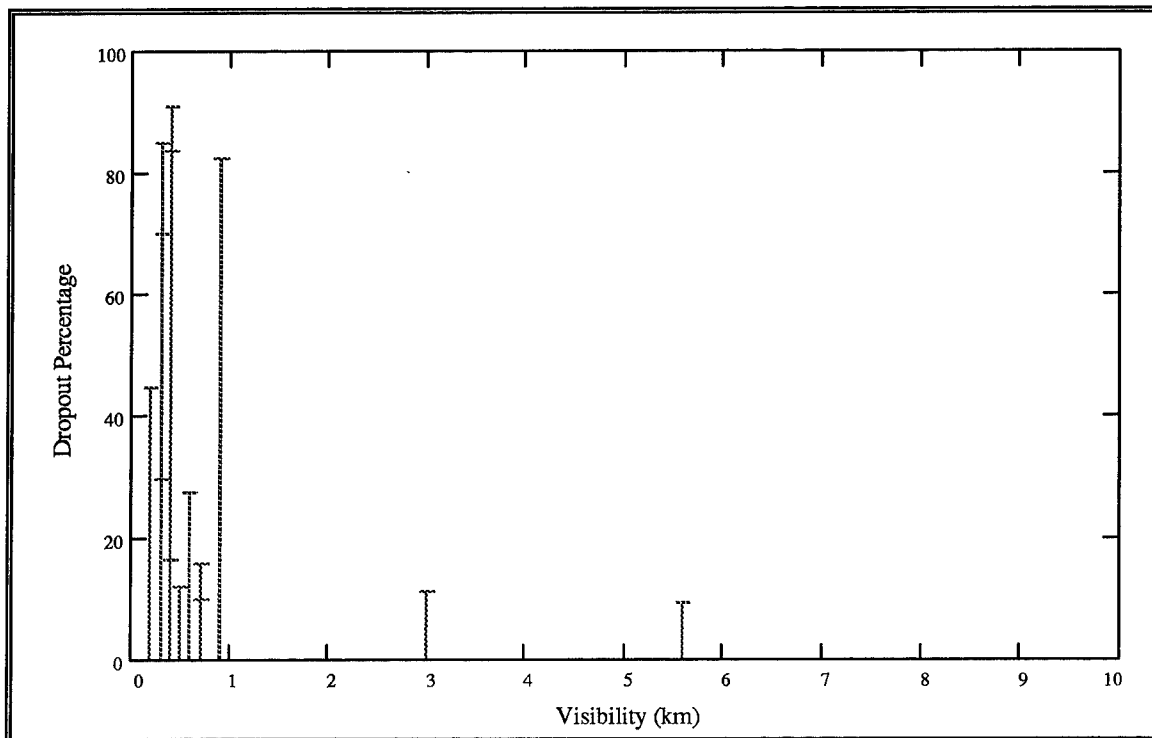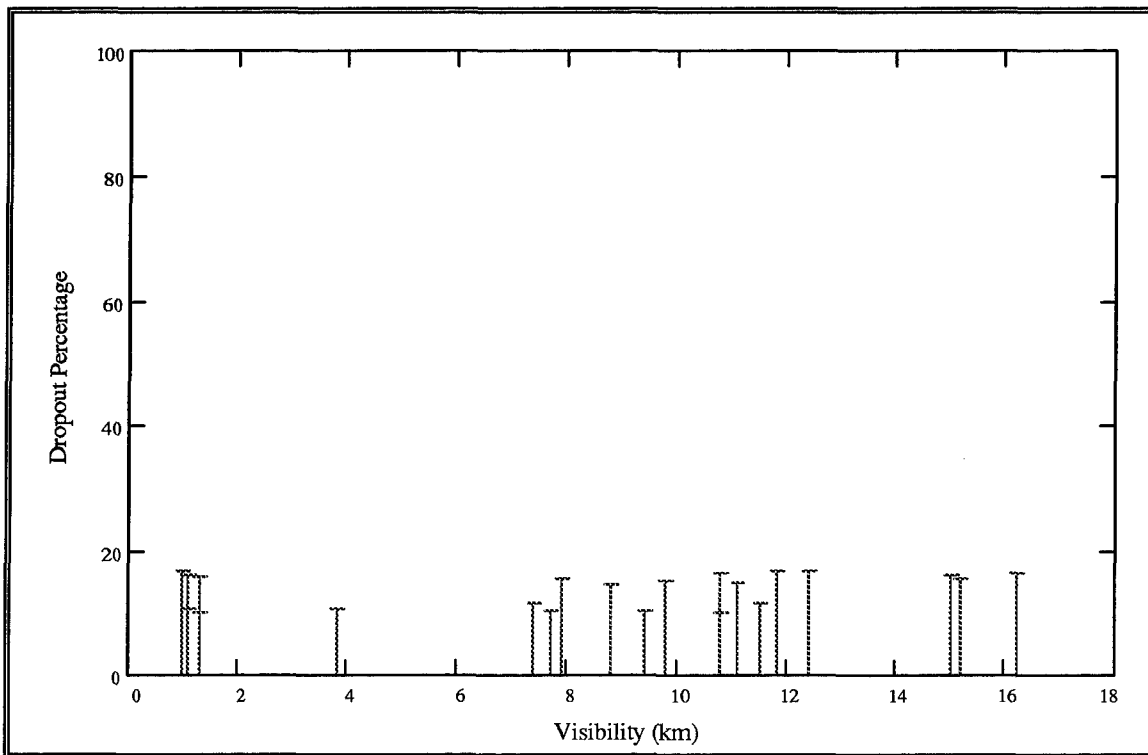

Figure 4.9 Dropout Percentage of the Tank vs. Visibility for 30 October (moderate fog)
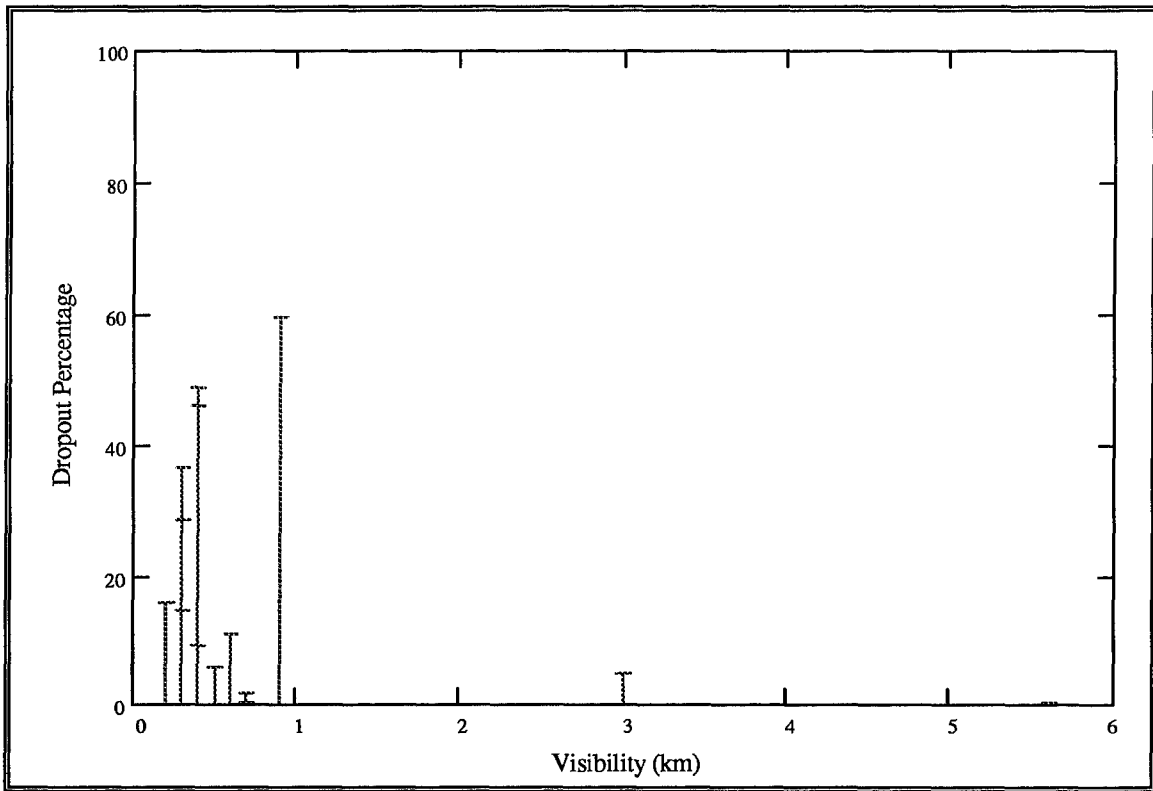
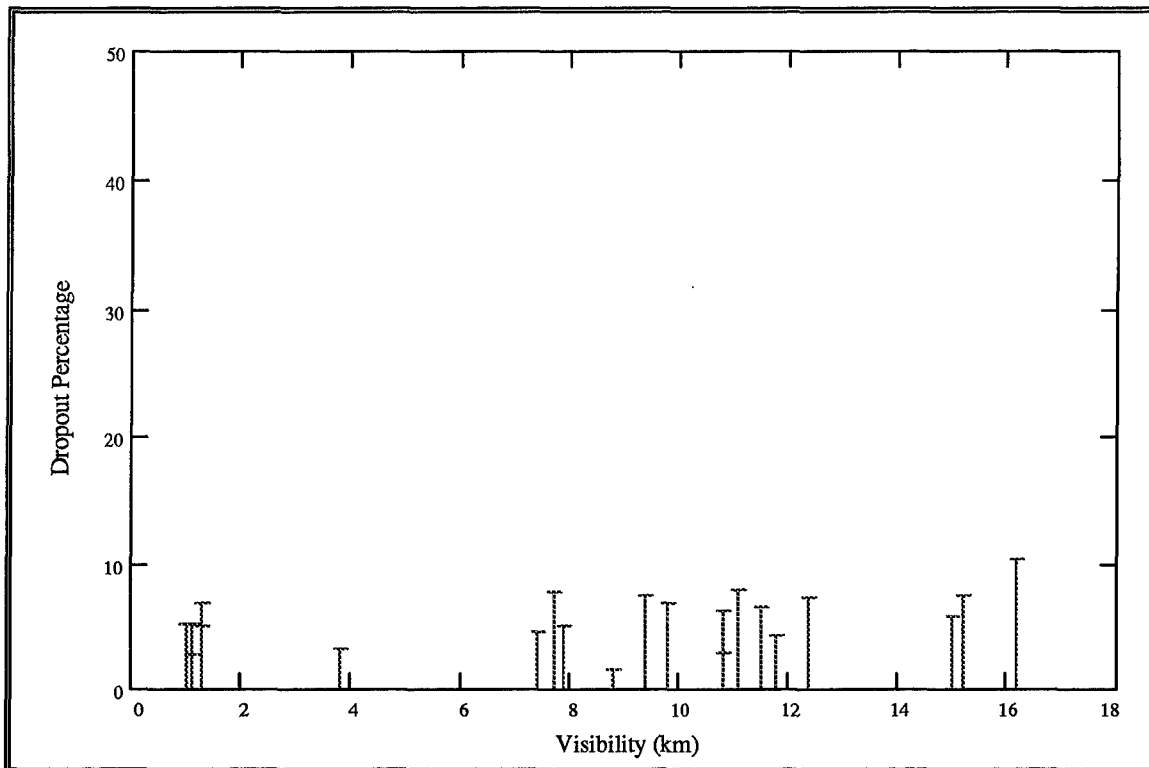Figure 4.10 Dropout Percentage of the Panel vs. Visibility for 30 October (moderate fog)

The next three figures, 4.11, 4.12, and 4.13 depict the dropout percentages on

6 December for the building, tank, and panel respectively. Although the weather could be

classified as moderate fog (with visibility dropping to 1.1 km), there is no discernible

pattern to the graphs. Dropout percentages of the tank and building are near 20% or

below, with the panel having maximum percentages of roughly 10%. All three seem to

have no dependence on visibility.

Figure 4.11 Dropout Percentage of the Building vs. Visibility for
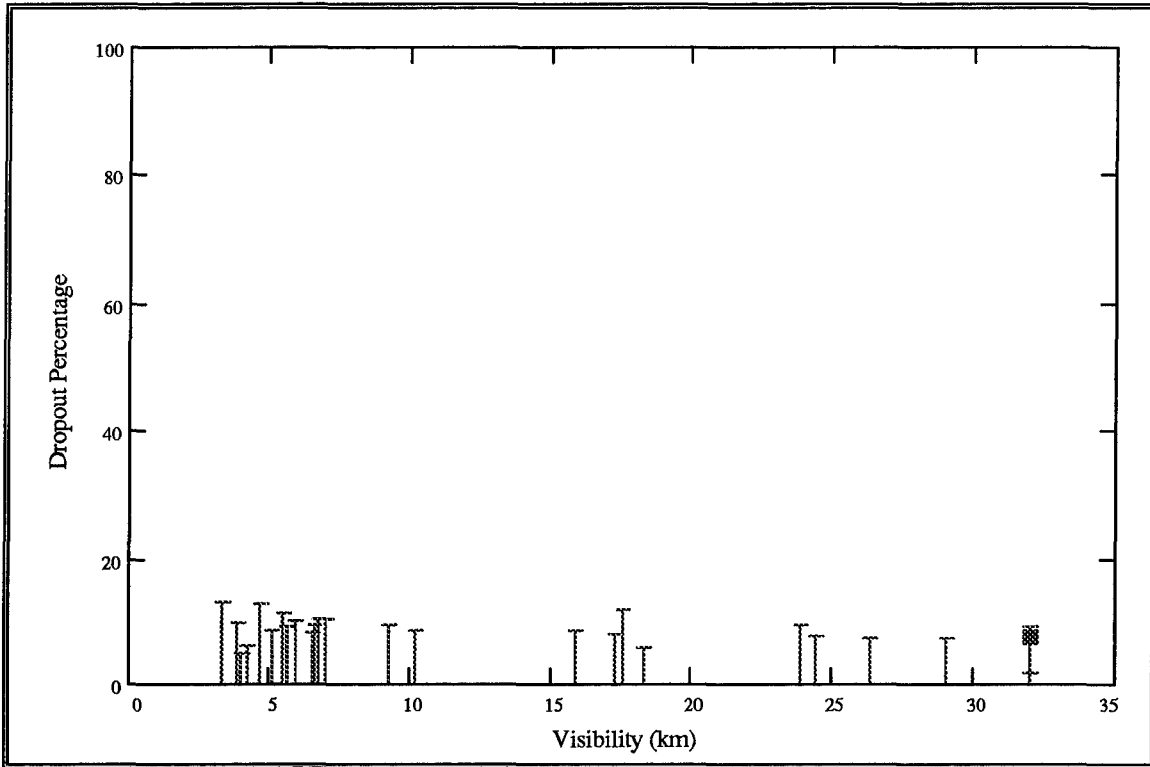6 December (moderate fog)

Figure 4.12 Dropout Percentage of the Tank vs. Visibility for 6 December (moderate fog)

48

Figure 4.13 Dropout Percentage of the Panel vs. Visibility for
6 December (moderate fog)

Similar to the graphs of 6 December, the percentages for the tank and panel targets

on 2 November appear to have no dependence on visibility as shown in Figures 4.14 and

4.15. Dropouts remain below 15% for the tank and below 7% for the panel, with neither

increasing or decreasing along the visibility axis.

Figure 4.16 indicates some dependence of dropout percentage on visibility. As the

visibility drops below 6 km, the tank dropout percentage shows an "exponential-like"

increase.   However, it is not nearly as clear as that of 15 March or 25 March. Figure 4.17

has no distinct shape and appears noisy.

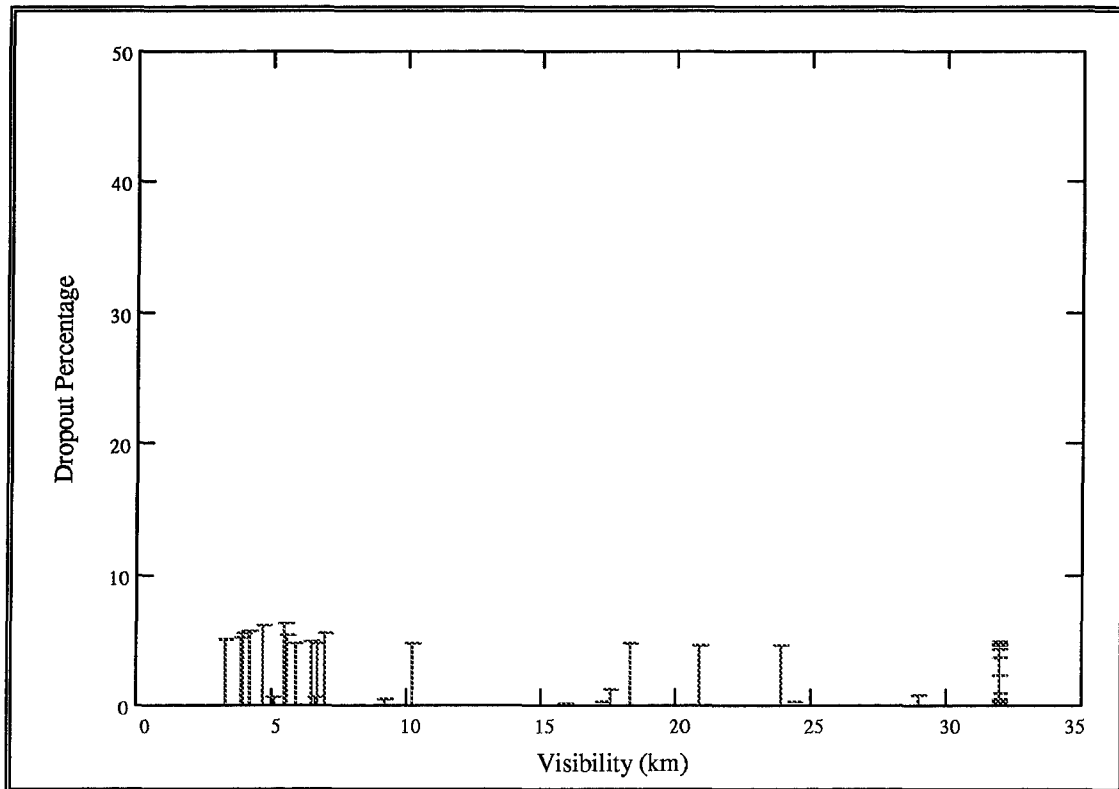Figure 4.14 Dropout Percentage of the Tank vs. Visibility for 2 November (light rain)

Figure 4.15 Dropout Percentage of the Panel vs. Visibility for 2 November (light rain)
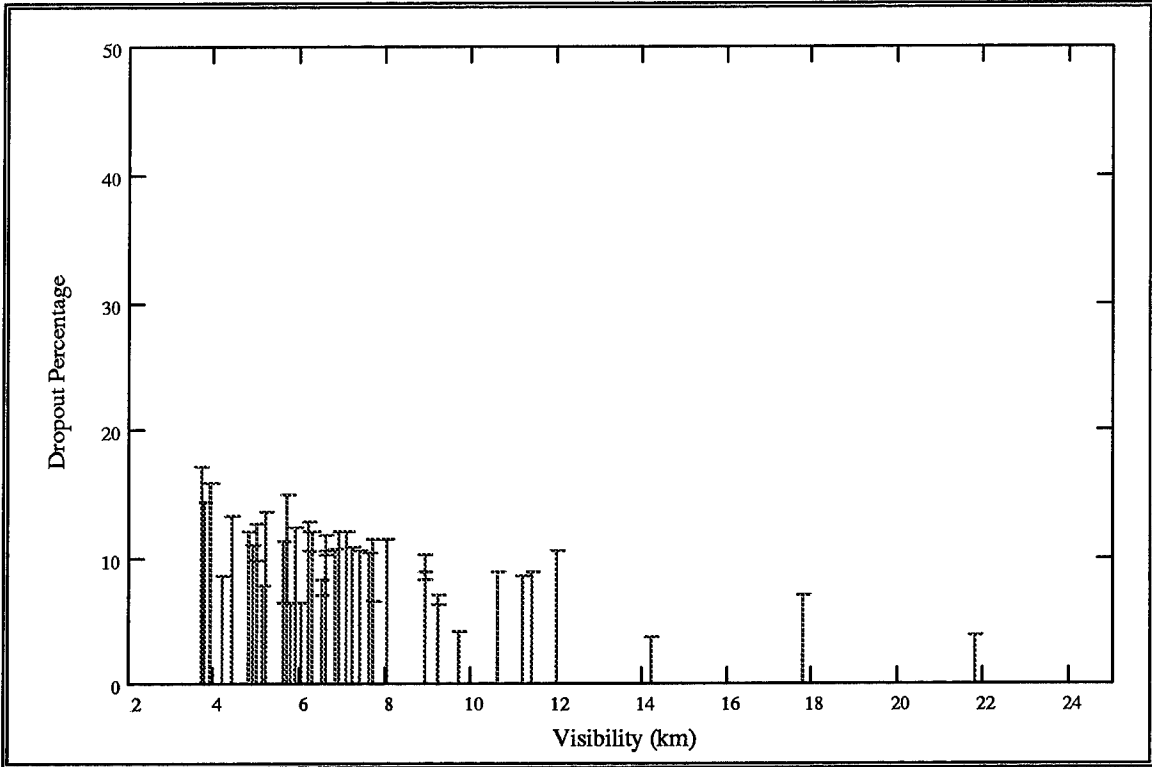
50

Figure 4.16 Dropout Percentage of the Tank vs. Visibility for 18 December (light rain)
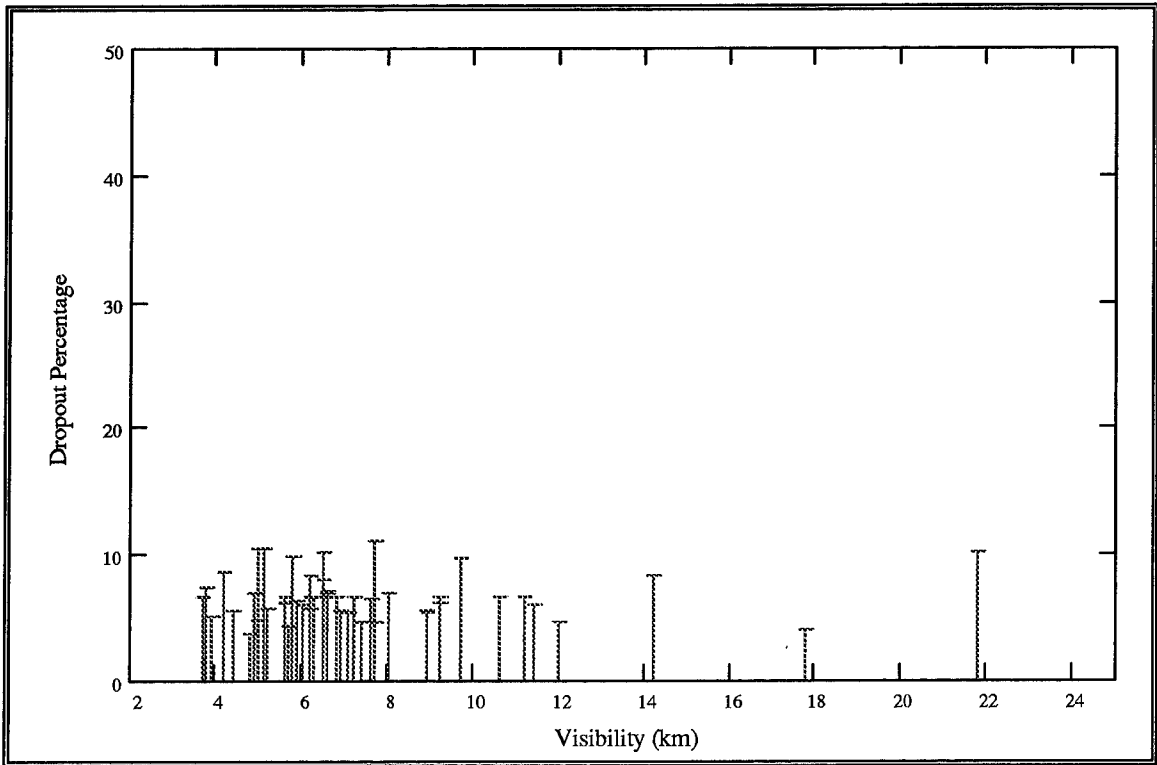

Figure 4.17 Dropout Percentage of the Panel Target vs. Visibility on
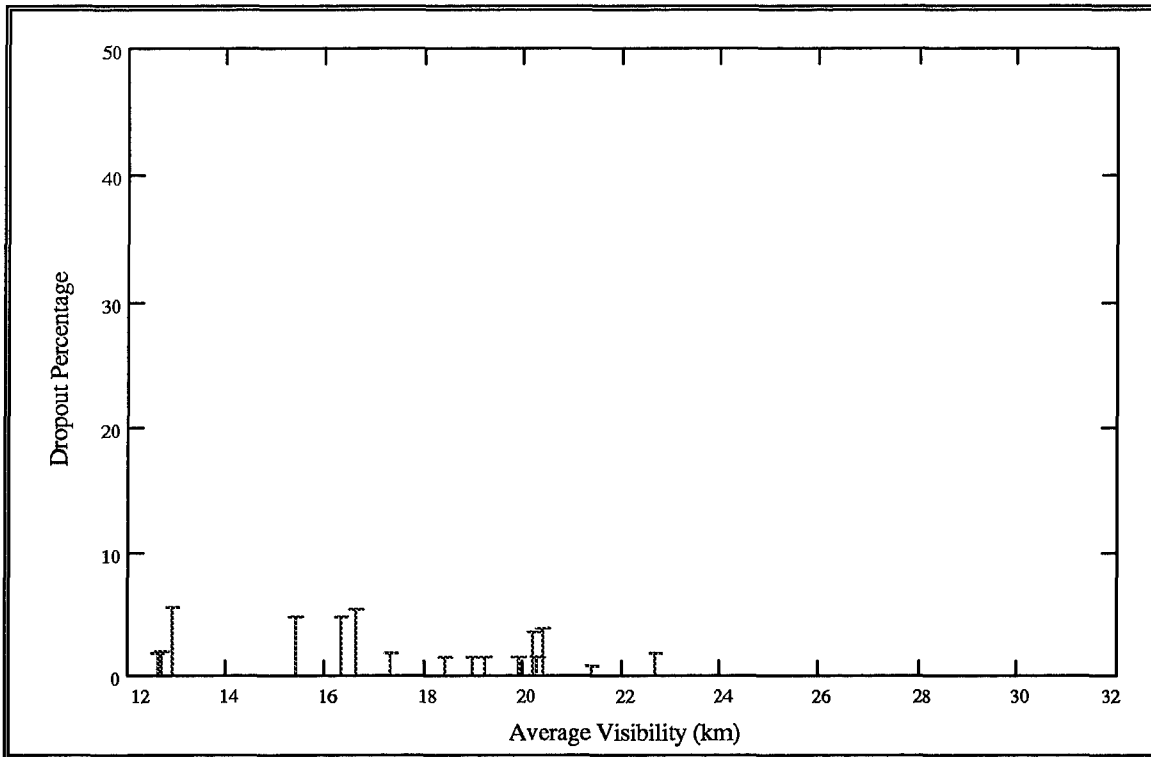18 December (light rain)

51

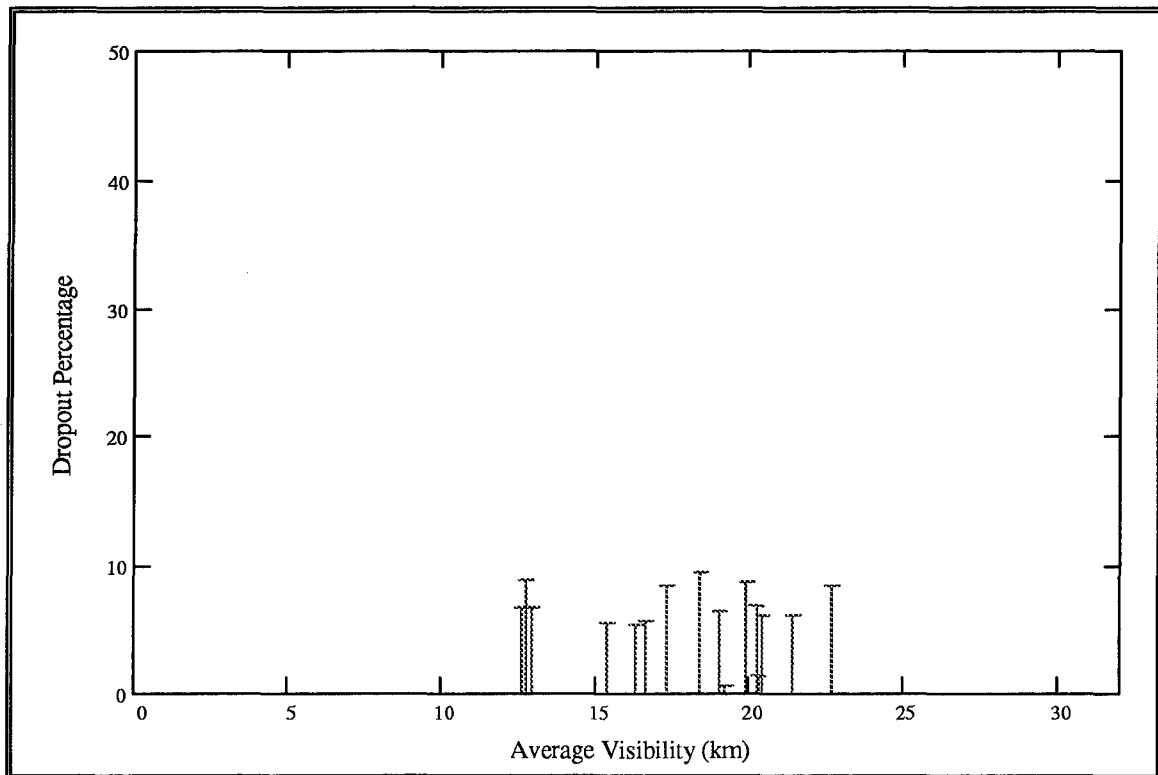Figure 4.18 Dropout Percentage of the Building vs. Visibility for 29 March (light fog)

Figure 4.19 Dropout Percentage of the Tank vs. Visibility for 29 March (light fog)
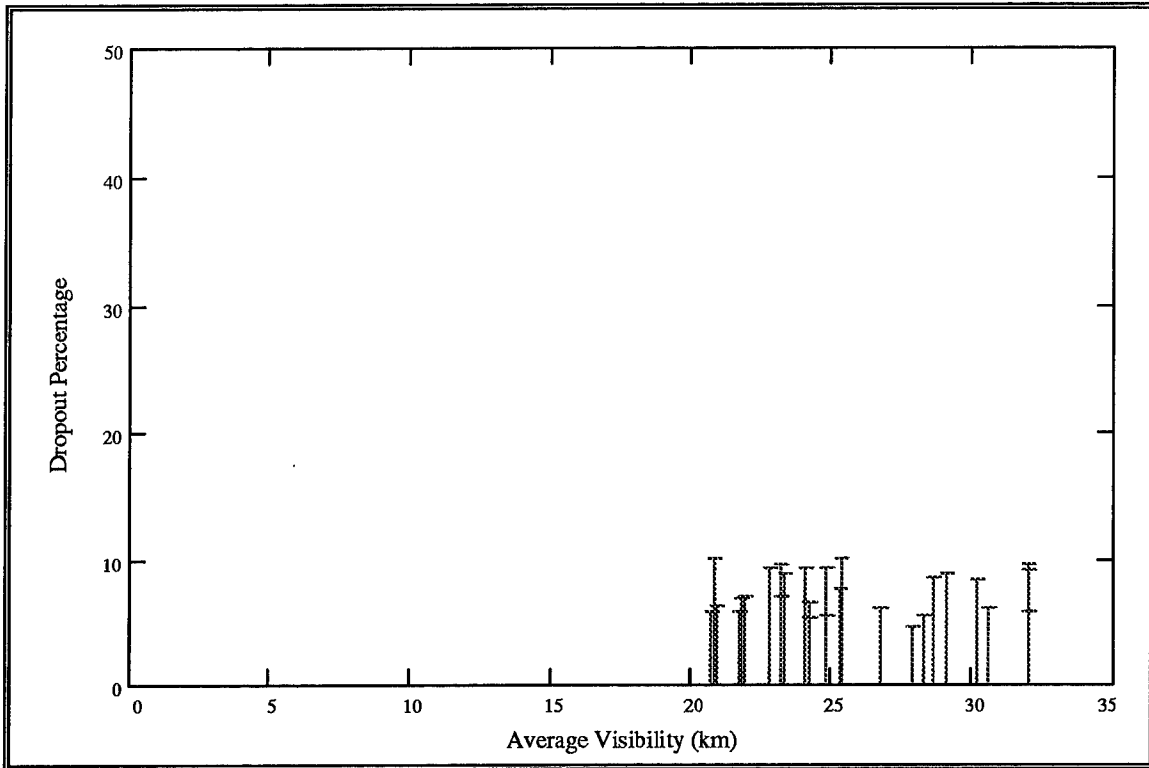
Figure 4.20 Dropout Percentage of the Building vs. Visibility for 4 April (light fog)
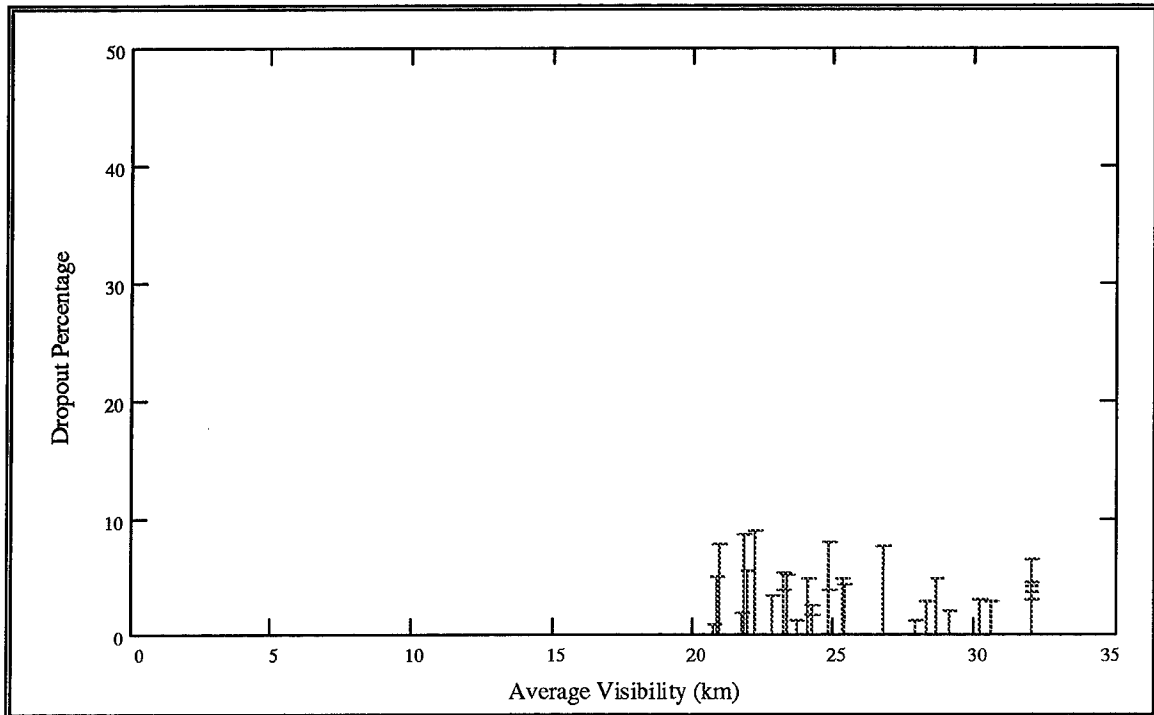

Figure 4.21 Dropout Percentage of the Tank vs. Visibility for 4 April (light fog)

Figures 4.18 through 4.21 show the percentage of target dropouts remaining below 10% as the visibility varies. System noise dominates these graphs.

4.4.2 Target Dropout Percentage vs. Rain Rate

As evidenced by a correlation coefficient of 0.91, dropout percentages on 25 March indicate good linear correlation with rain rate in Figure 4.22. The computed best-fit line is also shown. Its equation is given by $y=.46x + 2.74$. Figure 4.23, for the tank on the same day, is fitted with the similarly-sloped equation $y=.43x + 12.1$. The correlation coefficient for this data was a respectable 0.67. Figure 4.24, dropout percentage for the tank on 18 December, shows the linearity that its correlation coefficient of 0.54 would dictate. The data points are fairly symmetrical and "tight" around the best fit line of $y=1.559x + 8.417$. The equation fitted to Figure 4.25 is $y=.303x + 6.323$. The fact that it is nearly horizontal indicates that the dropouts are nearly independent of rain rate for the panel target on 18 December. The correlation coefficient of 0.15 supports this finding.
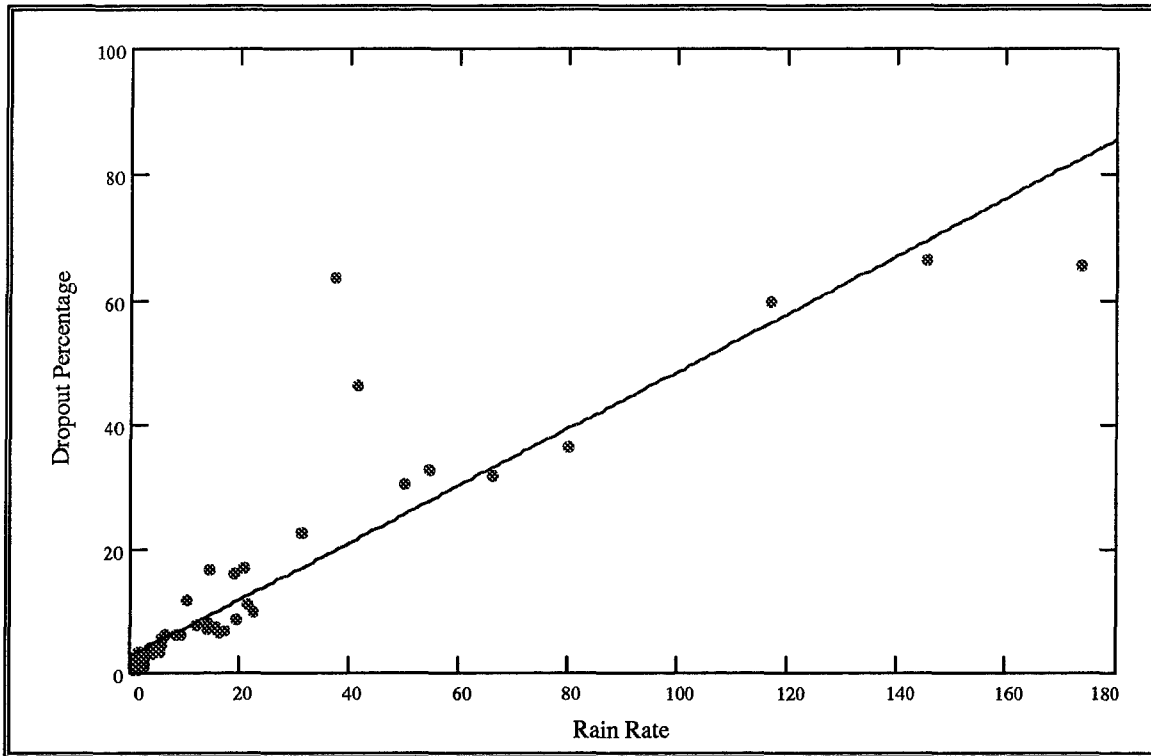
Figure 4.22 Dropout Percentage of the Building vs. Rain Rate (mm hr^{-1}) on
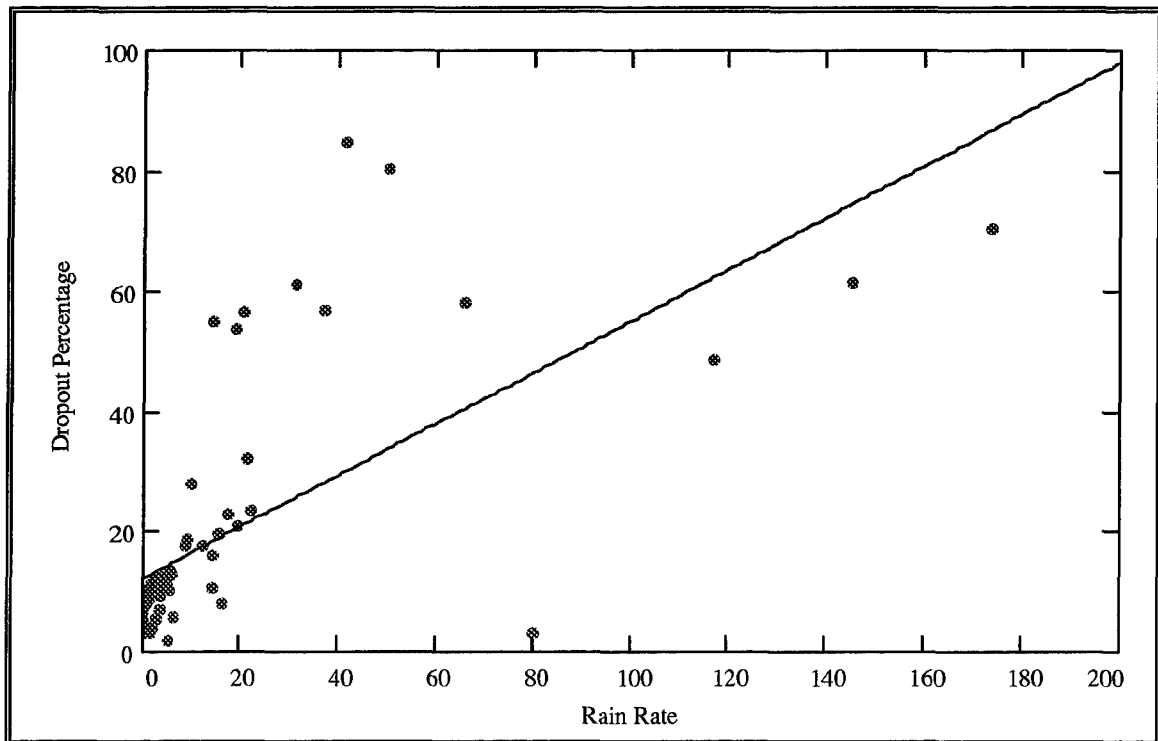25 March (heavy rain)

Figure 4.23 Dropout Percentage of the Tank vs. Rain Rate (mm hr^{-1}) on
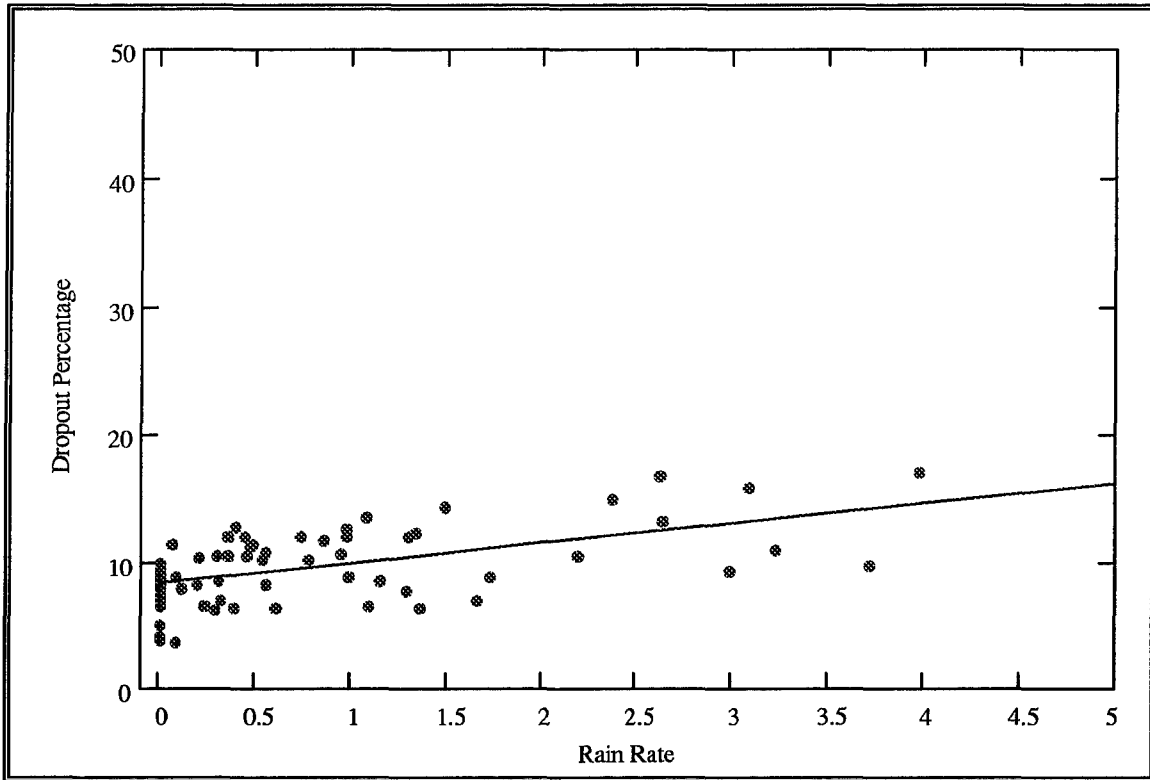25 March (heavy rain)

Figure 4.24 Dropout Percentage of the Tank vs. Rain Rate (mm hr^{-1}) on
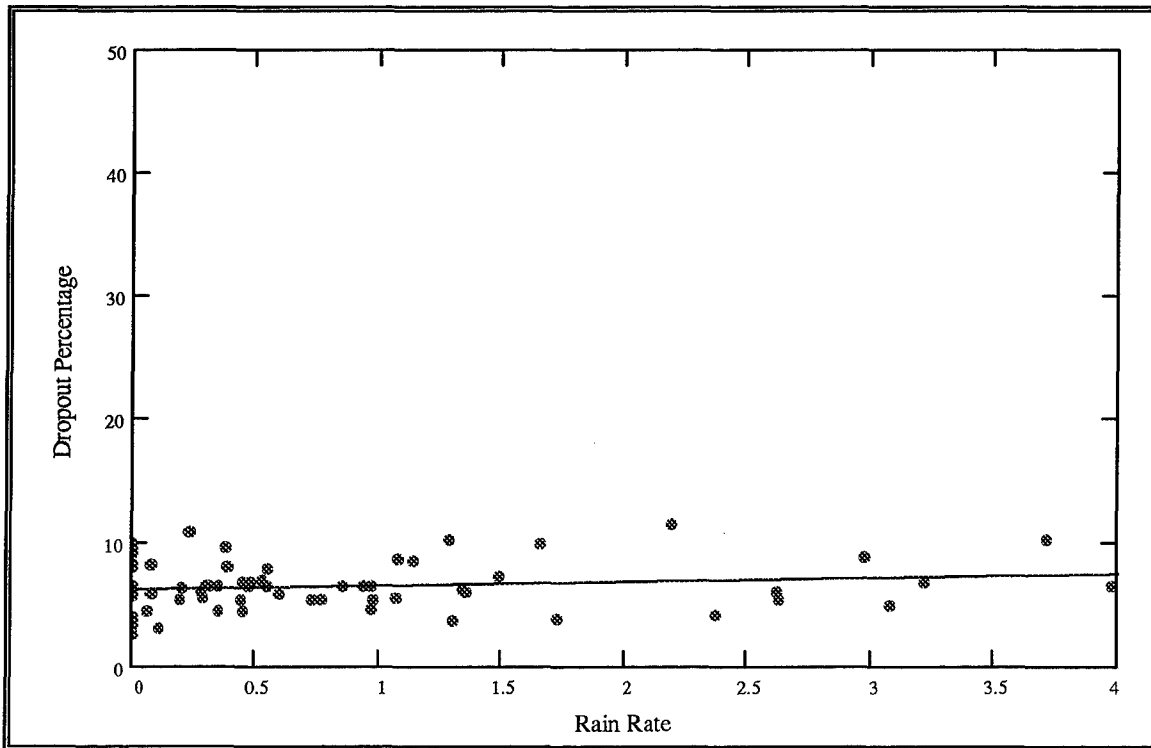18 December (light rain)

Figure 4.25 Dropout Percentage of the Panel vs. Rain Rate (mm hr^{-1}) on
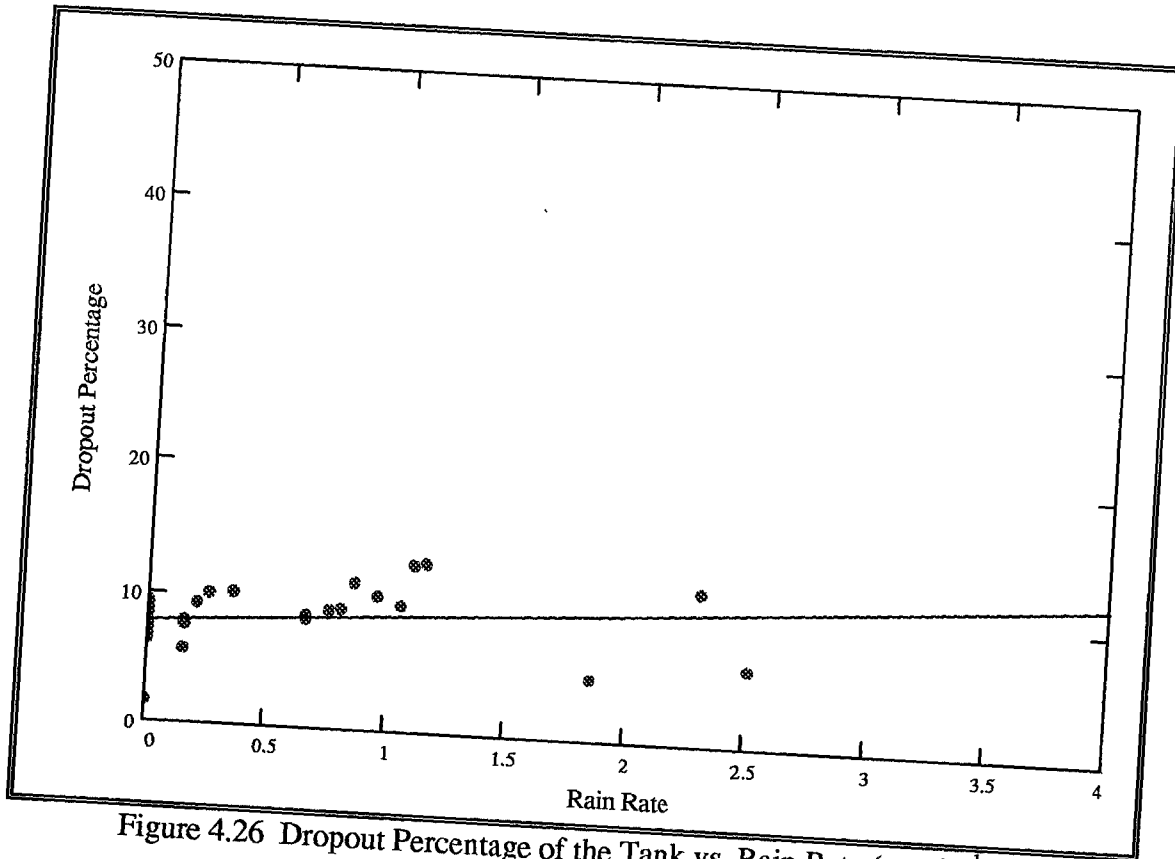18 December (light rain)

Figure 4.26 Dropout Percentage of the Tank vs. Rain Rate (mm hr^{-1}) on
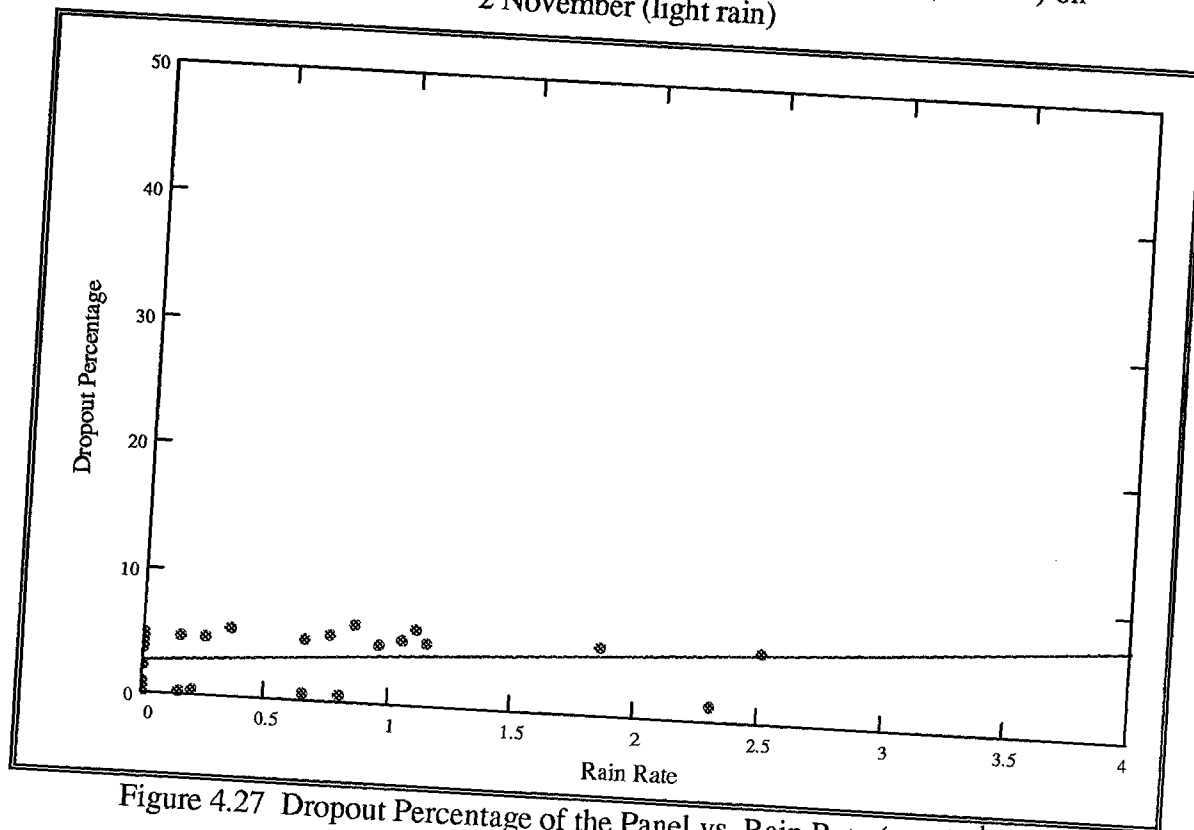2 November (light rain)

Figure 4.27 Dropout Percentage of the Panel vs. Rain Rate (mm hr^{-1}) on
2 November (light rain)

The best-fit lines computed for Figures 4.26 and 4.27 are $y=.998x + 7.824$ and $y=1.126x + 2.639$, respectively. The data points do not fit as tightly around the line as on some of the other graphs, which is supported by their correlation coefficients of 0.31 and 0.32. However, 2 November had the lightest of the rain rates, which may attribute to the poorer fit. Note that the dropout percentages for the tank are somewhat higher than those for the panel, indicating that the shape of the target affects dropout percentage.

4.4.3 False Return Percentage vs. Visibility

Figures 4.28 and 4.29 show the best response of false returns to visibility. They generally have an exponential shape, and as such are fitted with exponential functions. The curve to the 15 March data is $y=90exp(-2x)$. The data from 25 March is fitted with $y=50exp(-1.2x)$.
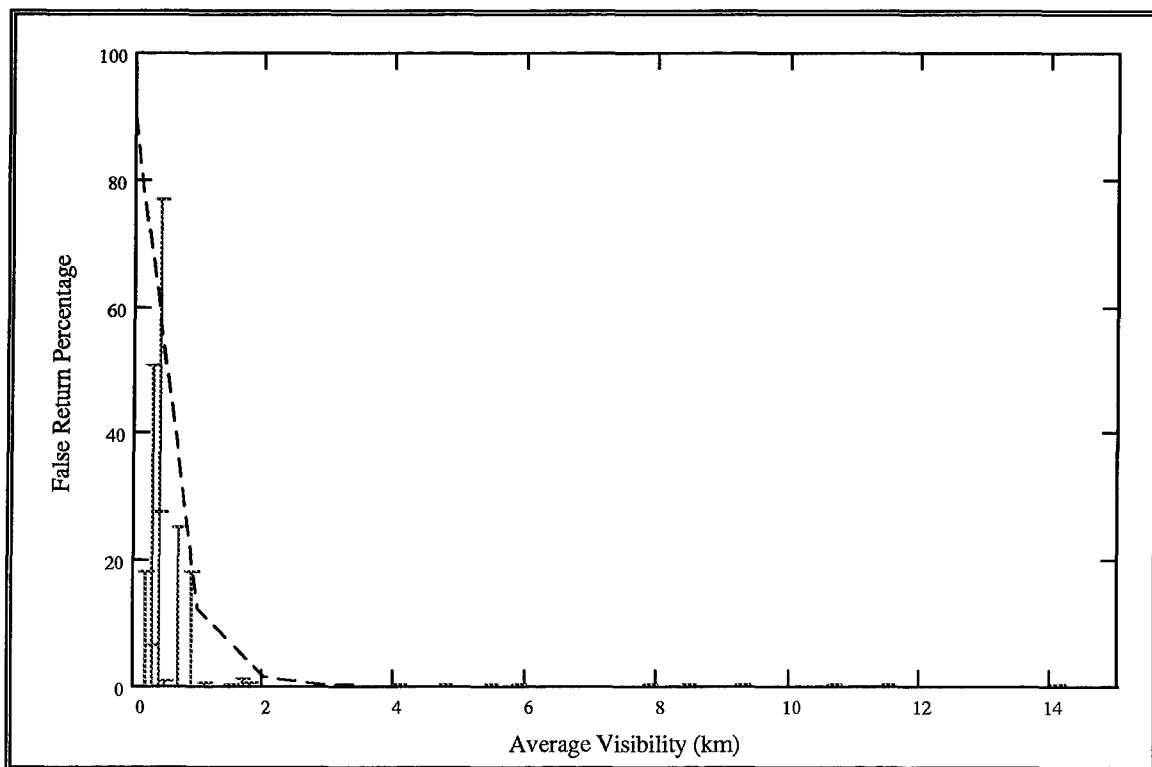
Figure 4.28 False Return Percentage vs. Average Visibility on 15 March (thick fog)
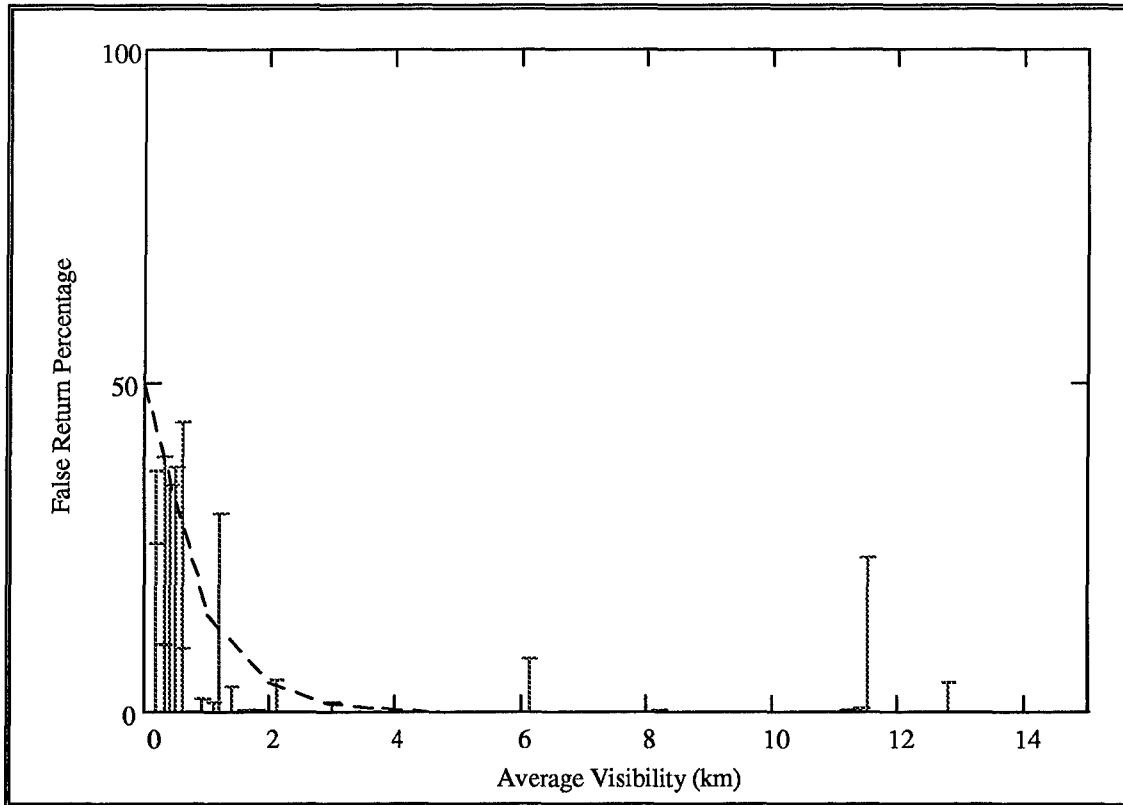
Figure 4.29 False Return Percentage vs. Average Visibility on 25 March (heavy rain)
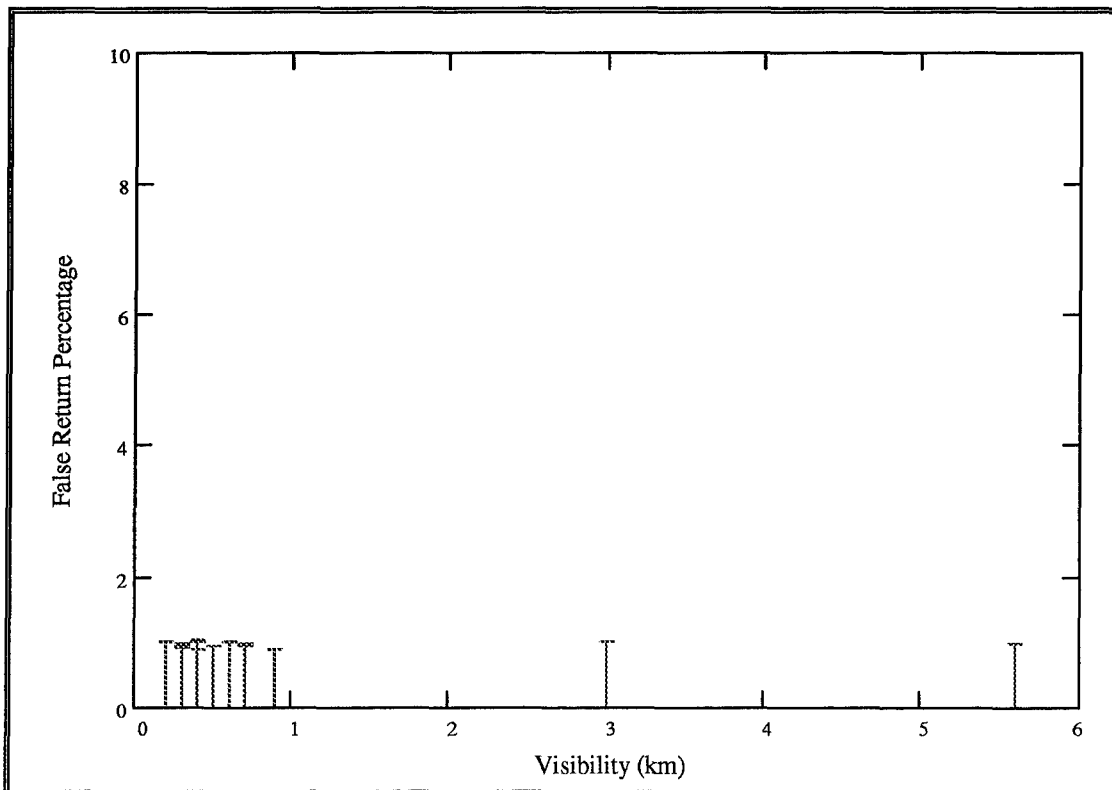
Figure 4.30 False Return Percentage vs. Visibility on 30 October (moderate fog)
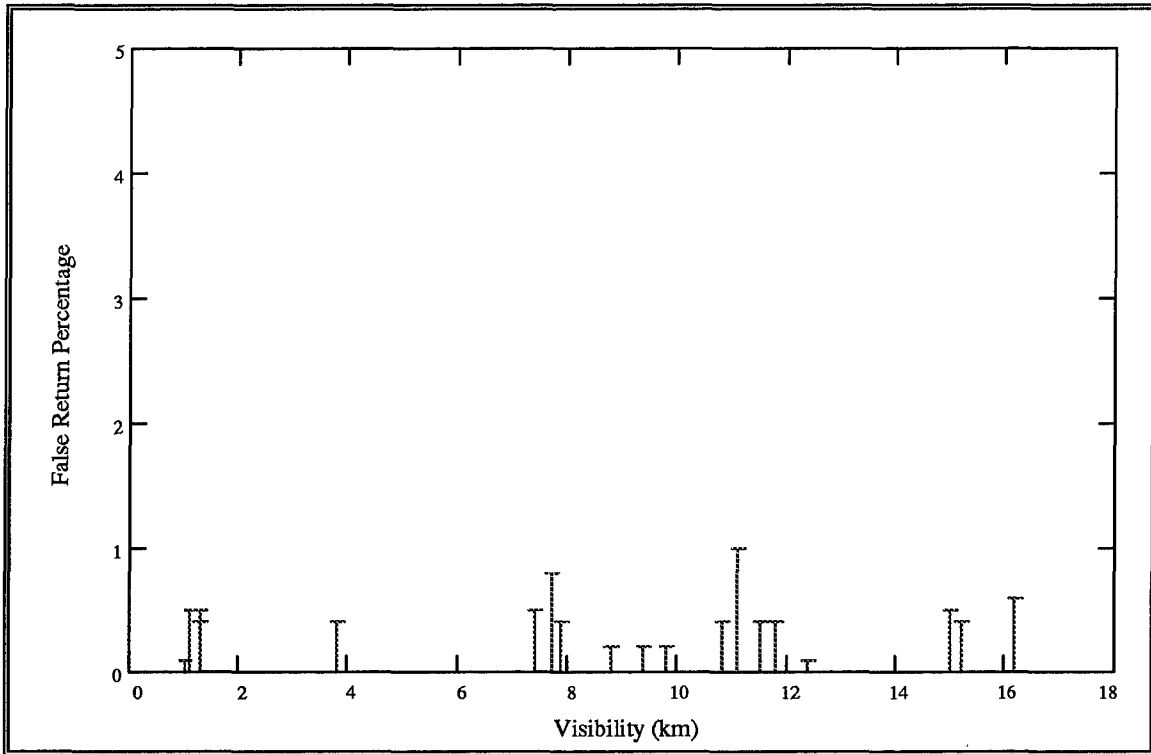
Figure 4.31 False Return Percentage vs. Visibility on 6 December (moderate fog)
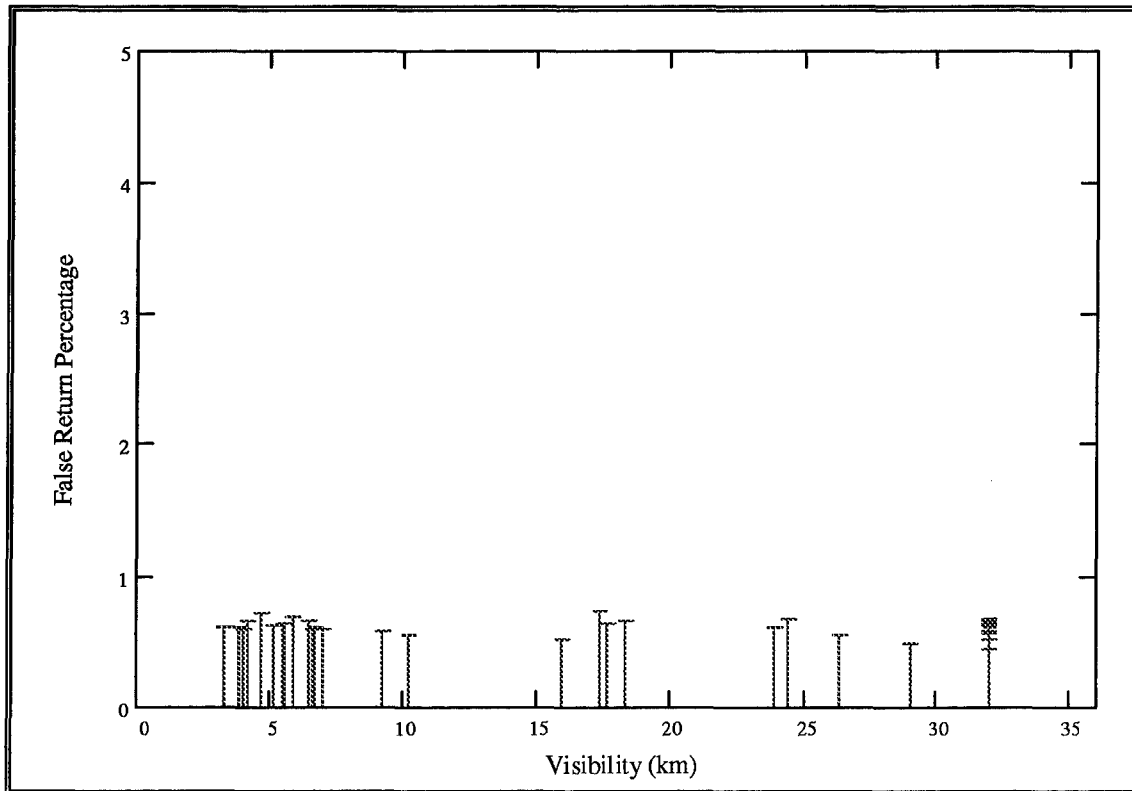
Figure 4.32 False Return Percentage vs. Visibility on 2 November (light rain)
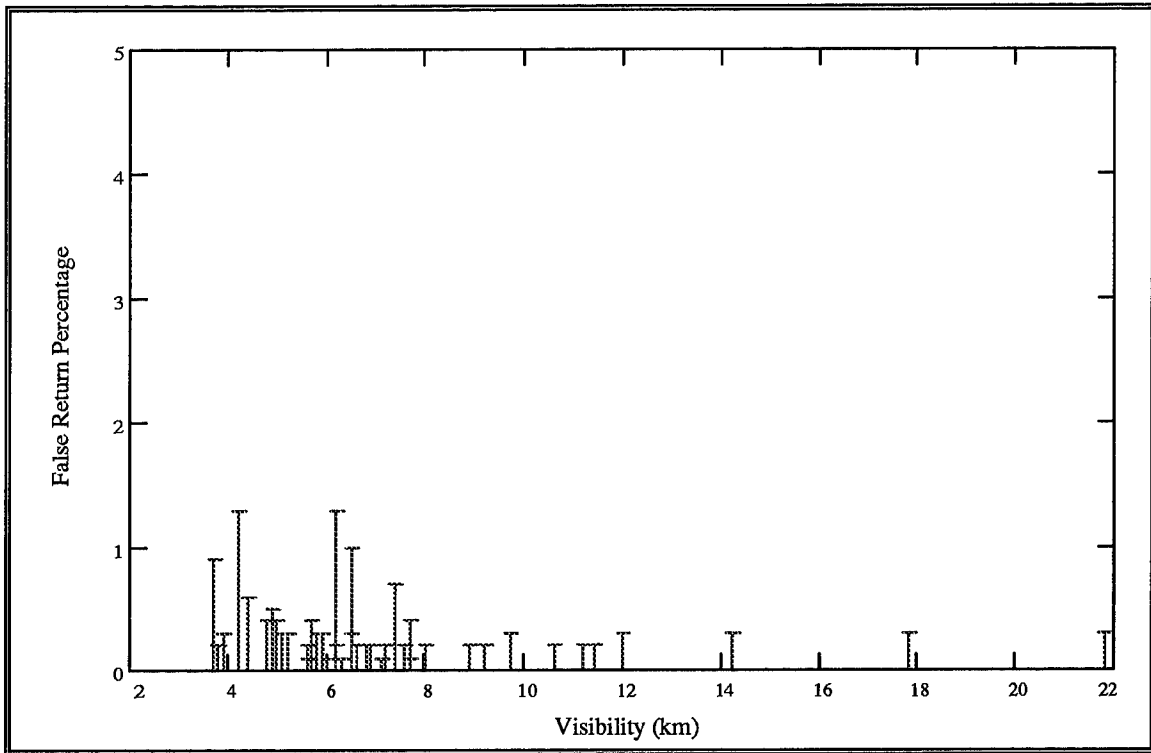
Figure 4.33 False Return Percentage vs. Visibility on 18 December (light rain)
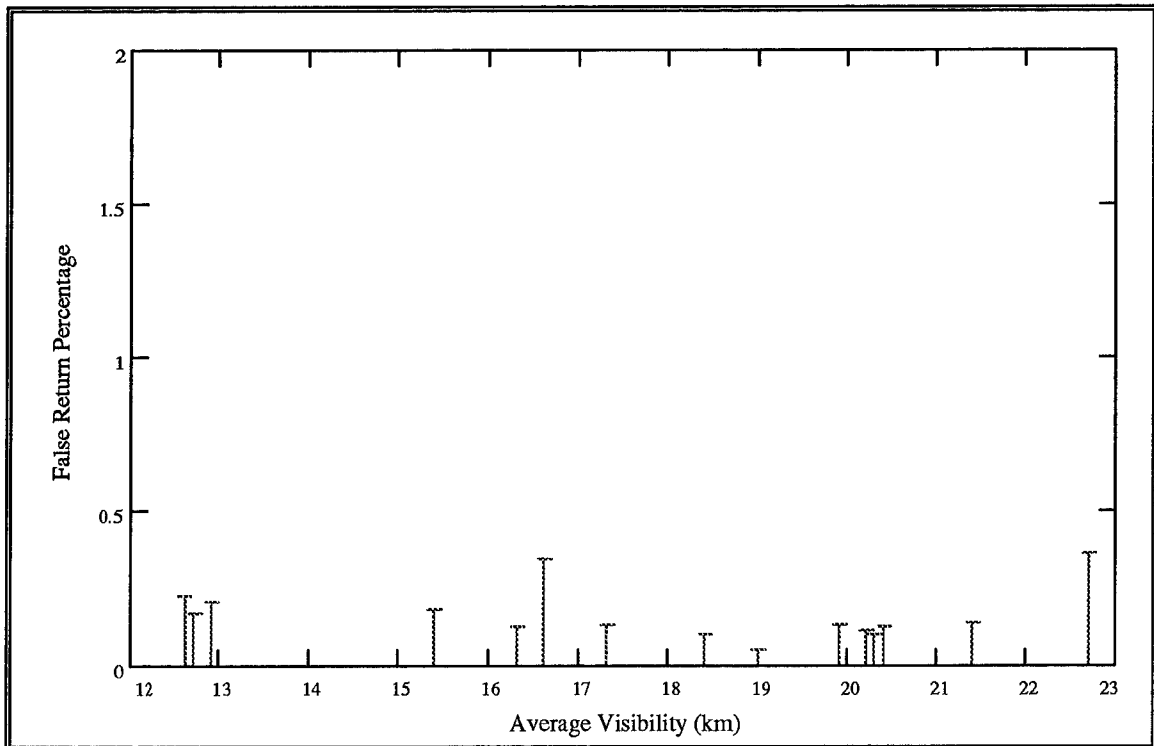
Figure 4.34 False Return Percentage vs. Visibility on 29 March (light fog)

61
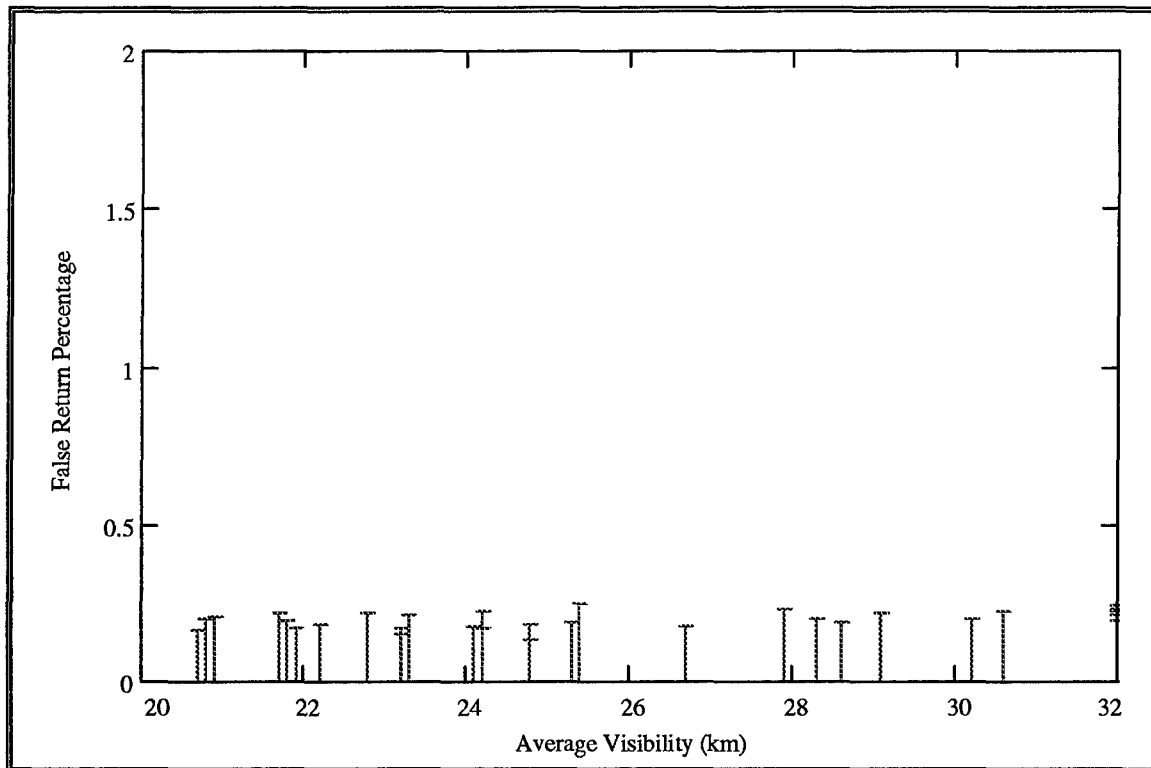
Figure 4.35 False Return Percentage vs. Visibility on 4 April (light fog)

Figures 4.30 through 4.35, all with fairly high visibilities, show little variance in false return percentage with visibility. In addition, the percentages, for the most part, are 1% or less, characterizing that they are predominantly system noise. These two factors indicate that false returns have little dependence on visibility, except in thick fog and heavy rain. The data from 15 March and 25 March clearly show that visibility can affect false returns.

4.4.4 False Return Percentages vs. Rain Rate

The data presented in Figure 4.36 has a correlation coefficient of 0.90. This high degree of linearity is readily apparent, further evidenced by the computed best-fit line of $y=.269x + .023$. In contrast, Figure 4.37 shows highly scattered data. This again can probably be attributed to system noise, since the false return percentages remain below 1.5%. The computed best-fit line for this figure is $y=.079x + 0.268$. Figure 4.38 presents data that appears quite linear. However, the percentages remain largely constant without regard to rain rate, which is confirmed by the line $y=.03x + 0.591$.

Comparison of false returns to rain rate and to visibility show a distinct difference between the two weather variables. False returns show good correlation with rain rate. However, the false return response from the fog is much less distinct. Physically this makes sense. Rain drops, with their larger cross section, scatter more energy back toward the ladar (180° angle) because they intercept more of the radiation than the fog droplets. Even though there are more numerous fog droplets, it takes 25 raindrops (of radius 1 mm) as opposed to 250,000 fog droplets (of radius 10 μm) to fill up a 1 cm diameter laser beam. More backscattering creates more false returns. Higher rain rates have more raindrops, which leads to higher numbers of false returns.
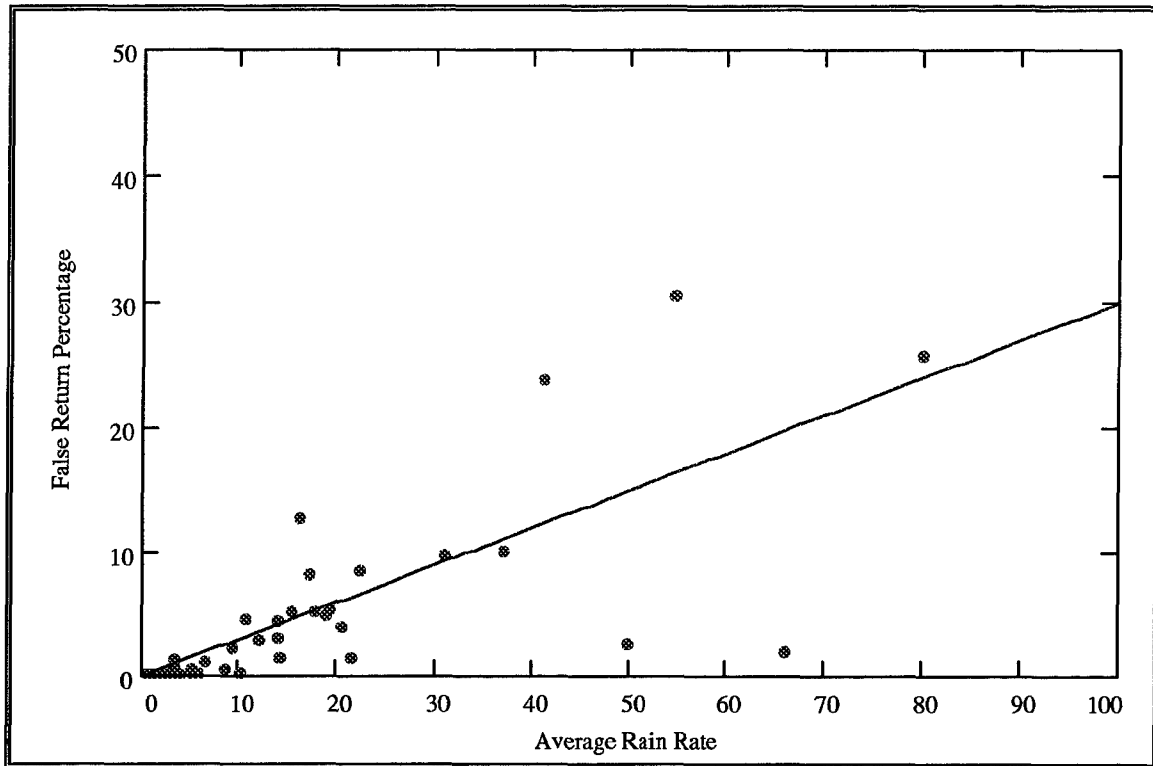
Figure 4.36 False Return Percentage vs. Average Rain Rate (mm hr^{-1}) for
25 March (heavy rain)
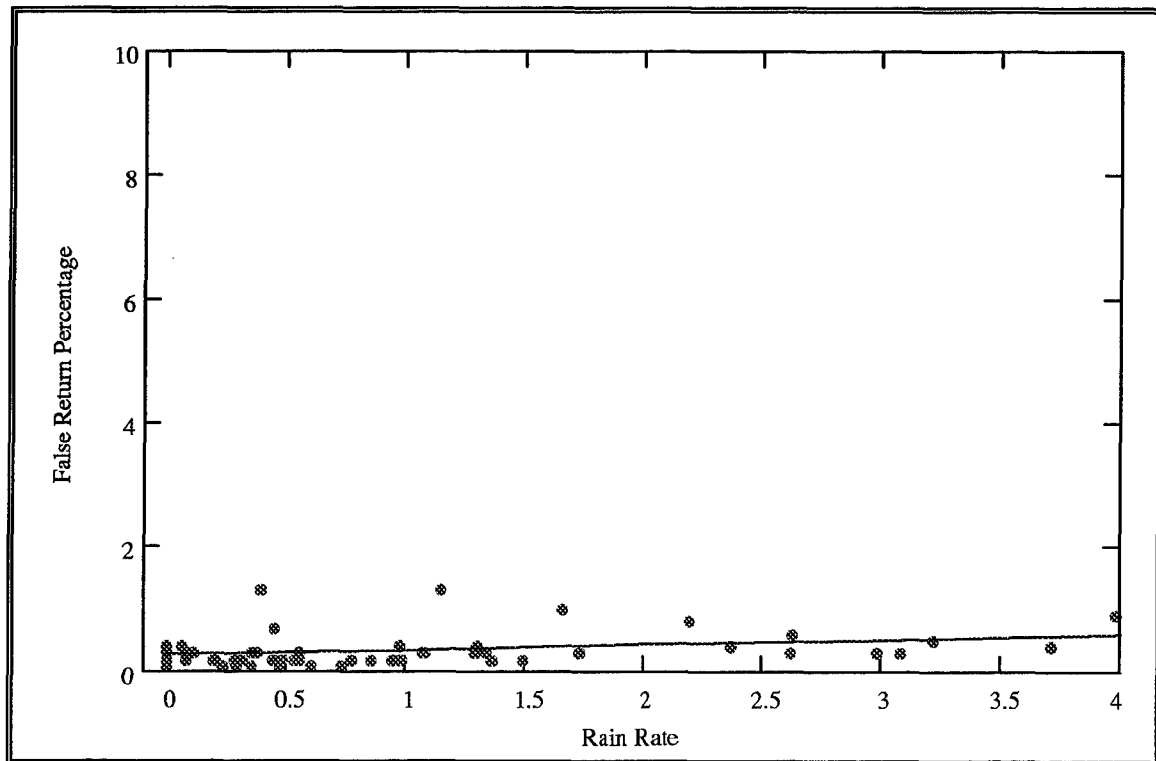
Figure 4.37 Percentage of False Returns vs. Rain Rate (mm hr^{-1}) for
18 December (light rain)
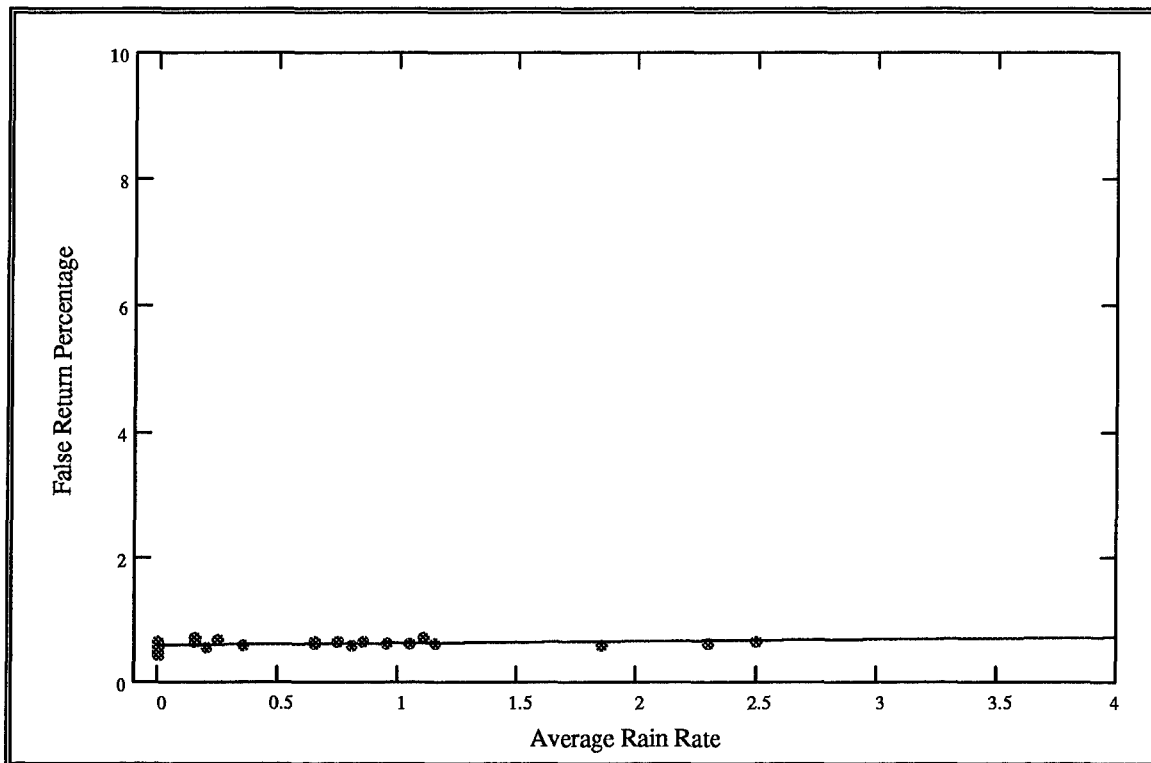
Figure 4.38 Percentage of False Returns vs. Average Rain Rate (mm hr^{-1}) for
2 November (light rain)

4.5 Quantitative Analysis of Degradation Percentage as a Function of Visibility

A by-product of plotting image degradation as a function of weather parameter is

the need to understand the quantities involved for all targets over all weather conditions.

The fitted equations are not useful in this sense because they are specific to each day.

Their main purpose was to aid in describing the plots. What is useful is a means of

expecting a certain percentage of dropouts or false returns for a given visibility interval.

The next two sections present descriptive statistics of all days of data over all visbilities,

resulting in expected values, standard deviations, and confidence intervals for false return

and dropout percentages with this ladar system.

4.5.1 Target Percentage of Dropouts

Table 4.8 presents the computed means and standard deviations for target dropout percentage based on all imaged targets over the eight days of collected data. These statistics are grouped according to visibility interval, which were chosen on the likelihood of being accurately forecast. An Air Force meteorologist should be expected to forecast 0.5 km visibility windows fairly accurately in the presence of heavy rain and fog. Given the state of the science, forecasts of 100 meter windows would be unreasonable. The windows increase to 1 km resolution for the sake of corralling more data points for a sufficient statistical analysis. Figures 4.39 and 4.40 are plots of the mean and standard deviation data from Table 4.8. The shapes of these graphs resemble the exponential shape of some of the previous dropout percentage vs. visibility bar graphs. Table 4.9 gives the same data as Table 4.8, except it is separated into categories of weather type. Statistical tests of visibility intervals 1,2,3, and 35 indicate that the mean percentages from the rain days and fog days are not statistically different from each other at a significance level of 0.02. Therefore we cannot say that low visibility on fog days causes more dropouts than low visibility on rain days. Table 4.10 then presents computed 95% confidence intervals of the dropout percentage for each visibility interval. Intervals denoted by "N/A" indicate not enough data points were available for the computation.

Table 4.6 Mean Dropout Percentages and Standard Deviations for Visibility Intervals

Interval Number	Visibility	Mean (%)	Standard Deviation	Number of Data Points
1	0.2 to 0.5	52.7	26.0	34
2	0.6 to 1.0	36.8	27.1	19
3	1.1 to 1.5	22.2	20.7	19
4	1.6 to 2.0	18.9	19.4	8
5	2.1 to 2.9	32.8	16.6	2
6	3.0	9.5	4.7	17
7	4.0	11.5	13.5	16
8	5.0	7.9	3.9	33
9	6.0	8.7	4.3	34
10	7.0	8.7	3.7	24
11	8.0	8.0	4.7	15
12	9.0	7.7	4.9	19
13	10.0	9.2	4.5	10
14	11.0	11.4	9.6	20
15	12.0	7.0	4.5	13
16	13.0	7.2	4.9	2
17	14.0	6.4	2.0	3
18	15.0	9.4	6.1	12
19	16.0	7.9	5.1	11
20	17.0	5.1	3.9	10
21	18.0	5.4	3.7	6
22	19.0	3.8	3.6	8
23	20.0	4.6	2.5	13
24	21.0	5.6	3.5	12
25	22.0	5.7	2.9	5
26	23.0	6.4	2.3	8
27	24.0	5.1	2.8	12
28	25.0	6.4	2.6	4
29	26.0	6.4	.2	3
30	27.0	2.8	1.8	2
31	28.0	5.2	2.3	4
32	29.0	4.6	3.4	4
33	30.0	4.8	2.5	4
34	31.0	N/A	N/A	0
35	32.0	4.9	2.9	47

Table 4.7 Mean Dropout Percentages and Standard Deviations for Visibility Intervals by Weather Type

| Visibility (km)	Fog Day Mean (%)	Fog Day Std Dev	Number of Data Points	Rain Day Mean (%)	Rain Day Std Dev	Number of Data Points
0.2 to 0.5	51.4	30.5	22	50.8	14.8	12
0.6 to 1.0	31.6	32.1	13	44.6	13.2	6
1.1 to 1.5	18.1	20.9	14	33.7	15.1	5
1.6 to 2.0	34.5	31.0	2	13.7	8.7	6
2.1 to 2.9	N/A	N/A	0	32.8	16.6	2
3.0	9.3	4.8	5	9.7	4.8	12
4.0	36.5	24.1	2	7.8	3.0	14
5.0	7.2	5.9	4	8.0	3.5	29
6.0	N/A	N/A	0	8.7	4.3	34
7.0	9.4	4.6	10	8.2	2.7	14
8.0	8.9	6.7	5	7.5	3.1	10
9.0	10.0	5.5	7	6.3	3.9	12
10.0	10.6	5.2	6	7.0	1.6	4
11.0	10.8	5.1	10	18.1	21.9	10
12.0	6.9	4.2	9	7.3	5.1	4
13.0	N/A	N/A	0	7.2	4.9	2
14.0	7.3	0.0	1	6.0	2.3	2
15.0	11.4	5.8	8	5.3	4.6	4
16.0	8.2	5.1	9	6.5	5.0	2
17.0	4.5	2.7	2	5.3	4.2	8
18.0	4.8	3.3	2	5.7	3.9	4
19.0	3.0	2.5	6	6.1	5.1	2
20.0	4.6	2.6	12	4.5	0.0	1
21.0	4.9	2.3	8	6.9	4.8	4
22.0	8.9	5.0	5	N/A	N/A	0
23.0	6.3	2.4	6	6.6	2.0	2
24.0	5.4	2.6	10	3.7	3.4	2
25.0	6.4	2.6	4	N/A	N/A	0
26.0	6.3	0.2	2	6.7	0.0	1
27.0	2.8	1.8	2	N/A	N/A	0
28.0	5.2	2.3	4	N/A	N/A	0
29.0	5.3	3.5	2	3.8	3.1	2
30.0	4.8	2.5	4	N/A	N/A	0
31.0	N/A	N/A	0	N/A	N/A	0
32.0	5.9	2.4	11	4.6	3.0	36
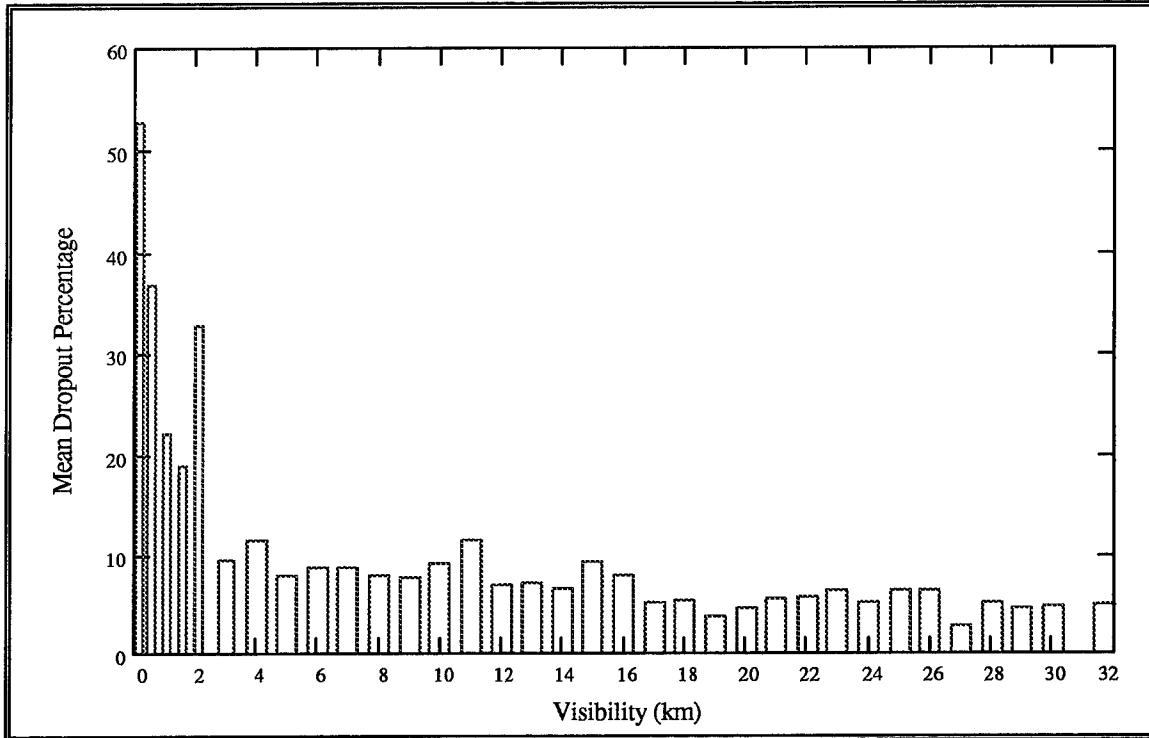
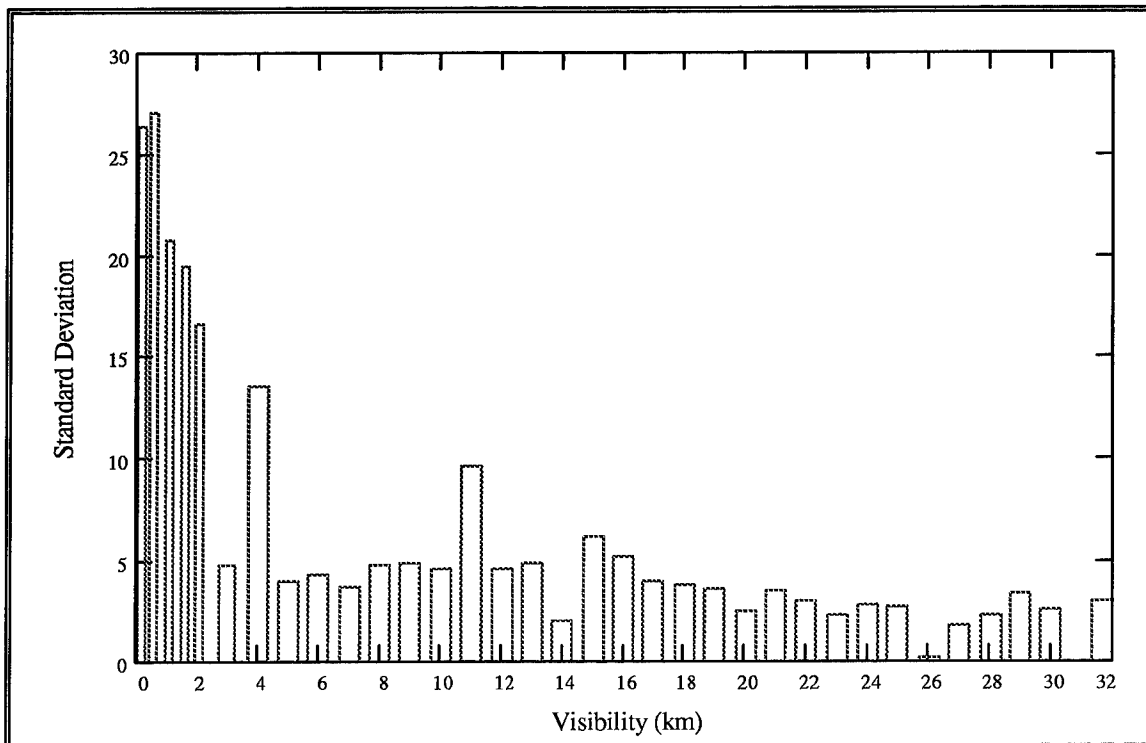Figure 4.39 Mean Dropout Percentage for Each Visibility Interval

Figure 4.40 Standard Deviation of the Mean Dropout Percentage

Table 4.8 95% Confidence Intervals for the Mean Percentage of Target Dropouts

Interval Number	Visibility (km)	95% CI Lower Bound	95% CI Upper Bound
1	0.2 to 0.5	42.9	62.5
2	0.6 to 1.0	24.1	49.4
3	1.1 to 1.5	11.9	32.4
4	1.6 to 2.0	1.5	36.2
5	2.1 to 2.9	N/A	N/A
6	3.0	7.1	11.9
7	4.0	3.8	19.3
8	5.0	6.5	9.4
9	6.0	7.2	10.2
10	7.0	7.1	10.3
11	8.0	5.2	10.7
12	9.0	5.3	10.1
13	10.0	5.8	12.6
14	11.0	6.7	16.1
15	12.0	4.2	9.8
16	13.0	N/A	N/A
17	14.0	.4	12.4
18	15.0	5.3	13.4
19	16.0	4.3	11.5
20	17.0	2.1	8.1
21	18.0	1.1	4.1
22	19.0	.5	7.0
23	20.0	3.0	6.1
24	21.0	3.3	7.9
25	22.0	1.7	9.8
26	23.0	4.3	8.4
27	24.0	3.2	6.9
28	25.0	1.5	11.2
29	26.0	5.7	7.1
30	27.0	N/A	N/A
31	28.0	.9	9.4
32	29.0	0.0	10.8
33	30.0	.2	9.4
34	31.0	N/A	N/A
35	32.0	4.1	5.8

The dropout system noise of the ladar can be characterized from these tables. Averaging the dropout percentages for all targets with visibility greater than 12 km (7.5 mi) gives an average dropout percentage of 5.7%. This value can be characterized as the average ladar system noise. However, in early November the ladar hardware experienced a power surge. After it was repaired, the laser lab personnel suspected that the system noise had increased on the data taken in November and December. Averaging the dropout percentages before 2 November yields a mean of 5.4% with a standard deviation of 3.4 for 114 data points. Averaging the dropouts percentages for 2 November and afterward yields a mean of 6.3% with a standard deviation of 4.6 for 70 data points. Performing a large sample statistical z-test at a significance level of $\alpha = .01$ indicates that the true mean dropout percentages are not statistically different. Thus, the power surge had minimal effect on the system noise.

4.5.2 False Return Percentage

Table 4.11 presents the computed means and standard deviations for false return percentage based on the eight days of collected data, grouped according to visibility interval. Figures 4.41 and 4.42 are plots of the mean and standard deviation data from Table 4.10. Table 4.12 then presents computed 95% confidence intervals of the false return percentage for each visibility interval. Intervals denoted by "N/A" indicate not enough data points were available for the computation

Table 4.9 Mean False Return Percentages and Standard Deviations for Visibility Intervals

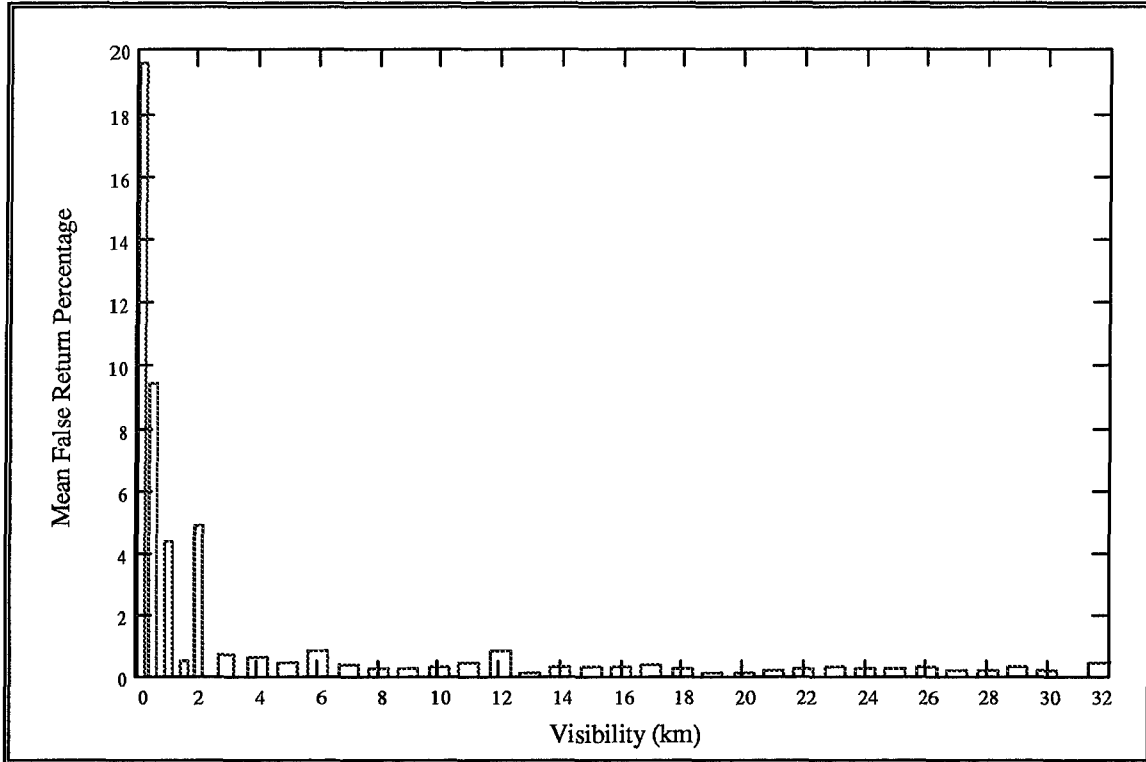| Interval Number	Visibility (km)	Mean (%)	Standard Deviation	Number of Data Points
1	0.2 to 0.5	19.5	21.3	19
2	0.6 to 1.0	9.4	13.6	11
3	1.1 to 1.5	4.3	9.4	9
4	1.6 to 2.0	.5	.3	5
5	2.1 to 2.9	4.9	0.0	1
6	3.0	.7	.4	8
7	4.0	.6	.3	9
8	5.0	.4	.2	17
9	6.0	.8	1.9	17
10	7.0	.4	.2	10
11	8.0	.3	.1	8
12	9.0	.3	.2	9
13	10.0	.4	.2	6
14	11.0	.4	.3	8
15	12.0	.8	1.6	7
16	13.0	.1	0.0	1
17	14.0	.4	.1	2
18	15.0	.3	.2	5
19	16.0	.3	.2	6
20	17.0	.4	.3	5
21	18.0	.3	.2	3
22	19.0	.1	0.0	3
23	20.0	.2	.1	6
24	21.0	.2	.1	6
25	22.0	.3	.1	3
26	23.0	.3	.2	4
27	24.0	.3	.2	6
28	25.0	.3	.1	2
29	26.0	.4	.2	2
30	27.0	.2	0.0	1
31	28.0	.2	0.0	2
32	29.0	.4	.2	2
33	30.0	.2	0.0	2
34	31.0	N/A	N/A	0
35	32.0	.5	.2	23

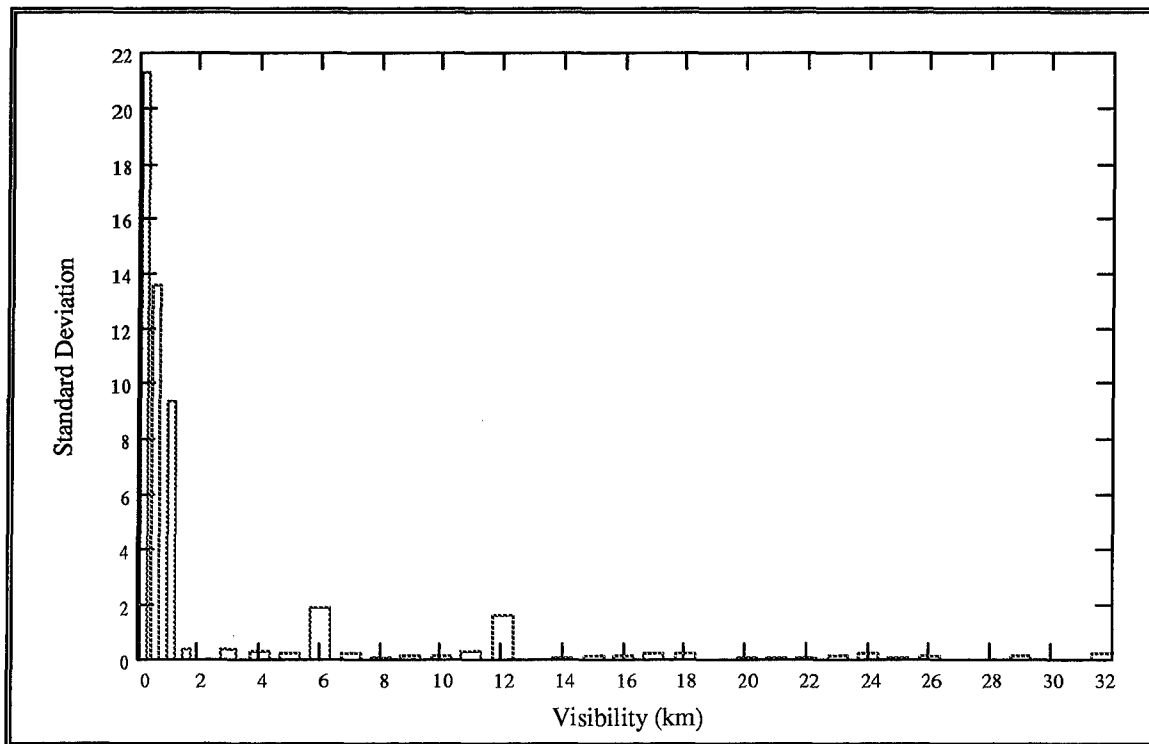Figure 4.41 Mean False Return Percentage for Each Visibility Interval

Figure 4.42 Standard Deviation of the Mean False Return Percentage

73

Table 4.10 95% Confidence Intervals for the Mean False Return Percentage

Interval Number	Visibility (km)	95% CI Lower Bound	95% CI Upper Bound
1	0.2 to 0.5	8.9	30.1
2	0.6 to 1.0	0.0	19.0
3	1.1 to 1.5	0.0	12.0
4	1.6 to 2.0	.1	1.0
5	2.1 to 2.9	N/A	N/A
6	3.0	.3	1.0
7	4.0	.4	.8
8	5.0	.3	.5
9	6.0	0.0	1.8
10	7.0	.2	.6
11	8.0	.2	.3
12	9.0	.1	.4
13	10.0	.2	.5
14	11.0	.2	.7
15	12.0	0.0	2.4
16	13.0	N/A	N/A
17	14.0	N/A	N/A
18	15.0	.1	.6
19	16.0	.1	.5
20	17.0	0.0	.7
21	18.0	0.0	1.0
22	19.0	.1	.1
23	20.0	.1	.2
24	21.0	.1	.3
25	22.0	0.0	.6
26	23.0	0.0	.6
27	24.0	0.0	.5
28	25.0	N/A	N/A
29	26.0	N/A	N/A
30	27.0	N/A	N/A
31	28.0	N/A	N/A
32	29.0	N/A	N/A
33	30.0	N/A	N/A
34	31.0	N/A	N/A
35	32.0	.4	.6

4.6 Mean Distance of False Returns

Table 4.13 gives the data for the mean distance of the false returns. The minimum, maximum, mean, and standard deviation are listed by date. The days are listed in descending order of weather severity with the fog days first, and then the rain days. Overall, the means and standard deviations remain close for all of the days. The exceptions are 29 March and 30 October. The 29 March mean of 88.5 m is somewhat lower than most, while the 30 October mean distance of 213.3 m is more than 70 m greater than the next closest mean. Graphs of the mean distance as a function of visibility and rain rate are presented in *Appendix D*. Some appear to have an exponential shape, while others are horizontal lines. The trends indicate that the mean distances decrease as the rain rate increases and the visibility decreases.

Table 4.11 Mean Distance of False Returns

Date	Minimum (m)	Maximum (m)	Mean (m)	Standard Deviation
15 March	112.8	140.0	130.6	10.5
30 October	206.5	226.7	213.3	4.7
6 December	121.9	146.2	134.9	5.9
29 March	54.4	140.8	127.0	20.0
4 April	129.9	142.0	135.8	3.6
25 March	46.8	152.7	88.5	29.9
18 December	60.0	162.0	142.2	18.9
2 November	118.7	139.4	136.4	3.7

V. Summary, Conclusions, and Recommendations

5.1 Summary

The Air Force is developing the use of imaging laser radar systems as guidance systems on future precision guided munitions. The Wright Laboratory is currently testing a direct detection 1.06 μm wavelength ladar at Eglin Air Force Base. Since laser radiation can be susceptible to propagation problems through weather, quantitative understanding of these effects is important to the development of this weapon system.

Ladar image degradation, in the form of target dropouts and false returns, was evaluated in various weather conditions. Statistical analysis of the images presented expected degrees of degradation according to visibility and rain fall rate. While only an elementary step in development of this system, this thesis has provided some understanding of the effects of weather on imaging laser radar.

5.2 Conclusions

For the majority of the weather data observed for this thesis, there was little effect on ladar image degradation. However, the effects became significant when the weather was poorest. Once visibility fell below 1 km and rain rates reached above 4 mm hr^{-1}, the percentages of dropouts and false returns climbed above the system noise of the ladar, which is generally 12% or less for dropouts, and 1% or less for false returns. At that point, trends in the relationships between image degradation and weather became apparent.

Dropouts generally appear as an exponential function of visibility as visibilities fall below 2 km. This trend is determined from the data of 15 March and 25 March, since

those were the only two days with a significant number of data points below 2 km. The dropout data from 30 October has a sizable number of data points below 2 km. However, the visibility measurements are probably not representative of the true fog conditions since they were made with only one sensor. For visibilities above 2 km, system noise appears to dominate the results.

Evidence presented in Chapter 4 indicates that dropouts are a linear function of rain rate. The six graphs presented show a good linear fit to the data points. However, the correlation coefficients for the data on 2 November and 18 December are less than the 0.70 needed to quantitatively show good linear correlation. Dropouts vary from 0-10% of the target with zero rain rate on these days. This system noise influences the correlation coefficients. On 25 March, the rain rates are significantly higher than those of 2 November and 18 December. Correlation coefficients of 0.67 for the tank and 0.91 for the building, along with the graphical fits to the data, show very good linearity. Thus, the linear relationship becomes apparent for rain rates greater than 4 mm hr^{-1}.

Like dropouts, false returns show characteristics of being an exponential function of visibility. However, this relation is not as strong as the one for dropouts. Only the heavy rain and fog exhibited in March present evidence of an exponential relation. All other days show a nearly constant number of false returns as visibility varies from 0.2 to 32 km, indicating that system noise is being observed. The data indicate that the false return noise is almost exclusively 1% or less of the target area.

The strongest relation observed results from false returns versus rain rate. Although there are only three data sets, false returns show a strong linear relation with rain rate in all three. The data from 2 November and 18 December show a very good fit

to their respective lines. However, since they have low rain rates, system noise influences the results, keeping the correlation coefficients low. But the data from 25 March presents the greatest evidence of true linearity. The correlation coefficient for false returns versus rain rate on this day is 0.90. In addition, the data points confirm very well to the best-fit line over a tremendous range of rain rates. The high rain rates expel most system noise contamination and let the true nature of the relationship emerge.

5.3 Recommendations

A tremendous amount of data is required to determine a conclusive relationship between ladar image degradation and weather. The scientists at the Wright Laboratory laser lab are in the process of collecting that data. This thesis has been a preliminary step in the development of this ladar system and more data is required for adequate study. In addition, the type of data is important. This thesis has shown that for high visibilities and low rain rates, the weather has little effect on image degradation. The poorest weather shows the greatest response from the ladar. Unfortunately, poor weather data is relatively sparse. Therefore, efforts should be made to acquire as much data as possible from the worst weather conditions.

The effectiveness of data gathering by the laser lab personnel at Eglin has been somewhat inhibited by their lack of ownership of the meteorological equipment. They have an autonomous ability to take ladar images, but the weather data must be gathered by someone else. This has led to missing opportunities to image in poor weather. The sponsors of this thesis are in the process of purchasing their own weather instrumentation,

which would make the entire data gathering process their own and allow them to gather weather data whenever they need it.

The setup of the weather instrumentation is also important. Two visibility sensors are indeed necessary for adequate representation of the visibility conditions. Due to the small scale and advective nature of fog, the need for near and far visibility sensors is apparent to average the visibility over 500 m. In addition, if fiscal considerations come into play, one rain rate sensor in the middle of the range would suffice.

Finally, the most important data necessary to proper analysis of the weather parameters was not available. Fog droplet and raindrop size distributions were the key to unlocking the true relationships between weather and ladar image degradation. For unknown reasons, the fog droplet size probe failed to give any readings whatsoever. Additionally, the raindrop size spectrometer produced distributions which did not coincide with measured rain rates. Accurate size distribution data would greatly enhance our understanding of the relationships studied here.
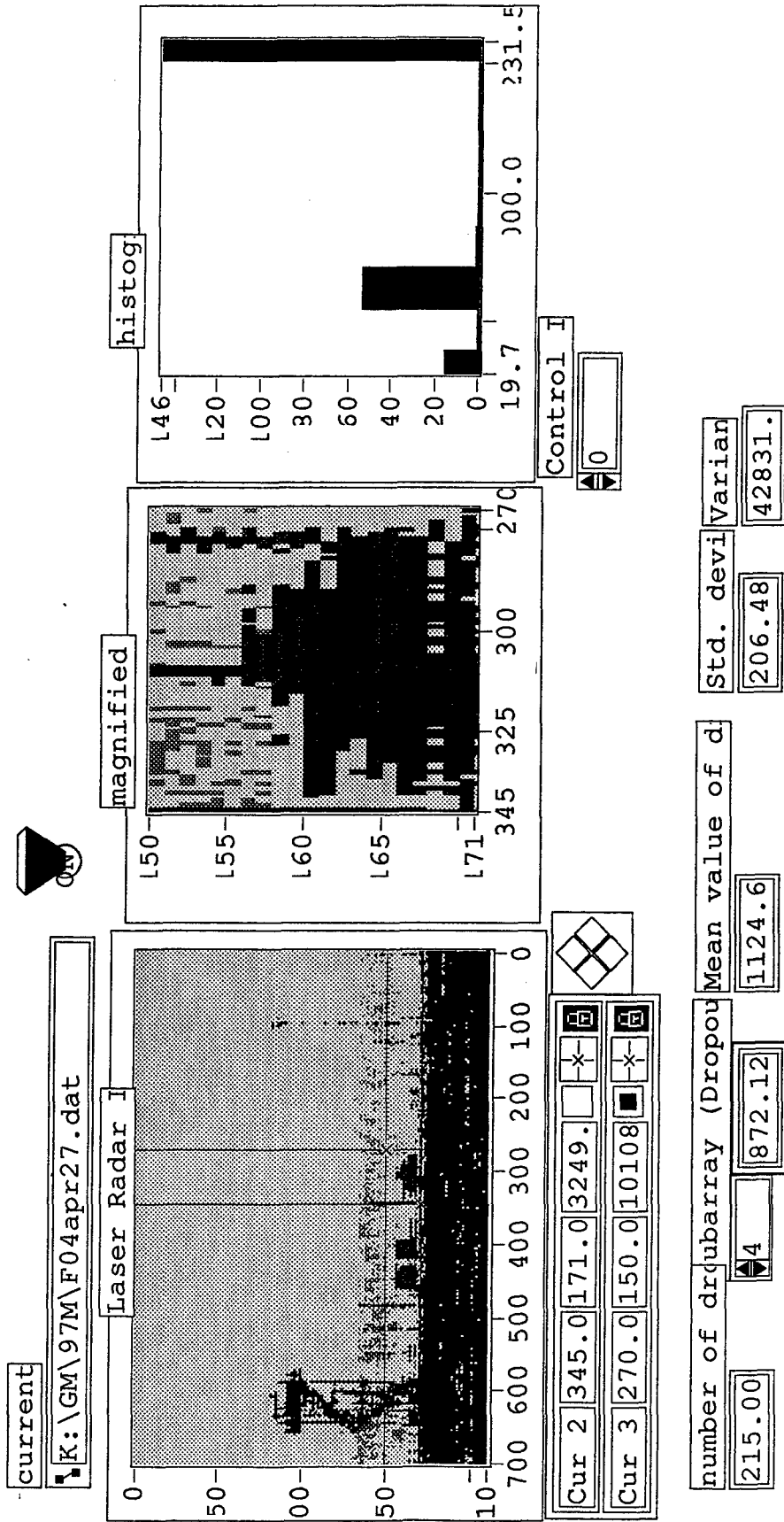
Appendix B. Raw Data for Calculated and Measured Rain Rates

Table B-1 Comparison of Calculated and Measured Rain Rates (mm hr^{-1}) for 25 March

Time	Measured	Calculated	Time	Measured	Calculated
8:49	0.00	0.00	**9:41**	0.00	0.68
8:50	0.00	0.00	**9:42**	0.00	0.40
8:51	2.19	0.77	**9:43**	0.00	0.17
8:52	9.40	35.14	**9:44**	0.00	0.20
8:53	10.84	13.01	**9:45**	0.00	0.02
8:54	1.50	11.90	**9:46**	0.00	0.15
8:55	0.43	3.88	**9:47**	0.00	0.94
8:56	0.00	3.08	**9:48**	0.00	0.29
8:57	0.00	2.00	**9:49**	0.00	0.01
8:58	0.00	0.15	**9:50**	0.00	0.00
8:59	0.00	0.10	**9:51**	0.00	0.10
9:00	0.00	0.06	**9:52**	0.00	0.18
9:01	0.00	0.05	**9:53**	0.60	1.59
9:03	0.00	1.89	**9:54**	0.55	3.70
9:04	0.00	0.05	**9:55**	0.46	4.25
9:05	3.47	0.01	**9:56**	0.48	3.28
9:06	0.00	0.24	**9:57**	0.39	5.04
9:08	0.80	0.52	**9:58**	0.00	3.74
9:09	0.45	4.09	**9:59**	0.00	3.12
9:10	3.73	11.88	**10:00**	0.00	1.82
9:11	2.69	10.91	**10:01**	0.00	0.71
9:13	0.26	3.91	**10:02**	0.00	0.62
9:14	0.30	2.82	**10:03**	0.00	0.77
9:15	0.36	1.39	**10:04**	0.00	2.59
9:16	0.58	1.51	**10:05**	0.00	0.91
9:18	0.00	1.62	**10:06**	0.00	1.27
9:19	0.00	0.55	**10:07**	0.00	0.06
9:20	0.00	0.10	**10:09**	0.00	0.08
9:21	0.00	0.10	**10:10**	0.00	0.04
9:22	0.00	0.56	**10:11**	0.00	0.03
9:23	40.09	16.16	**10:12**	4.13	13.91
9:24	30.90	140.54	**10:13**	54.08	128.02
9:25	16.11	78.6	**10:14**	16.44	42.04
9:26	13.49	31.48	**10:15**	21.33	17.08
9:27	5.69	27.74	**10:16**	14.49	30.72
9:28	4.39	26.02	**10:17**	13.34	20.77
9:29	3.80	22.35	**10:18**	13.68	44.44
9:30	2.29	30.54	**10:19**	26.06	114.13
9:31	17.91	16.79	**10:20**	47.53	145.82
9:32	14.26	60.67	**10:21**	115.88	535.78
9:33	1.66	47.56	**10:22**	88.10	1160.72
9:34	0.38	11.72	**10:23**	174.58	863.57
9:35	0.00	8.27	**10:24**	194.09	868.47
9:36	0.00	5.97	**10:25**	160.32	572.62
9:37	0.00	3.19	**10:27**	24.55	831.30
9:38	0.00	0.84	**10:28**	17.66	935.46
9:39	0.00	0.50	**10:29**	22.80	643.21
9:40	0.00	1.30	**10:30**	66.53	382.00

Table B-2 Comparison of Calculated and Measured Rain Rates (mm hr^{-1}) for 2 November

Time	Calculated	Measured	Time	Calculated	Measured
8:05	0.42	0.00	8:53	17.24	0.20
8:06	1.18	0.00	8:54	14.09	0.10
8:07	0.51	0.00	8:55	9.87	0.15
8:08	3.57	0.00	8:56	5.47	0.00
8:09	1.34	0.00	8:57	6.00	0.00
8:10	0.77	0.00	8:58	3.62	0.00
8:11	5.05	0.20	8:59	2.61	0.00
8:12	2.87	0.65	9:00	3.81	0.00
8:13	22.53	2.30	9:01	4.32	0.00
8:14	38.29	2.50	9:02	1.66	0.00
8:15	41.08	1.85	9:03	1.45	0.00
8:16	27.18	1.60	9:04	0.99	0.00
8:17	33.76	1.15	9:05	0.76	0.00
8:18	36.03	1.25	9:06	0.65	0.00
8:19	35.13	2.10	9:07	0.47	0.00
8:20	35.61	3.55	9:08	0.44	0.00
8:21	41.47	3.60	9:09	0.78	0.00
8:22	73.32	1.25	9:10	0.38	0.00
8:23	40.85	0.65	9:11	1.25	0.00
8:24	16.41	0.25	9:12	0.60	0.00
8:25	7.00	0.25	9:13	0.44	0.00
8:26	18.74	0.15	9:14	2.06	0.00
8:27	19.94	0.55	9:15	0.93	0.00
8:28	26.55	0.85	9:16	1.05	0.00
8:29	15.51	0.95	9:17	0.19	0.00
8:30	15.07	0.65	9:18	0.09	0.00
8:31	15.07	0.60	9:19	0.00	0.00
8:32	8.35	0.25	9:20	0.20	0.00
8:33	15.85	0.55	9:21	0.11	0.00
8:34	16.37	0.65	9:22	0.12	0.00
8:35	15.89	0.80	9:23	0.11	0.00
8:36	25.12	0.85	9:24	0.82	0.00
8:37	30.46	0.95	9:25	0.70	0.00
8:38	33.18	2.65	9:26	0.81	0.00
8:39	40.68	2.50	9:27	1.38	0.00
8:40	41.40	1.25	9:28	1.19	0.00
8:41	78.68	1.05	9:29	1.29	0.00
8:42	62.62	1.10	9:30	1.95	0.00
8:43	34.80	1.00	9:31	1.00	0.00
8:44	47.10	0.90	9:32	1.22	0.00
8:45	14.37	0.75	9:33	1.60	0.15
8:46	30.58	0.85	9:34	3.57	0.25
8:47	13.29	0.95	9:35	4.45	0.15
8:48	16.44	1.00	9:36	7.72	0.20
8:49	31.57	0.65	9:37	7.38	0.15
8:50	38.82	0.40	9:38	4.36	0.20
8:51	14.78	0.35	9:39	2.71	0.15
8:52	10.95	0.30	9:40	3.48	0.00
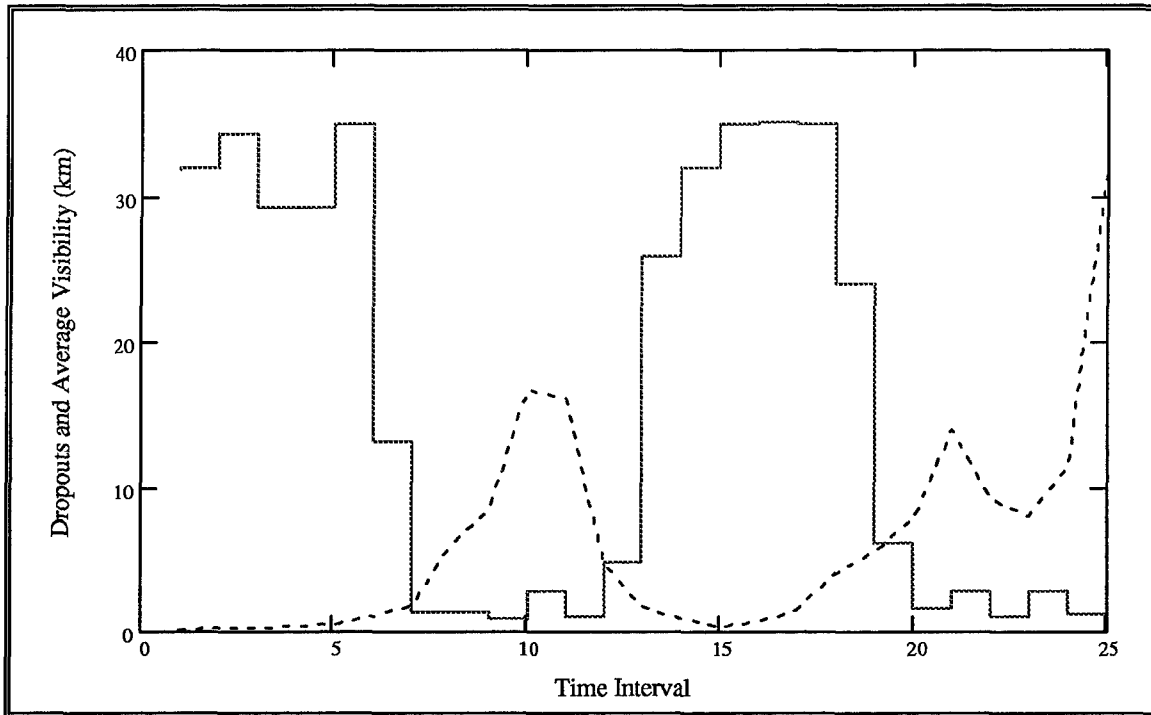
Figure C-1 Building Dropouts/10 (solid) and Average Visibility (km) on
15 March (thick fog)
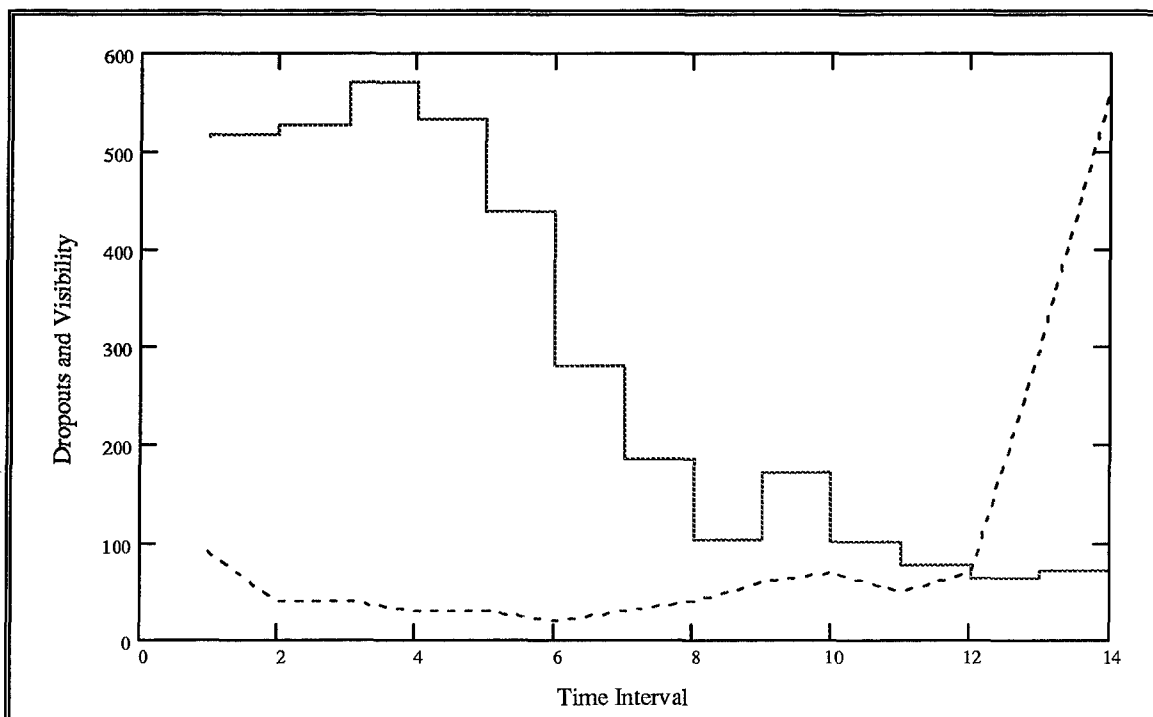
Figure C-2 Tank Dropouts (solid line) Divided by 100 (for scale) and Visibility
(dashed line) Over Time on 30 October
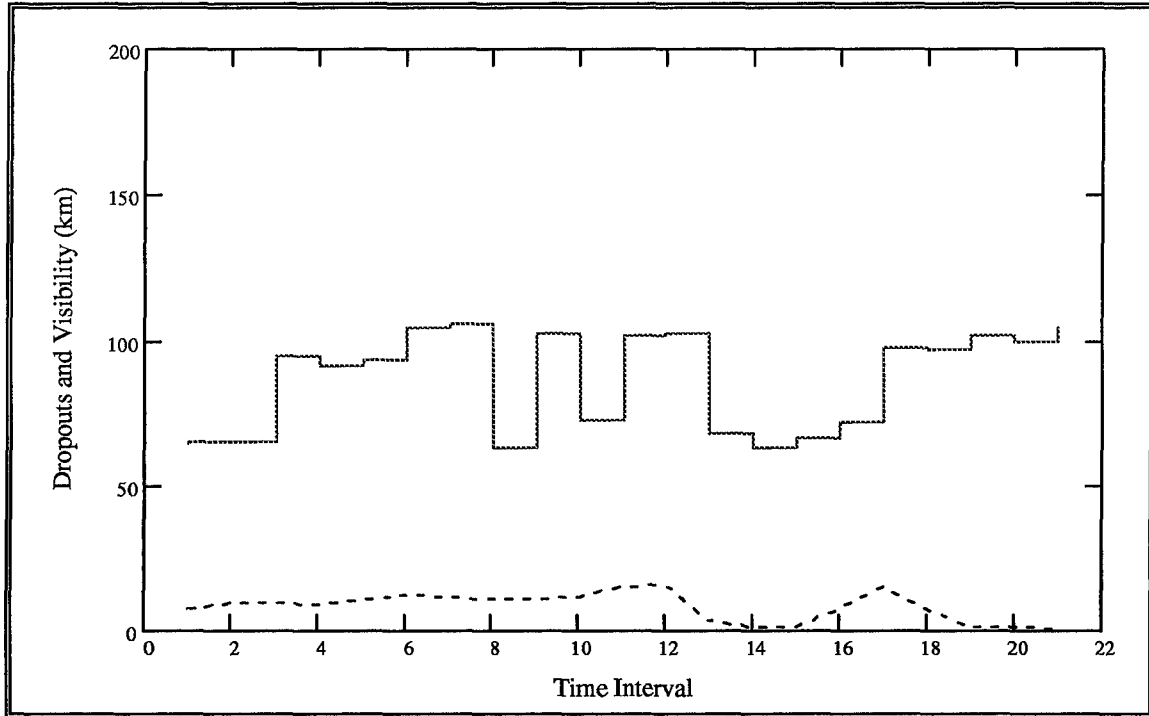
Figure C-3 Tank Dropouts (solid) and Visibility (dashed) Over Time for
6 December (light rain)
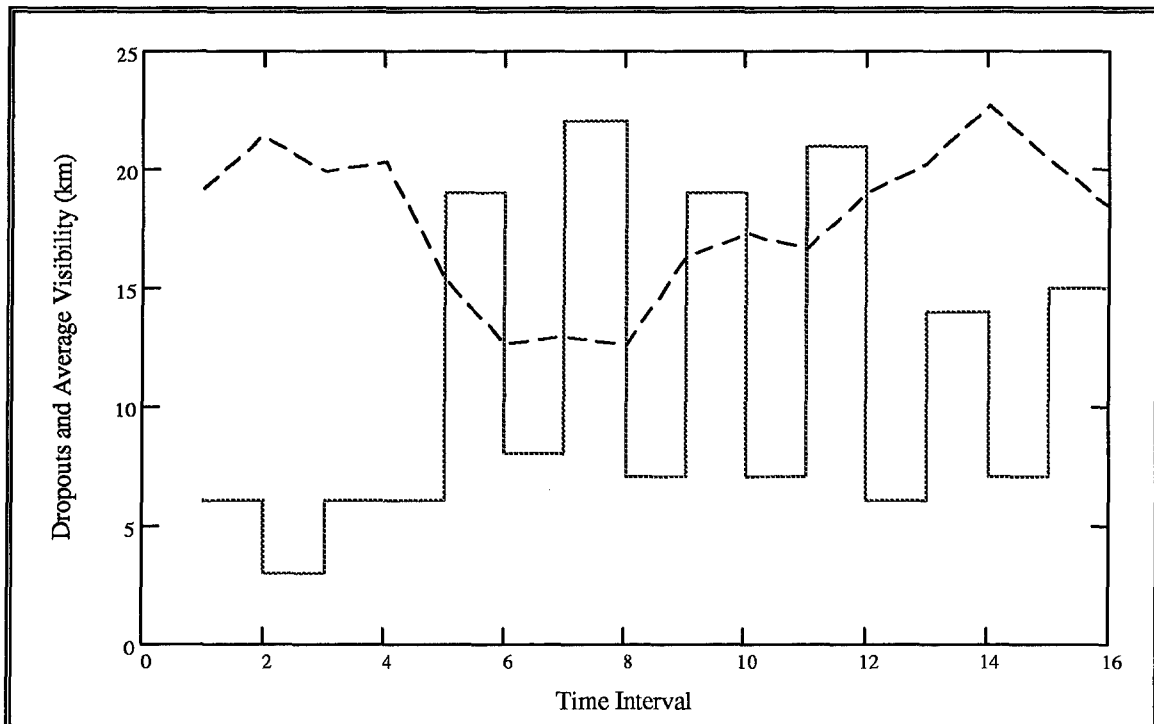
Figure C-4 Dropouts for the Building Target (solid) and Average Visibility (dashed) on
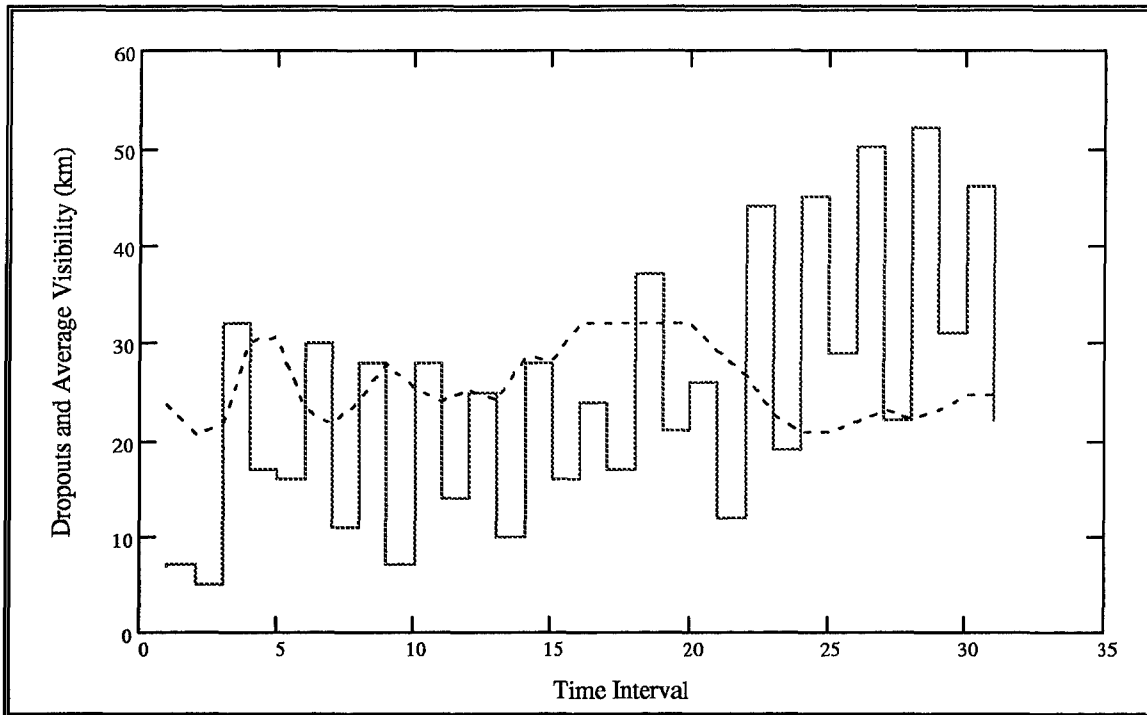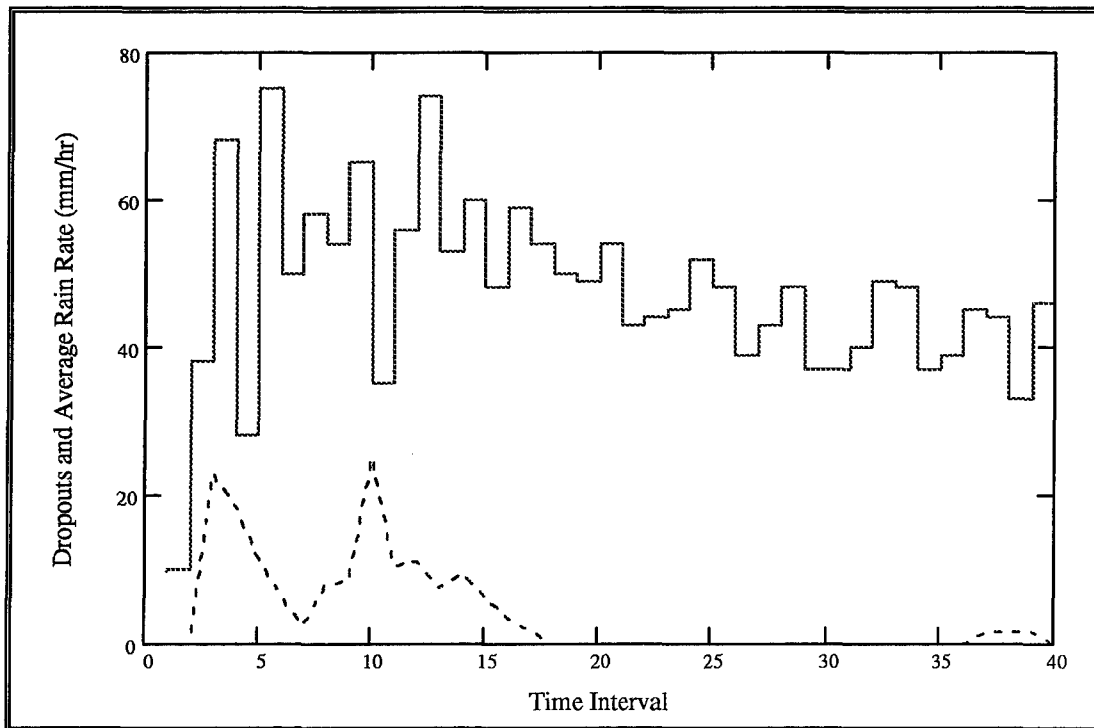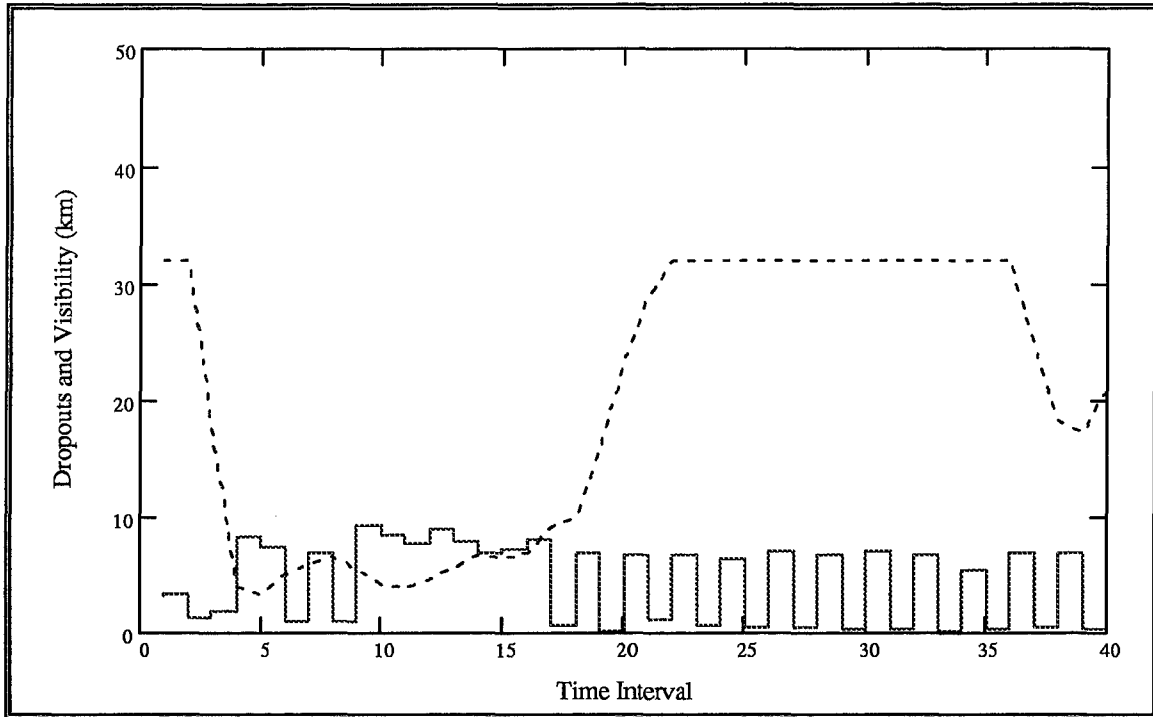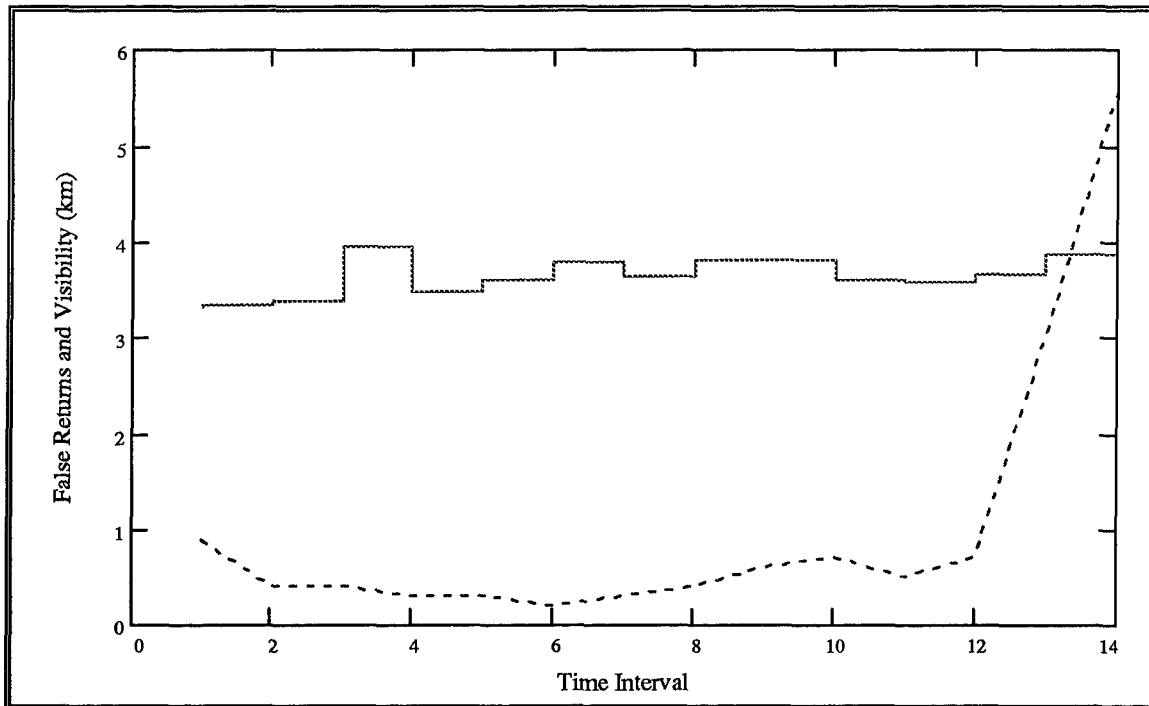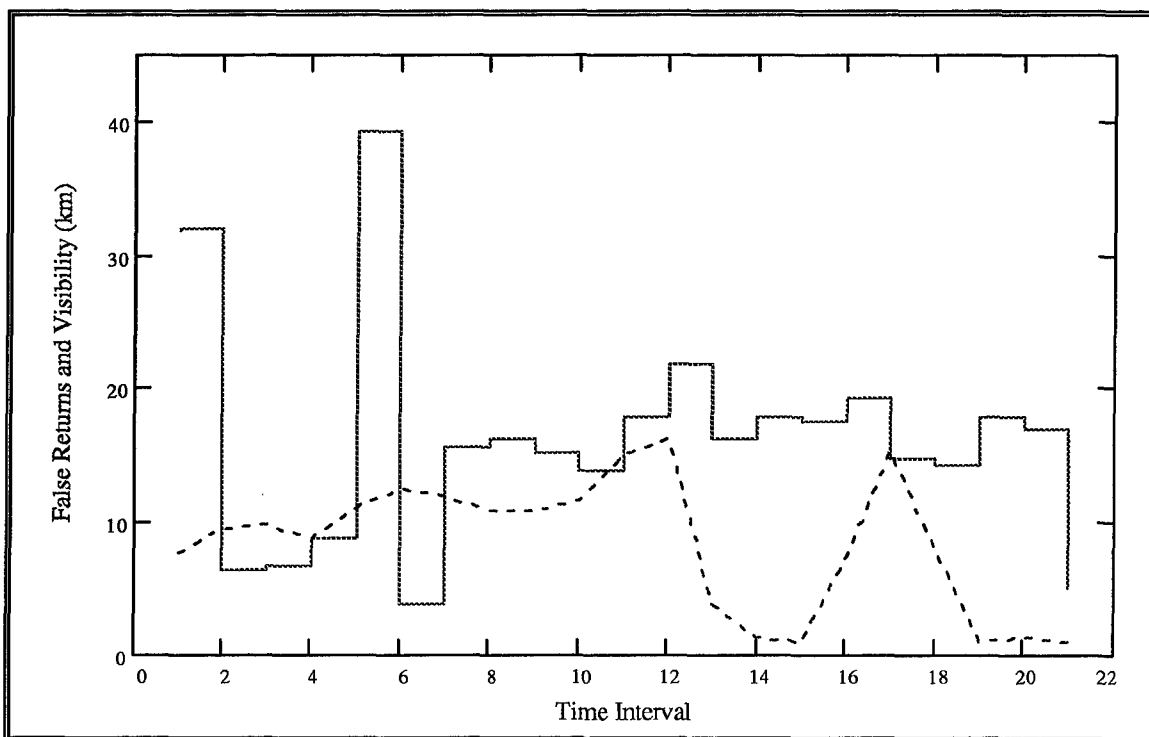29 March (light fog)
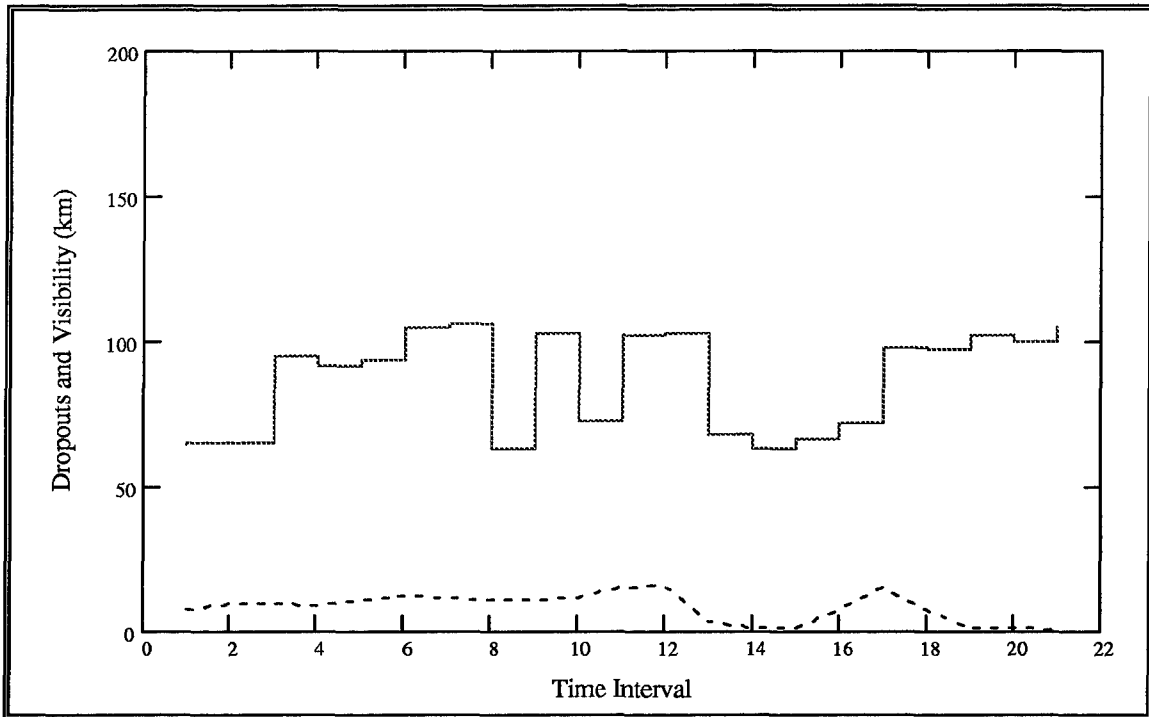
Figure C-5 Tank Target Dropouts (solid) and Visibility (dashed) Over Time for
6 December (moderate fog)
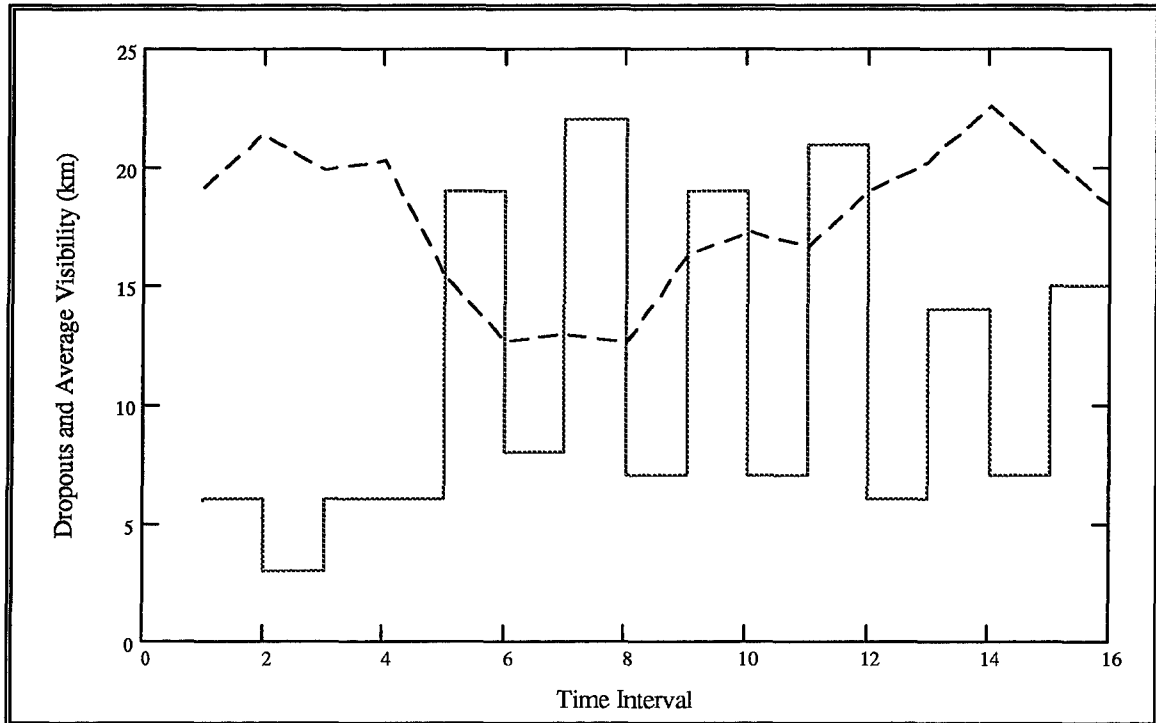
Figure C-6 Dropouts for the Building Target (solid) and Average Visibility (dashed) on
29 March (light fog)

85

Figure C-7 Tank Dropouts (solid) and Average Visibility (dashed) Over Time for
4 April (light fog)
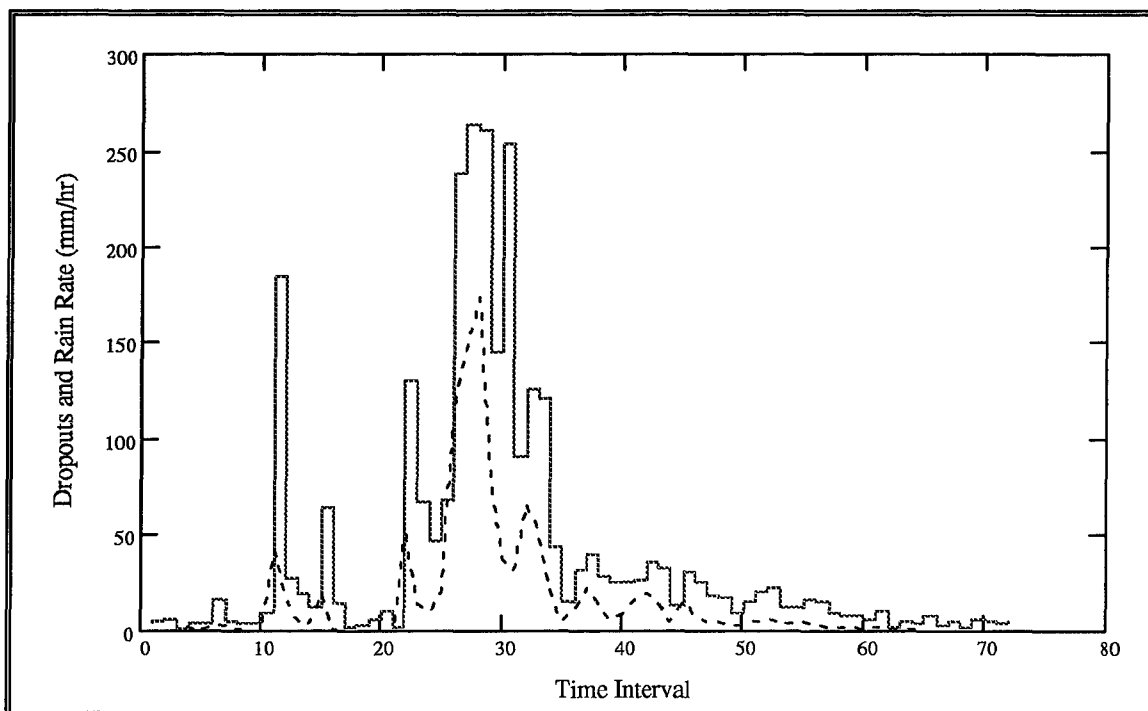
Figure C-8 Dropouts (solid) for the Building Target and Rain Rate (dashed) on
25 March (heavy rain)
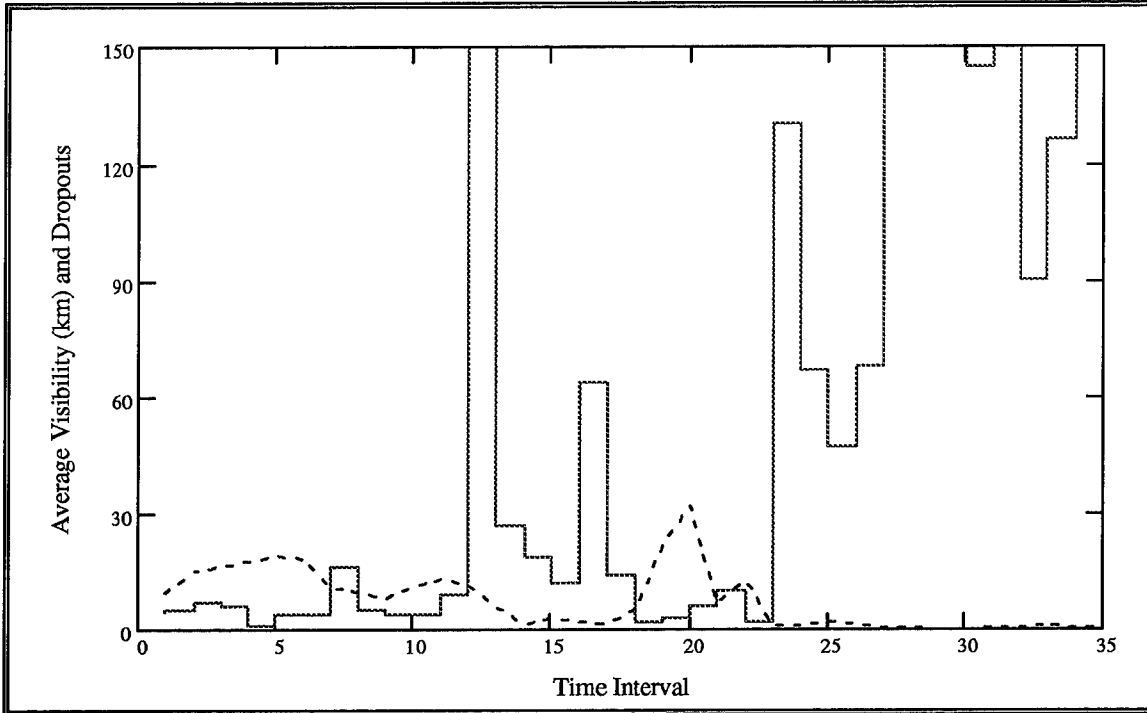
Figure C-9 Dropouts (solid) for the Building Target and Visibility (dashed) Over Time
on 25 March (heavy rain)
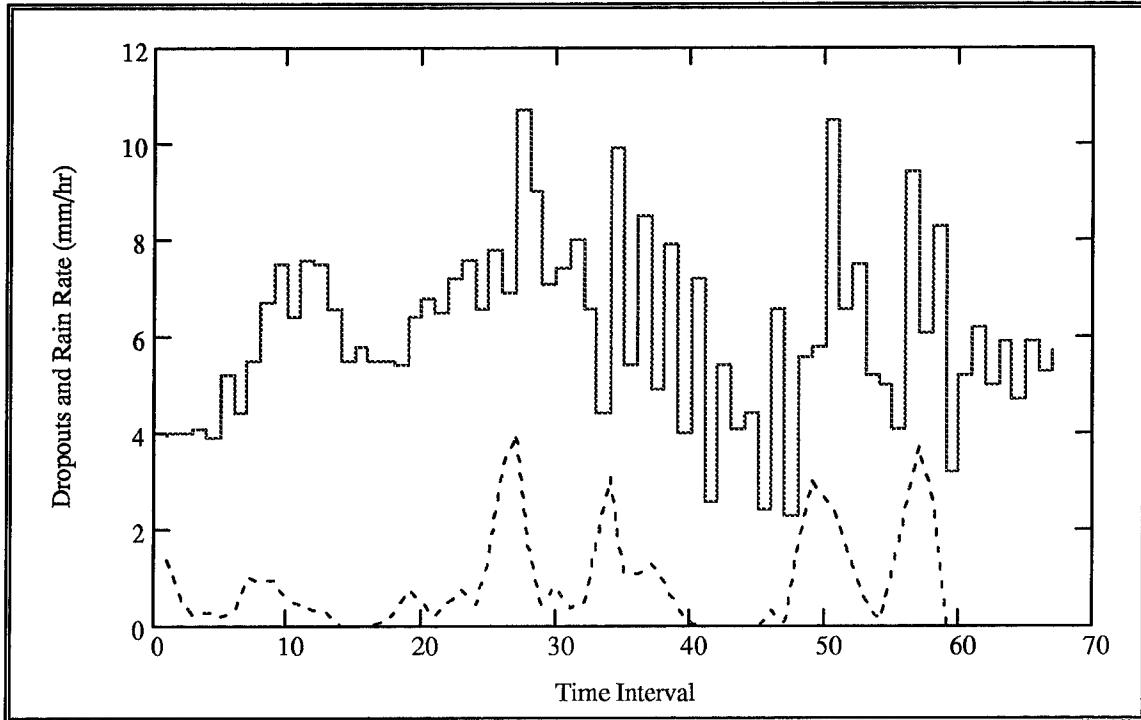
Figure C-10 Tank Dropouts (solid line) and Rain Rate (dashed line) Over Time on
18 December (light rain)
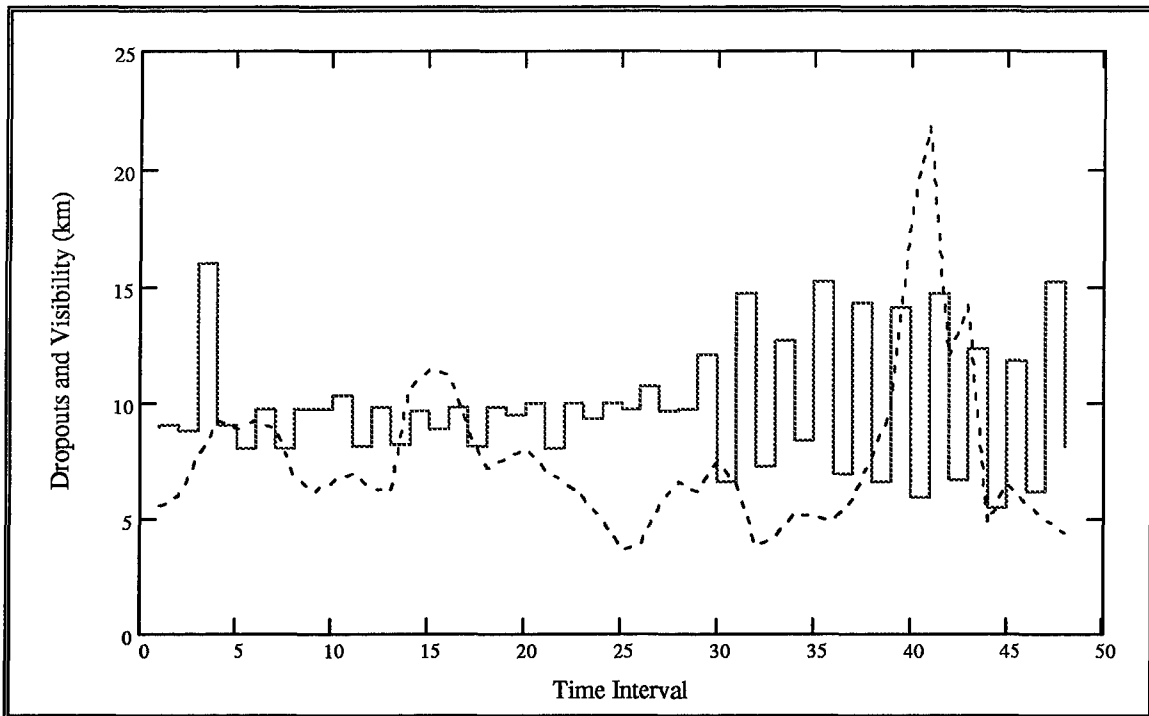
Figure C-11 Panel Dropouts (solid line) and Visibility (dashed line) Over Time on 18 December (light rain)

Figure C-12 Tank Dropouts (solid line) Divided by 10 (for scale) and Rain Rate (dashed line) Over Time on 2 November

88

Figure C-13 Panel Dropouts (solid line) Divided by 10 (for scale) and Visibility (dashed line) Over Time on 2 November (light rain)
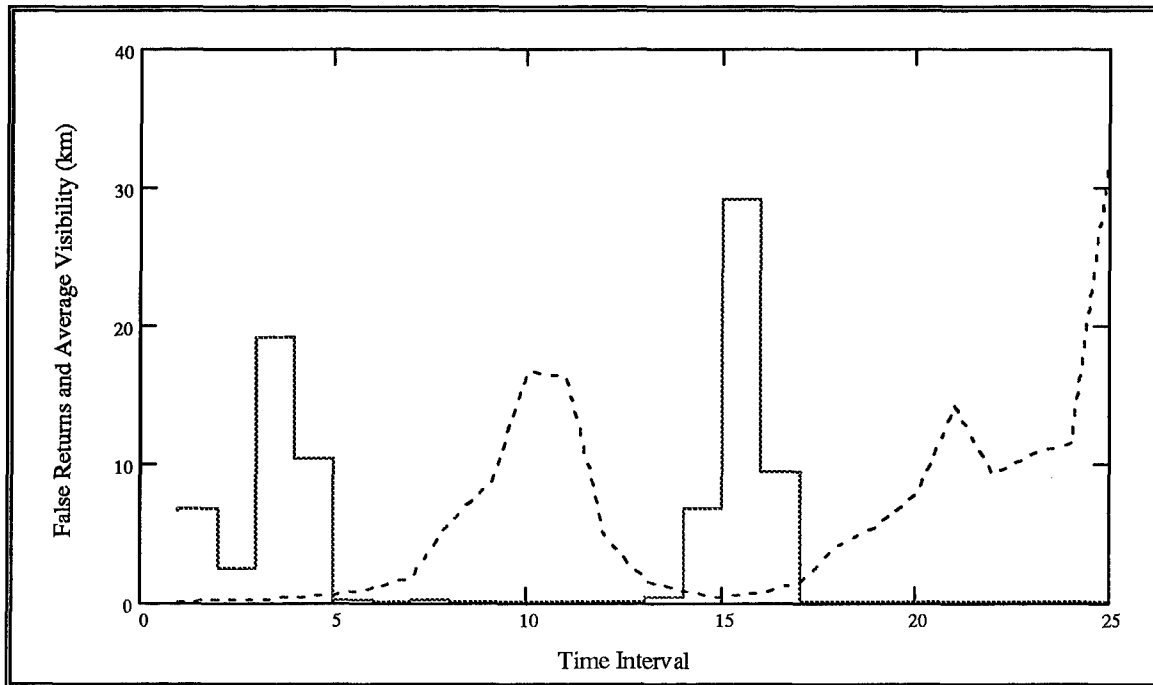
Figure C-14 False Returns Divided by 1000 (solid) and Visibility (dashed) Over Time on 15 March (thick fog)

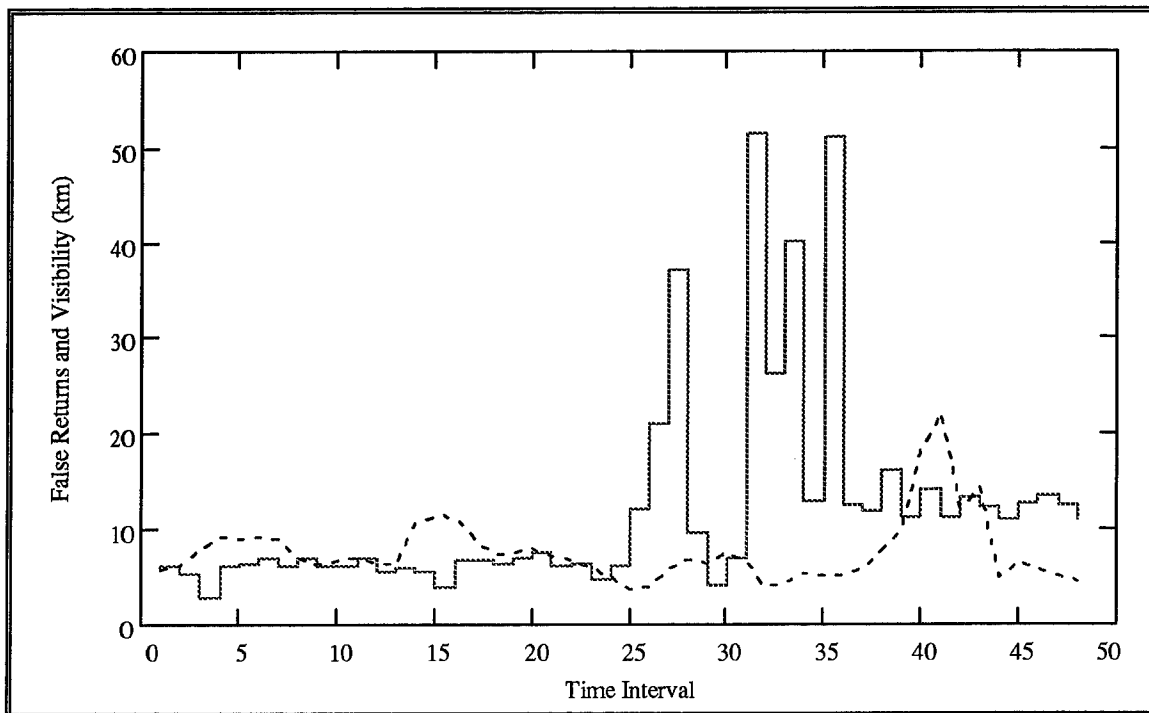Figure C-15 False Returns (solid line) Divided by 100 (for scale) and Visibility (dashed line) Over Time on 30 October (moderate fog)

Figure C-16 False Returns (solid) Divided By 10 and Visibility (dashed) on 6 December (moderate fog)
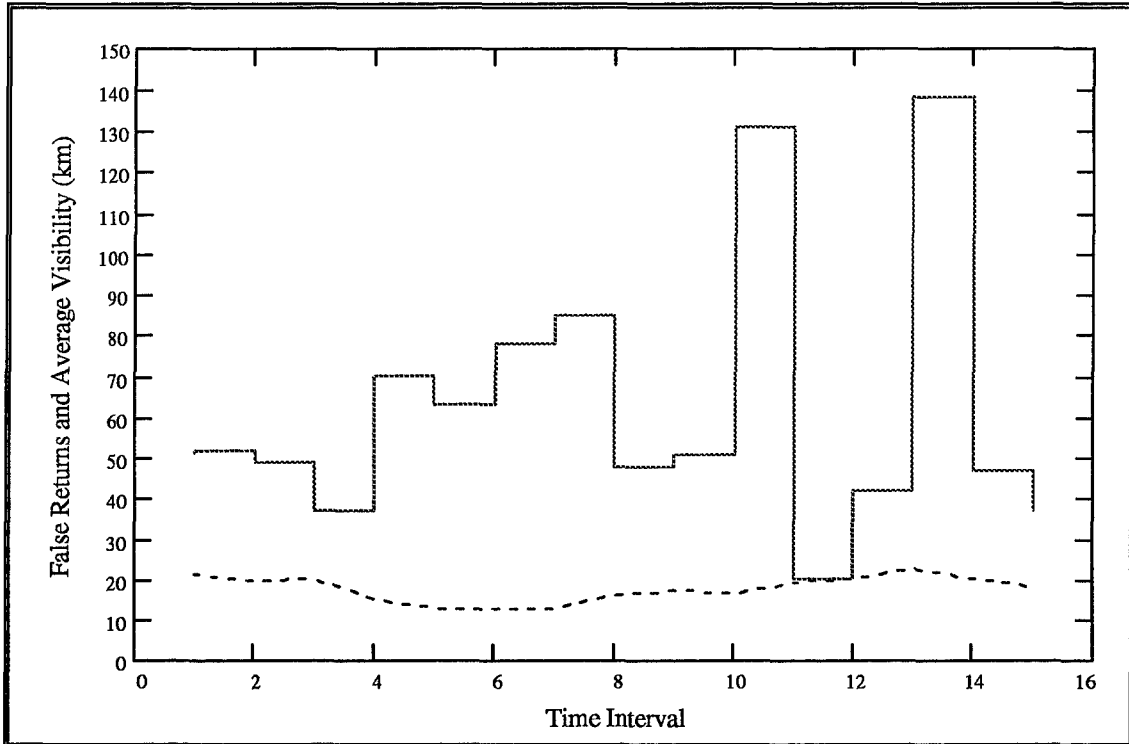
Figure C-17 False Returns (solid) and Average Visibility (dashed) on 29 March (light fog)
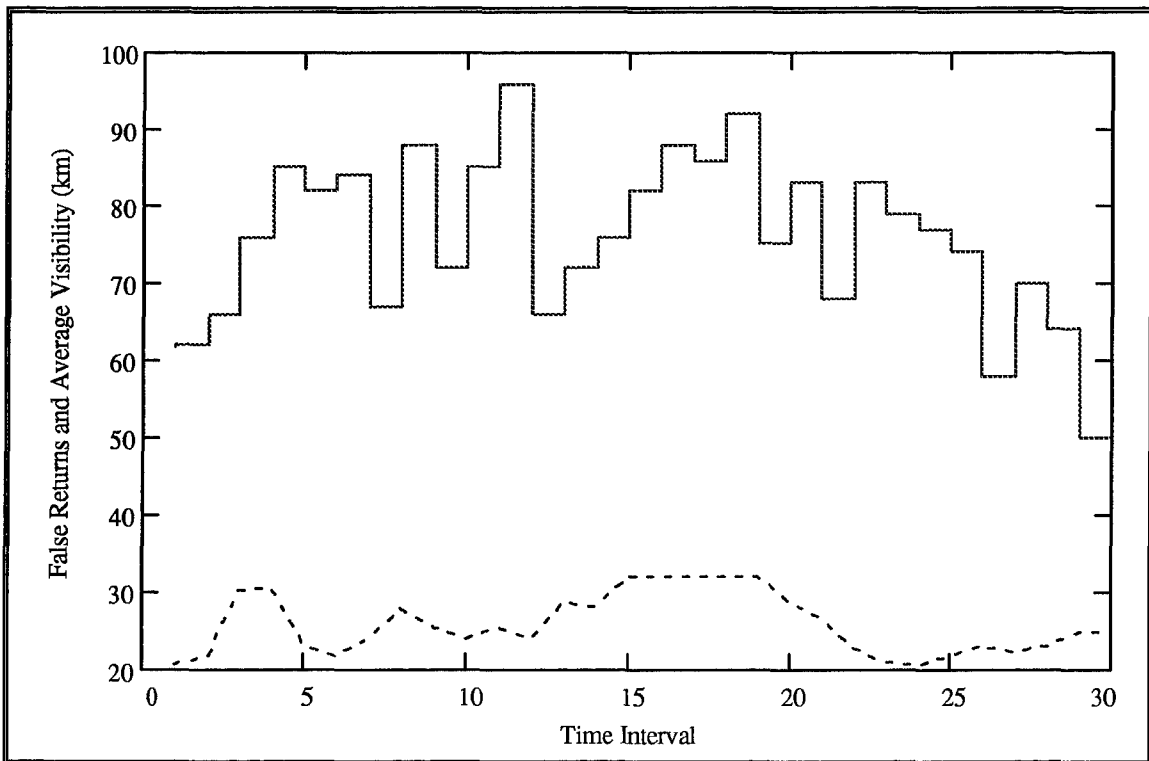
Figure C-18 False Returns (solid) and Average Visibility (dashed) Over Time for 4 April
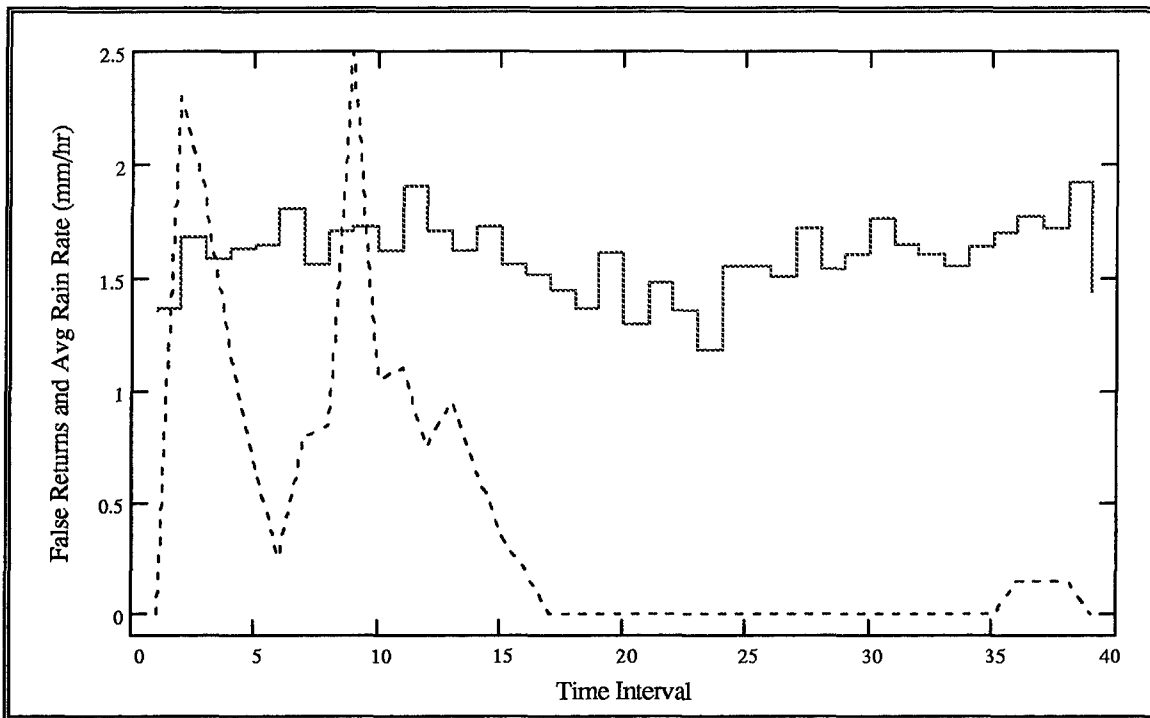(light fog)
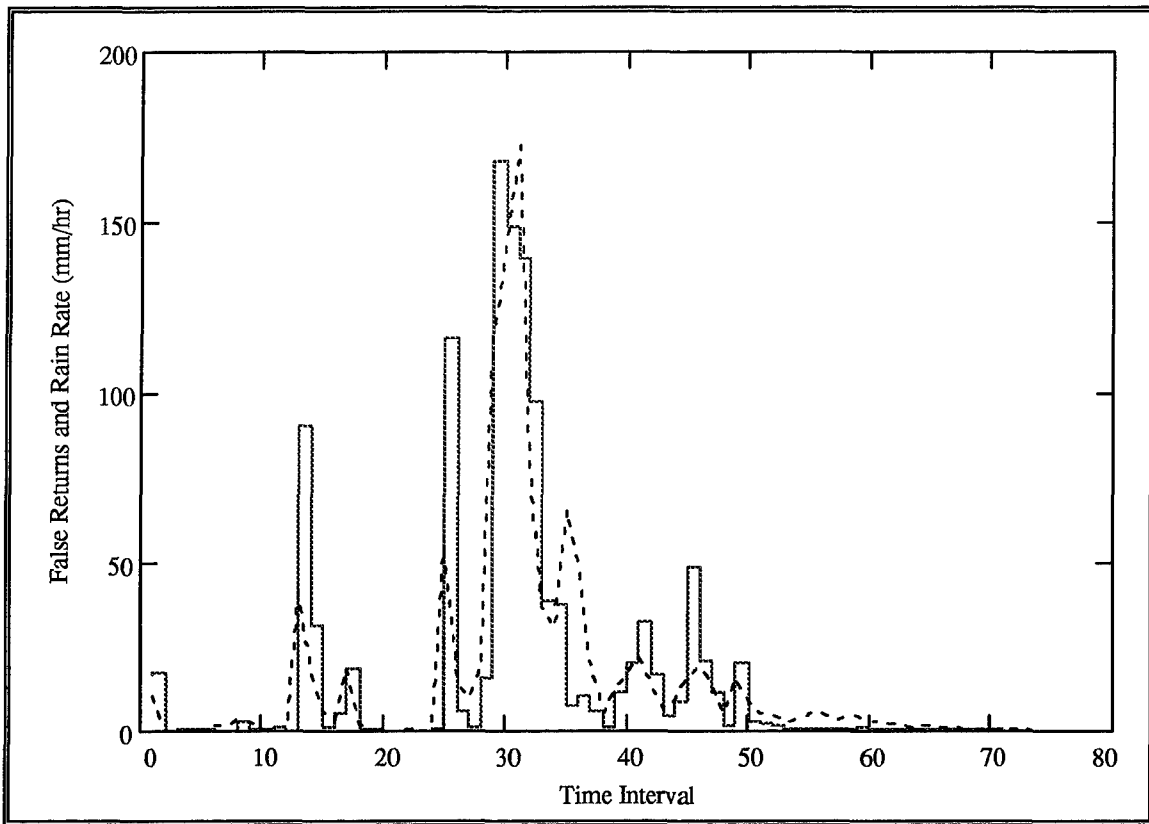
Figure C-19 False Returns (solid) Divided by 100 (for scale) and Rain Rate (dashed) Over Time on 25 March (heavy rain)
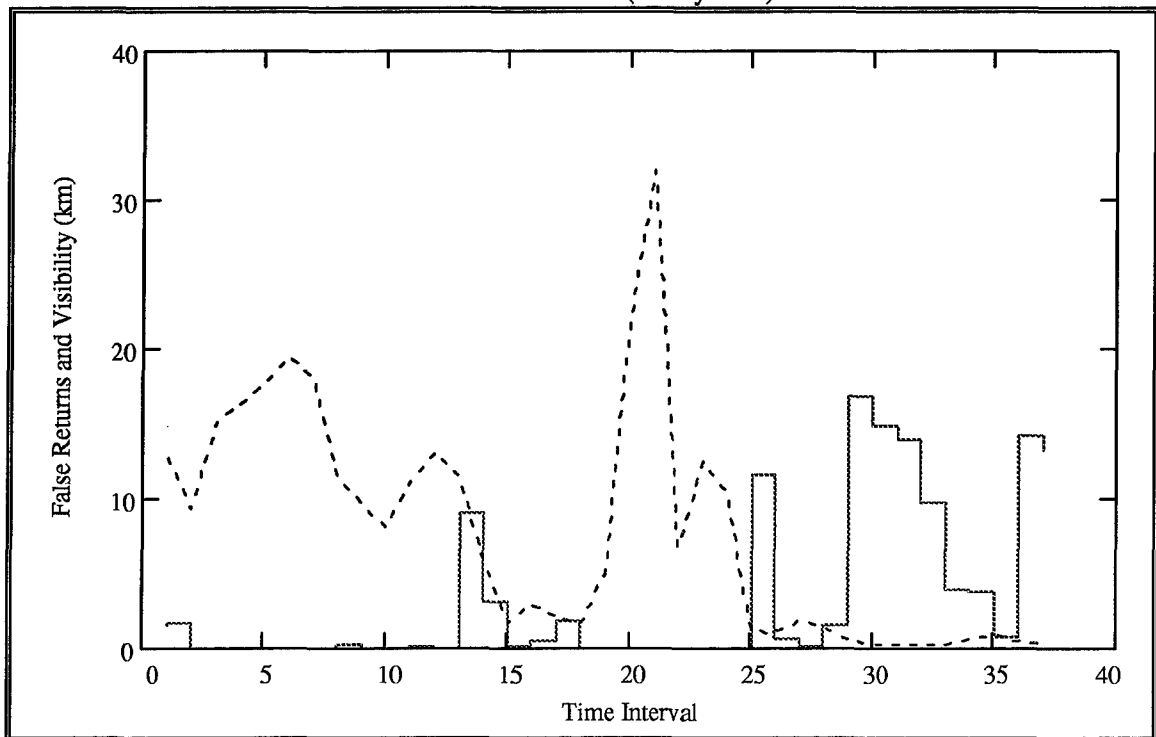
Figure C-20 False Returns (solid) Divided by 1000 (for scale) and Visibility (dashed) Over Time on 25 March (heavy rain)
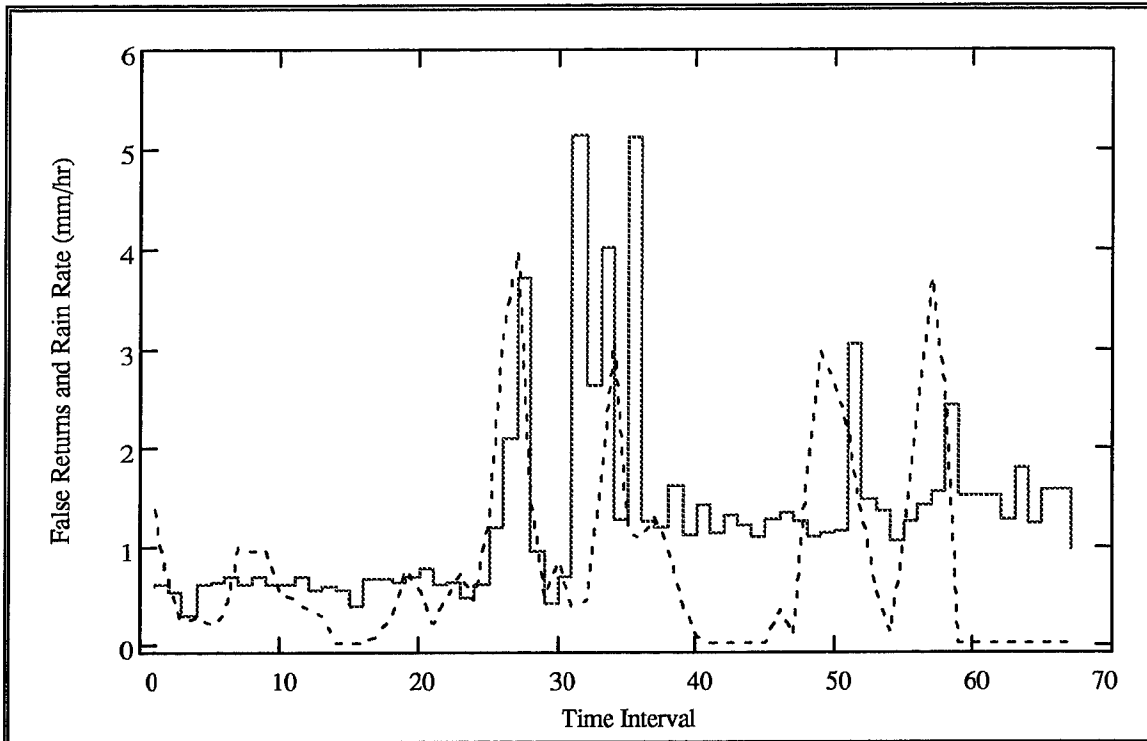
Figure C-21 False Returns (solid) Divided by 100 and Rain Rate (dashed) Over Time on 18 December (light rain)

Figure C-22 False Returns (solid) Divided by 10 (for scale) and Visibility (dashed) Over Time on 18 December (light rain)

Figure C-23 False Returns (solid line) Divided by 100 (for scale) and Rain Rate (dashed line) Over Time on 2 November
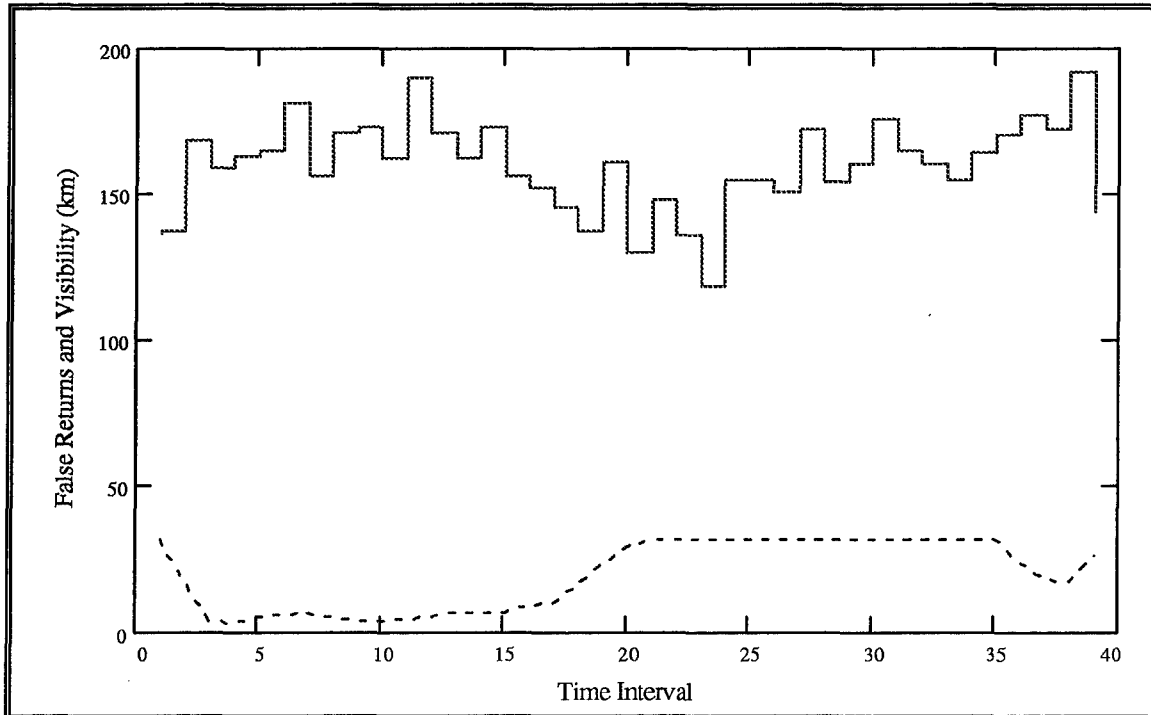
Figure C-24 False Returns (solid line) and Visibility (dashed line) Over Time on 2 November (light rain)
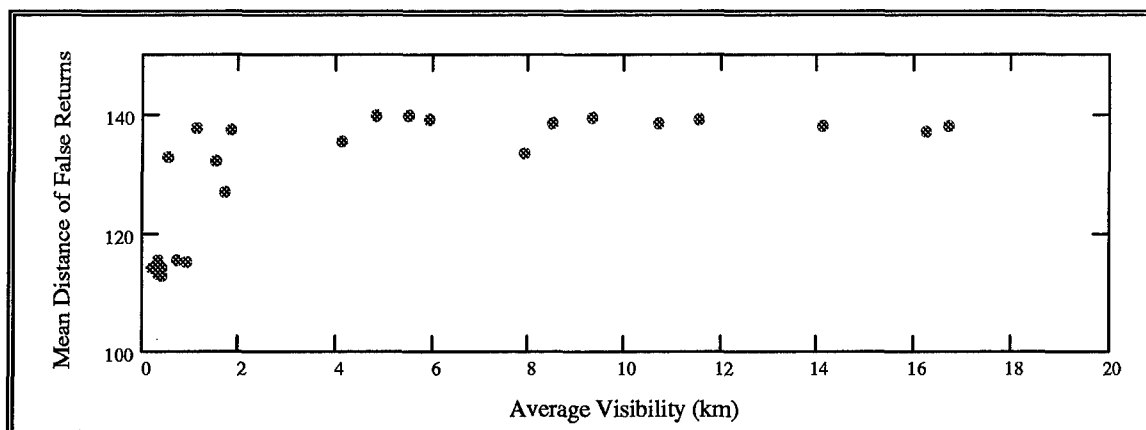
Figure D-1 Mean Distance of False Returns (meters) vs. Visibility (km) for 15 March (thick fog)
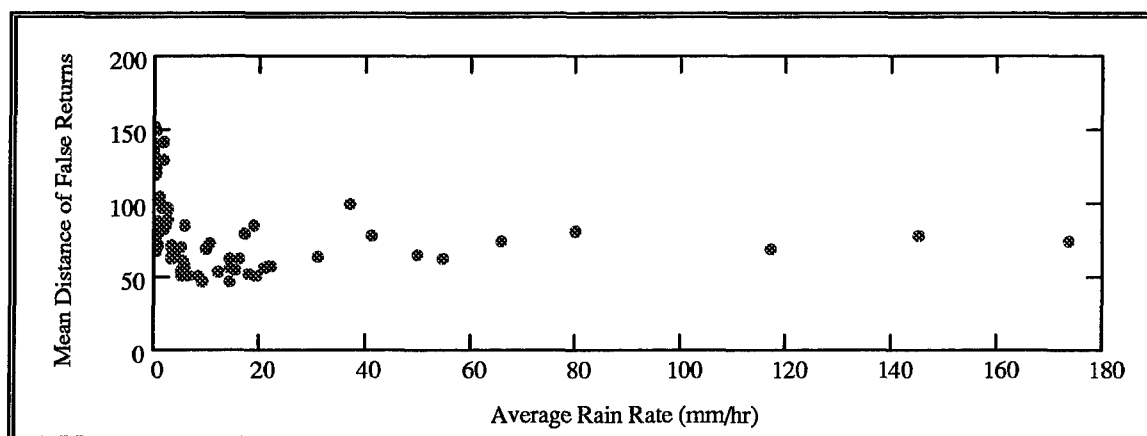

Figure D-2 Mean Distance of False Returns (meters) vs. Average Rain Rate (mm hr^{-1}) for 25 March (heavy rain)
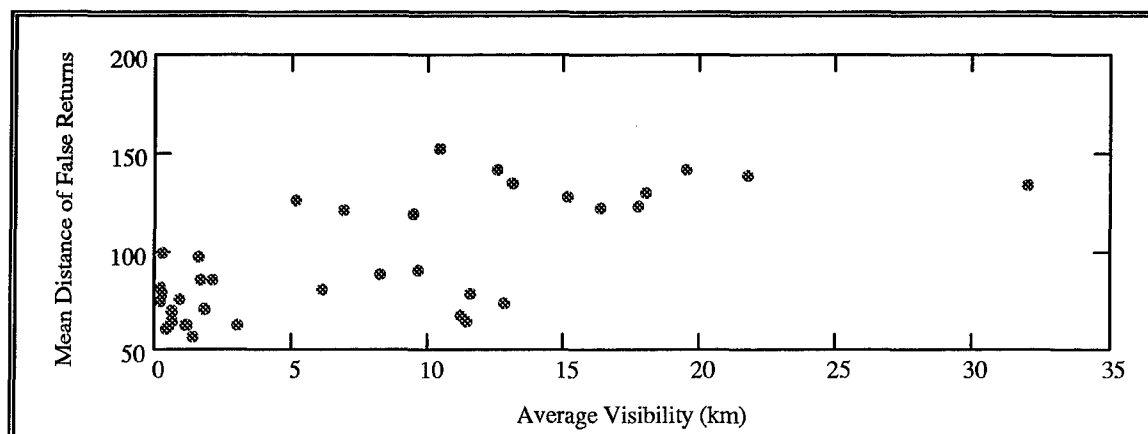

Figure D-3 Mean Distance of False Returns (meters) vs. Average Visibility (km) for 25 March (heavy rain)
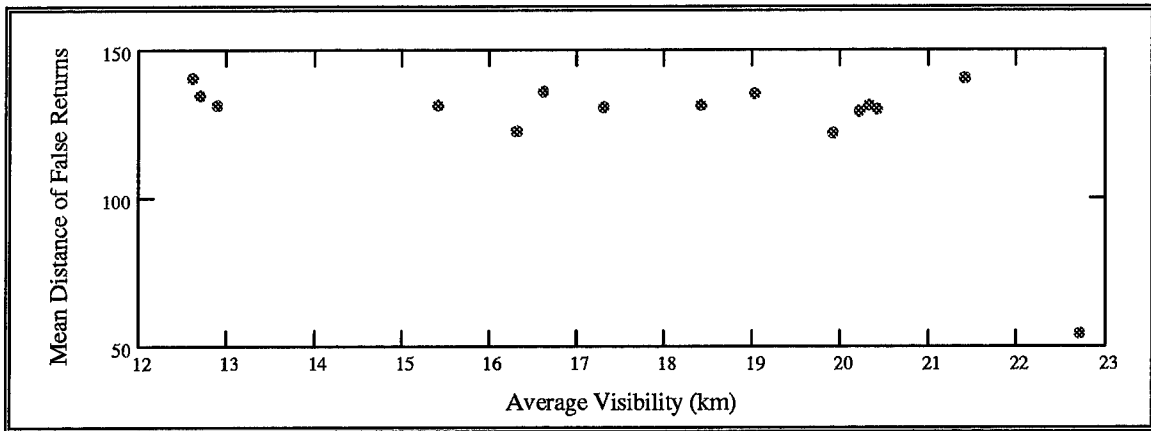
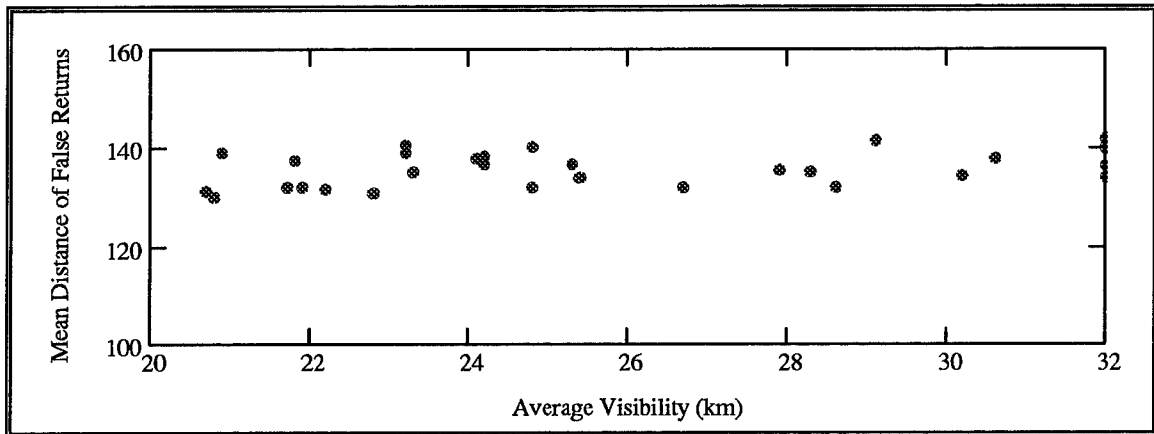Figure D-4 Mean Distance of False Returns (meters) vs. Average Visibility (km) for 29 March (light fog)

Figure D-5 Mean Distance of False Returns (meters) vs. Average Visibility (km) for 4 April (light fog)
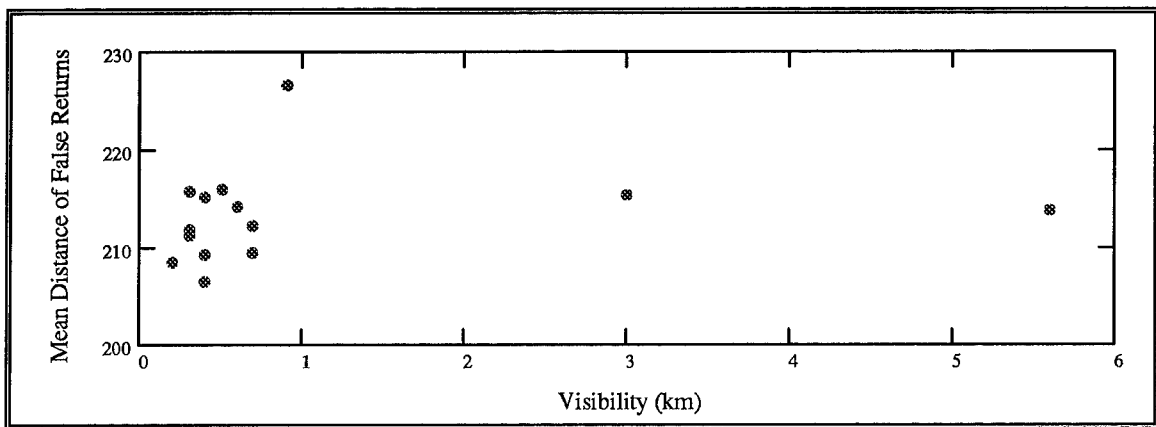

Figure D-6 Mean Distance of False Returns (meters) vs. Average Visibility (km) for 30 October (moderate fog)
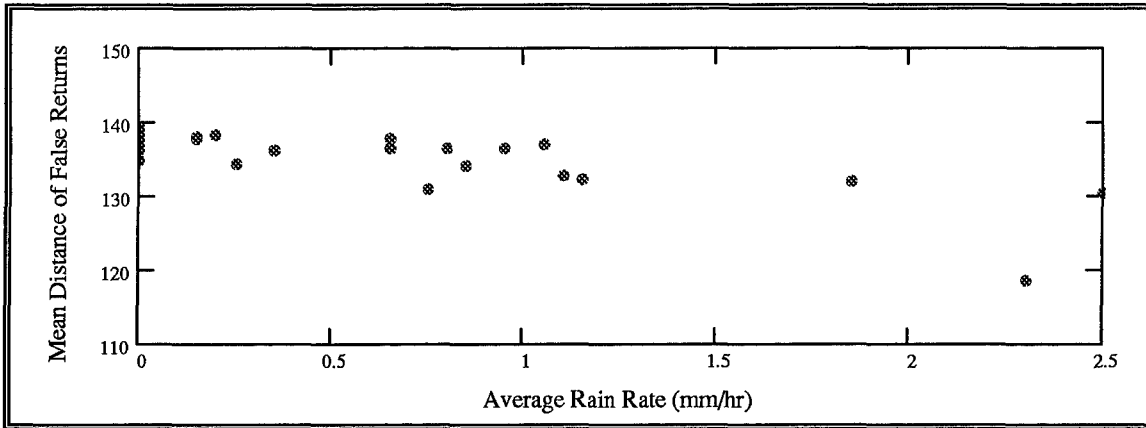
Figure D-7 Mean Distance of False Returns (meters) vs. Average Rain Rate (mm hr^{-1}) for 2 November (light rain)

Figure D-8 Mean Distance of False Returns (meters) vs. Average Visibility (km) for 2 November (light rain)

Figure D-9 Mean Distance of False Returns (meters) vs. Average Visibility (km) for 6 December (moderate fog)

Figure D-10 Mean Distance of False Returns (meters) vs. Average Rain Rate (mm hr^{-1}) for 18 December (light rain)
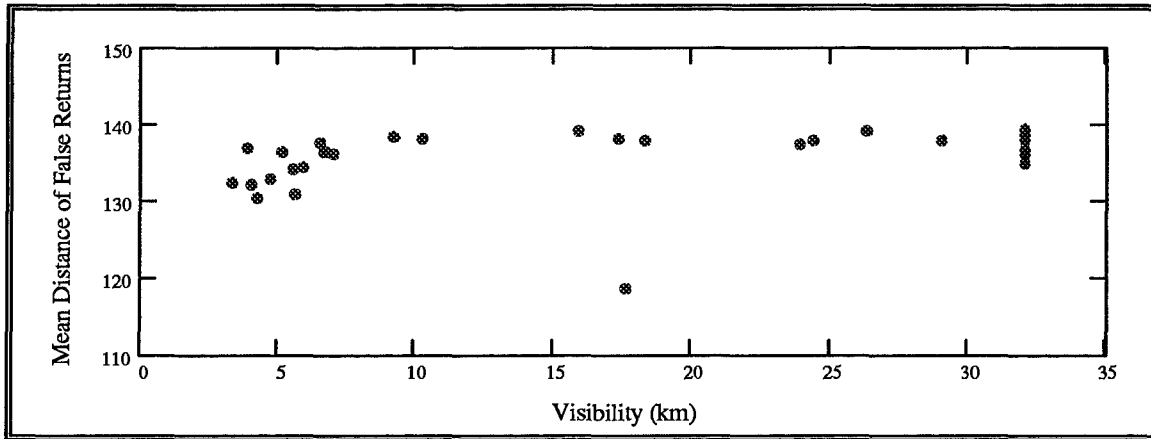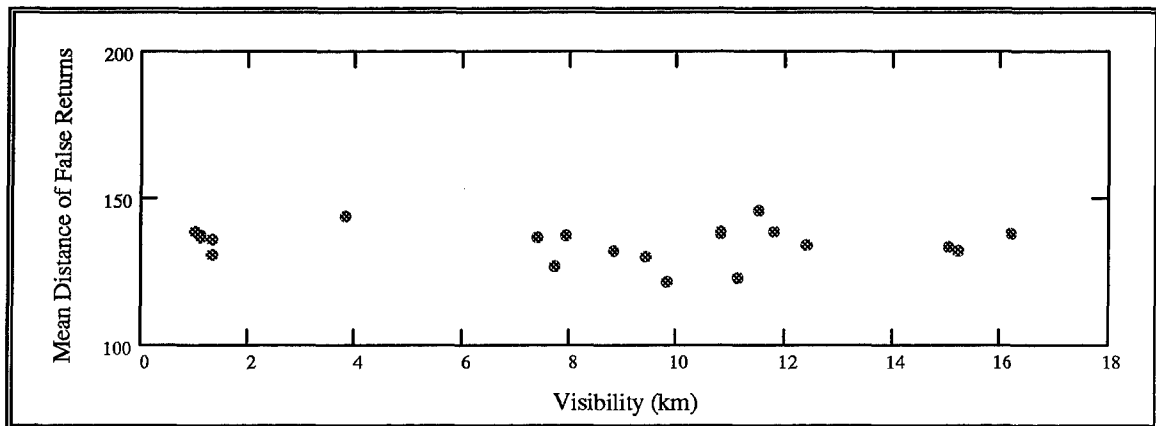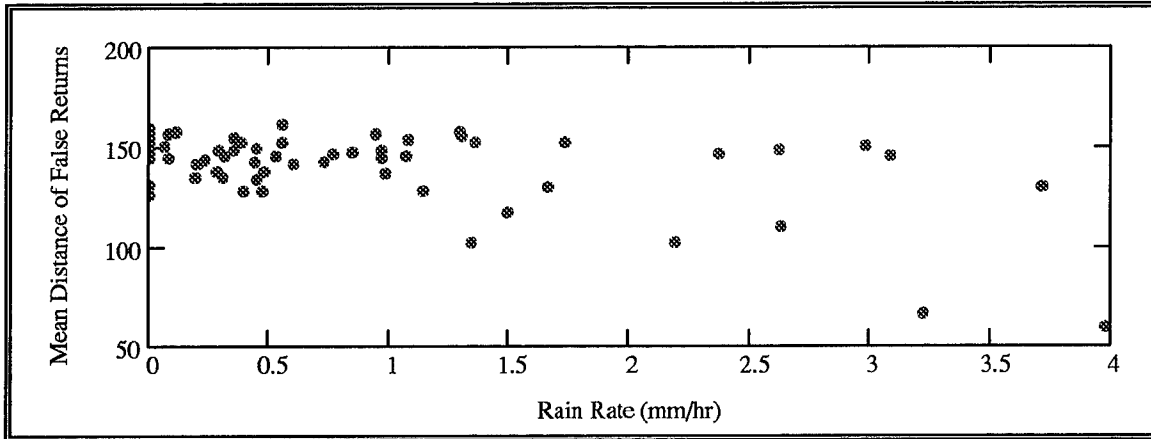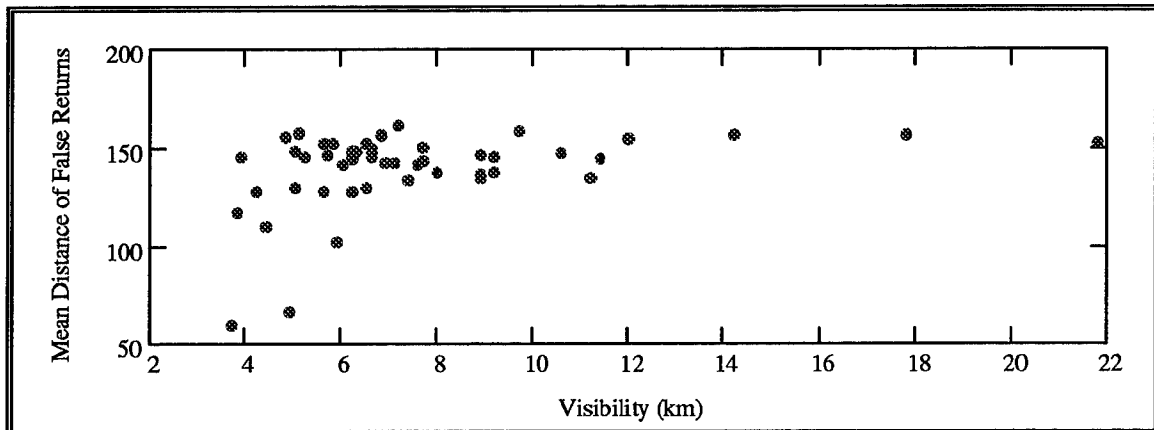

Figure D-11 Mean Distance of False Returns (meters) vs. Average Visibility (km) for 18 December (light rain)

References

Bohren, Craig F. and Donald R. Huffman, 1983: *Absorption and Scattering of Light by Small Particles*. John Wiley & Sons, Inc., 530 pp.

Chylek, Petr, 1978: Extinction and Liquid Water Content of Fogs and Clouds. *Journal of the Atmospheric Sciences,* **35,** 296-300.

Devore, Jay L., 1995: *Probability and Statistics for Engineering and the Sciences*. Wadsworth, Inc., 743 pp.

Fleagle, Robert G. and Joost A. Businger, 1980: A*n Introduction to Atmospheric Physics*. Academic Press, Inc., 432 pp.

Jelalian, Albert V., 1992: *Laser Radar Systems*. Artech House, 292 pp.

Keller, John, March 15, 1993: Will Ladar be the DoD's Next Quantum Leap? *Military &Aerospace Electronics,* 25-27.

Kimmet, Jim, October 1996: Ladar Development Evaluation Research Facility Certification. WL/MNGS Eglin AFB, FL 32542-6810.

Kyle, Thomas G., 1991: *Atmospheric Transmission. Emission, and Scattering*. Pergamon Press, 283 pp.

Metvan Instrument Pamphlet, 1995: Qualimetrics Weather Systems and Sensors, Inc. 1165 National Drive Sacramento, CA 95834.

Pinnick, R.G., D.L. Hoihjelle, G. Fernandez, and others, 1978: Vertical Structure in Atmospheric Fog and Haze and Its Effects on Visible and Infrared Extinction. *Journal of the Atmospheric Sciences,* **35,** 2020-2032.

Pinnick, R.G., S.G. Jennings, Petr Chylek, and H.J. Auvermann, 1979: Verification of a Linear Relation Between IR Extinction, Absorption, and Liquid Water Content of Fogs. *Journal of the Atmospheric Sciences,* **36,** 1577-1586.

Rogers, R.R. and M.K. Yau, 1989: *A Short Course in Cloud Physics*. Pergamon Press, 293 pp.

Tonna, Glauco, 1991: Backscattering, Extinction, and Liquid Water Content in Fog: A Detailed Study of Their Relations for Use in Lidar Systems. *Applied Optics,* **30,** 1132-1140.

Vita

Captain Clifton D. Stargardt███████████████████████████████████

████. He grew up in Richmond, Virginia, graduating from Manchester High School in 1987. He was awarded an Air Force ROTC scholarship to attend the University of Colorado in Boulder, then graduated with a Bachelor of Arts degree in Mathematics and a United States Air Force commission in May of 1991.

Capt Stargardt's first assignment was to the University of Oklahoma as an Air Force Institute of Technology Basic Meteorology Program student eventually completing the requirements for the Bachelor of Science in Meteorology degree. In 1992 Capt Stargardt was assigned to the 1ᵉ Weather Squadron at Langley Air Force Base, Virginia, as a Wing Weather Officer. In 1993, he served a temporary assignment as the Wing Weather Officer to the 4404th Composite Wing (Provisional) in Dhahran, Saudi Arabia. Upon returning, Capt Stargardt moved to the Air Combat Command headquarters as Command Weather Briefer to the ACC Commander and senior staff. In 1995 he began his studies at the School of Engineering, Air Force Institute of Technology, Wright-Patterson Air Force Base, Ohio for the Master of Science degree in Meteorology.

Capt Stargardt is single. His parents, Lt Col Kenneth H. Stargardt, USAF (retired), and Gisela A. Stargardt live in Richmond, VA.

REPORT DOCUMENTATION PAGE			*Form Approved* OMB No. 0704-0188

Public reporting burden for this collection of information is estimated to average 1 hour per response, including the time for reviewing instructions, searching existing data sources, gathering and maintaining the data needed, and completing and reviewing the collection of information. Send comments regarding this burden estimate or any other aspect of this collection of information, including suggestions for reducing this burden, to Washington Headquarters Services, Directorate for Information Operations and Reports, 1215 Jefferson Davis Highway, Suite 1204, Arlington, VA 22202-4302, and to the Office of Management and Budget, Paperwork Reduction Project (0704-0188), Washington, DC 20503.

1. AGENCY USE ONLY *(Leave blank)*	2. REPORT DATE March 1997	3. REPORT TYPE AND DATES COVERED

4. TITLE AND SUBTITLE Quantification of Weather Effects on Imaging Laser Radar	5. FUNDING NUMBERS

6. AUTHOR(S) Clifton D. Stargardt, Capt, USAF	

7. PERFORMING ORGANIZATION NAME(S) AND ADDRESS(ES) AFIT/ENP 2950 P Street Wright-Patterson AFB, OH 45433 Attn: Maj Cliff Dungey	8. PERFORMING ORGANIZATION REPORT NUMBER AFIT/GM/ENP/97M-09

9. SPONSORING/MONITORING AGENCY NAME(S) AND ADDRESS(ES) WL/MNGS 101 W. Eglin Blvd Suite 219 Eglin AFB, FL 32542-6810 Attn: Maj Jeff Grantham	10. SPONSORING/MONITORING AGENCY REPORT NUMBER

11. SUPPLEMENTARY NOTES

12a. DISTRIBUTION AVAILABILITY STATEMENT Distribution Unlimited	12b. DISTRIBUTION CODE

13. ABSTRACT *(Maximum 200 words)*

The Air Force is investigating the use of imaging laser radar systems as autonomous guidance systems on future precision guided munitions. The Air Force's Wright Laboratory is currently testing a 1.06 μm imaging laser radar (ladar) at Eglin Air Force Base. Since laser radiation can be susceptible to propagation problems through weather, quantitative understanding of these effects is important to the development of this weapon system. Ladar image degradation, in the form of target dropouts and false returns, was evaluated in various weather conditions. Statistical analysis of the images presented expected degrees of degradation according to visibility and rain fall rate. Apparent system noise masked much of the ladar response to weather. Visibility generally less than 2 kilometers, and rain rates greater than 4 millimeters per hour were required to generate dropouts and false returns from the ladar above the system noise level. Image degradation showed a generally exponential relation to visibility and those graphs were fitted with best-guess exponential curves. However, dropouts and false returns indicated a strong linear correlation with rain rate. For the heaviest rain, correlation coefficients of 0.91 and 0.90, respectfully, were computed. Best-fit linear functions were fitted to the rain rate data.

14. SUBJECT TERMS Imaging Laser Radar, Wright Laboratory			15. NUMBER OF PAGES 115
			16. PRICE CODE

17. SECURITY CLASSIFICATION OF REPORT Unclassified	18. SECURITY CLASSIFICATION OF THIS PAGE Unclassified	19. SECURITY CLASSIFICATION OF ABSTRACT Unclassified	20. LIMITATION OF ABSTRACT UL

Standard Form 298 (Rev. 2-89) (EG)
Prescribed by ANSI Std. 239.18
Designed using Perform Pro, WHS/DIOR, Oct 94